

UNIVERSITÀ DEGLI STUDI DI PADOVA

DIPARTIMENTO DI FISICA E ASTRONOMIA “GALILEO GALILEI”

Master Degree in Astrophysics and Cosmology

Final dissertation

Study of the $^{20}\text{Ne}(p, \gamma)^{21}\text{Na}$ reaction at LUNA

Supervisor:

Prof. Antonio Cacioli

Co-supervisor:

Prof.ssa Sandra Zavatarelli

Candidate:

Lucia Barbieri

Academic year 2021/2022

Abstract

The synthesis of Ne, Na, Mg, and Al isotopes is connected to the NeNa-MgAl cycles of stellar burning. The entire cycle speed is controlled by the $^{20}\text{Ne}(p,\gamma)^{21}\text{Na}$ reaction ($Q_{\text{value}}=2431.68$ keV) which is the first and slowest reaction of the whole NeNa cycle. At the state of the art, the associated reaction rate uncertainty therefore affects the production of the elements in the NeNa cycle and their yields in various stellar environments. In the relevant temperature range from 0.1 GK to 1 GK, the rate is mainly dominated by the 366 keV resonance, corresponding to the excited state of $E_x = 2797.5$ keV, and by the direct capture component. The present thesis analyses the direct capture below energies of 400 keV, which has been studied in deep underground at LUNA (Laboratory for Underground Nuclear Astrophysics), located at Gran Sasso National Laboratories in Italy. The reaction has been measured using the intense proton beam delivered by the LUNA 400 kV accelerator and a windowless differentially pumped gas target filled with natural neon at pressure of few mbar. Two fully shielded high-purity germanium detectors collected the photons produced in the reaction, obtaining associated gamma spectra. This work will present the experimental details of the campaign and its scientific results, focusing on the measured $^{20}\text{Ne}(p,\gamma)^{21}\text{Na}$ cross section at stellar energies and its possible impact on the associated thermonuclear reaction rate.

Contents

1	Introduction	3
2	Thermonuclear reaction rates	4
2.1	Non-resonant reactions	6
2.1.1	Direct capture	7
2.2	Resonant reactions	9
3	Astrophysical motivation	12
3.1	The $^{20}\text{Ne}(p, \gamma)^{21}\text{Na}$ reaction	12
3.2	Neon-Sodium (Ne-Na) burning cycle	13
3.3	RGB stars, Globular Clusters and AGB stars	15
3.4	ONe classical novae and Type Ia supernovae	18
4	State of the art	19
5	The LUNA experiment	24
5.1	400 kV Accelerator	26
5.2	Windowless gas target	27
5.3	Calorimeter	30
5.4	Background	32
5.4.1	Natural background	32
5.4.2	Beam-induced background	33
6	Experimental setup for $^{20}\text{Ne}(p, \gamma)^{21}\text{Na}$ reaction study	34
6.1	Campaign details	36
6.2	Calorimeter calibration	36
7	Target characterization	37
7.1	Gas density without beam	40
7.2	Beam heating effect	40
8	Detection efficiency	42
9	Data analysis	49
9.1	Spectra energy calibration and net peak areas	53
9.2	Energy loss and charge determination	58
9.3	Experimental yields	58
9.4	S-factor	59
10	$^{20}\text{Ne}(p, \gamma)^{21}\text{Na}$ reaction rate	62
11	Conclusions and future perspectives	66
12	Acknowledgments	67

1 Introduction

The life of a star is continuous battle against its own gravity, which acts as an inward directed force leading the star to collapse under its own weight. However, thanks to the high temperatures and densities reached in stellar interiors, this collapse can be halted by the onset of thermonuclear reactions. These reactions can provide the internal pressure needed to keep the star in hydro-static equilibrium, as long as nuclear fuel is available.

The evolution of a star during its whole life can be followed on the Hertzsprung-Russell (HR) diagram, one of the most powerful tools in astrophysics, which can be used to trace stellar evolutionary stages. The diagram relates the luminosity (or the absolute magnitude) of a star to its effective temperature. An example is shown in Figure 1, where the path of three different stars having masses respectively of 1, 5 and 10 M_{\odot}) is also reported.

Stars located at different regions of the HR diagram are burning different types of fuels through thermonuclear reactions. In general, nuclear burnings proceed through chain and cycles, during which various elements are burned into heavier ones, depending on the achieved temperature. Main nuclear processes include hydrogen, helium, carbon, neon, oxygen and silicon burnings. They can be burned either in the core or in shells around it, creating an onion-like structure of burning shells. When a fuel is exhausted, the core begins to contract, increasing its pressure and heating up. The equilibrium can be restored only when the temperature has risen enough to ignite the successive fuel.

Nuclear reactions in a star are important not only as an energy source that keeps the star alive, but also as a way to synthesize the chemical elements we found all over the cosmos. It is therefore crucial to characterize precisely the nuclear network through which the reactions proceeds. Theoretical models have been developed to reproduce the evolution of different stars and the observed elemental abundances. One of the most important input to these models are thermonuclear reaction rates: the number of reactions taking place at a given stellar temperature per unit time and unit volume. The goal of experimental nuclear astrophysics is to directly measure or to extrapolate at energies relevant for stars these reactions rates, with uncertainties as small as possible.

The first section of this thesis will provide a general overview of thermonuclear reaction rates for different types of nuclear reactions. Then, the astrophysical relevance of the $^{20}\text{Ne}(p, \gamma)^{21}\text{Na}$ studied for this work will be underlined, focusing on the main astrophysical sites where the reaction takes place. State of the art knowledge of the reaction will be also briefly reviewed. In the third section the LUNA (Laboratory for Underground Nuclear Astrophysics) facility and the experimental setup adopted for the $^{20}\text{Ne} + p$ study will be presented in details. Afterwards I will go through the data analysis procedure and finally the preliminary results obtained will be shown.

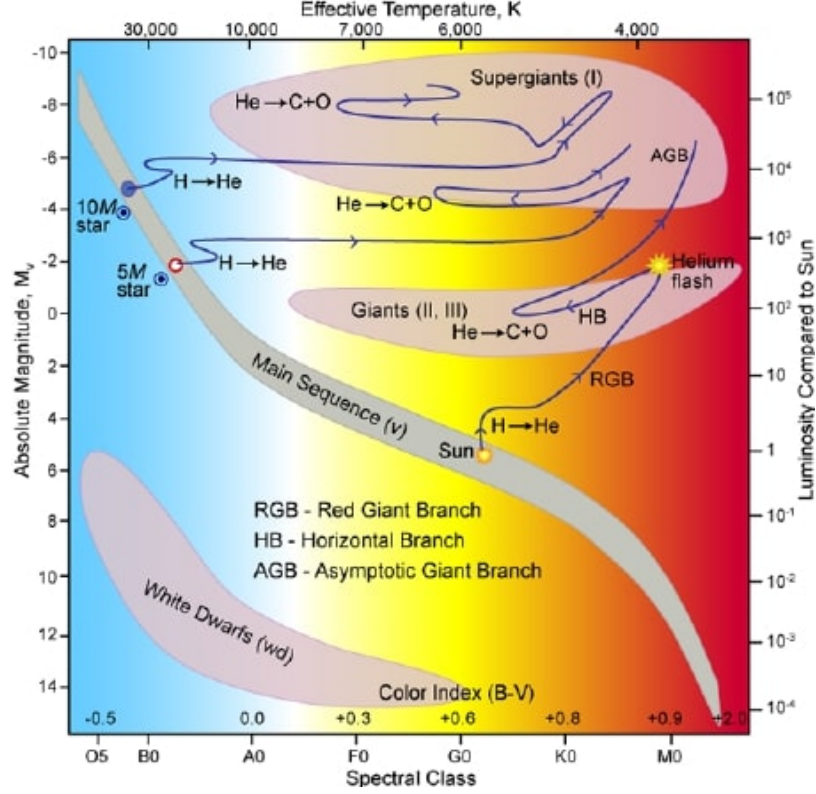


Figure 1: Hertzsprung-Russell (HR) diagram which shows stars' evolution in terms of their luminosity and temperature. The former is reported on the y right axis and is connected to stellar mass and radius. The latter is reported on the x top axis. The colors of the background show the spectral class (reported on the x bottom axis) to which a star of given color index belongs. The stellar evolutionary tracks for three different stellar masses (1, 5 and $10 M_{\odot}$) are shown as blue lines passing through the main stellar evolutionary phases. Illustration from Robert Hollow, Commonwealth Science and Industrial Research Organisation (CSIRO), Australia, adapted by Carin Cain.

2 Thermonuclear reaction rates

A nuclear reaction can be schematized as a two body interaction of the type $A + a \rightarrow B + b$, where a is the projectile, A is the target nucleus, B and b the products of the reaction. The associated reaction rate is defined as the number of reactions per unit time and unit volume [1] and depends on the nuclear cross section σ , the densities of the reactants n_A and n_a and their relative velocity v :

$$r_{Aa} = n_A \cdot n_a \cdot v \cdot \sigma(v) \quad (1)$$

In stellar plasma, however, nuclei do not have the same exact speed, but they rather follow a certain distribution of relative velocities $\phi(v)$. For a non degenerate non relativistic plasma in thermal equilibrium, this is given by the Maxwell-Boltzmann (MB) distribution, which tell us the probability that two nuclei have a relative velocity between v and $v + dv$:

$$\phi(v) = \left(\frac{\mu}{2\pi k_B T} \right)^{3/2} e^{-\frac{\mu v^2}{2k_B T}} 4\pi v^2 \quad (2)$$

where $\mu = \frac{m_a m_A}{m_a + m_A}$ is the reduced mass, k_B the Boltzmann constant and T the temperature. The distribution is normalized to unity.

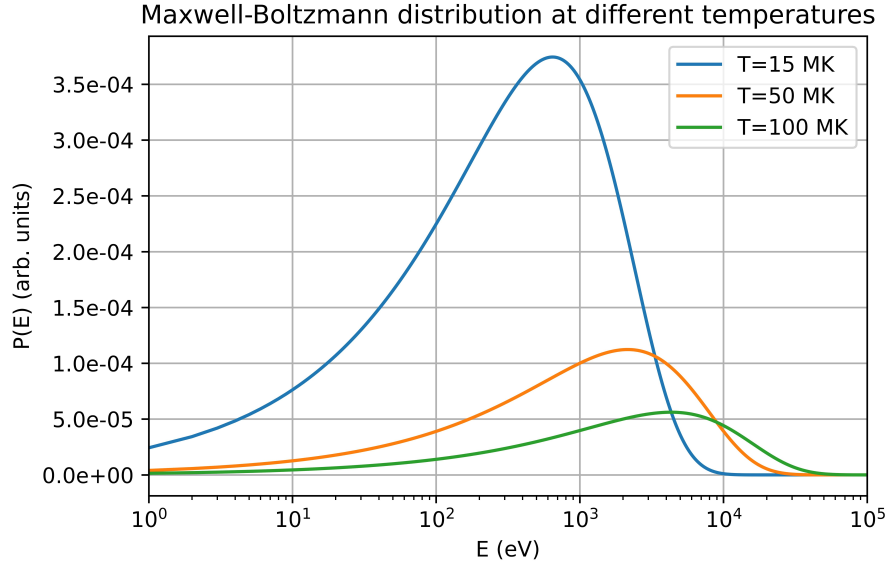


Figure 2: Maxwell-Boltzmann distribution giving the number of particles with energy between E and $E+dE$ at different temperatures.

Using the velocity distribution $\phi(v)$, we can rewrite Eq. 1 as

$$r_{Aa} = n_A \cdot n_a \cdot \int_0^{\infty} \sigma(v)v\phi(v) dv = n_A \cdot n_a \cdot \langle \sigma v \rangle \quad (3)$$

where $\langle \sigma v \rangle$ is the reaction rate per particle pair.

It is also possible to switch to the energy domain considering that $E = \frac{1}{2}\mu v^2$ and $dE = \mu v dv$, thus obtaining $\phi(E)$

$$\phi(E) = \frac{2}{\sqrt{\pi}} \frac{1}{(k_B T)^{3/2}} e^{-\frac{E}{k_B T}} \sqrt{E} \quad (4)$$

In Figure 2 an example of the MB distribution for different stellar temperatures is plotted.

Finally we can write the reaction rate per particle pair as function of stellar energies

$$\langle \sigma v \rangle = \left(\frac{8}{\pi \mu} \right)^{1/2} \frac{1}{(k_B T)^{3/2}} \int_0^{\infty} E \sigma(E) e^{-\frac{E}{k_B T}} dE \quad (5)$$

Note that, in practice, it is the quantity $N_A \langle \sigma v \rangle$ (where N_A denotes the Avogadro constant) in units of $cm^3 mol^{-1} s^{-1}$ which is usually tabulated and presented in the literature [1]. The energy dependence of the cross section is linked to the reaction mechanism, which can be resonant or non-resonant. In the following sections the basics of the two mechanisms will be briefly explained, with a focus on direct capture reactions relevant for this thesis.

2.1 Non-resonant reactions

Nuclei are positively charged particles, made up of protons and neutrons. Therefore, according to Coulomb law, they repel each other establishing a repulsive Coulomb potential. The qualitative behaviour of this potential is shown in Figure 3. For radius r larger than the nuclear radius, the potential is given by $E_C = \frac{Z_T Z_p e^2}{r}$, where Z_T is the charge of the target nucleus, Z_p the charge of the projectile and e the elementary charge. At shorter distances, instead, the attractive strong force creates a potential well that can hold interacting nuclei together. This implies that only projectiles with energy $E_p > E_C$ can overcome the Coulomb barrier and fuse with the target nucleus. Otherwise, they will be repelled after reaching a minimum distance $R_C(E)$, classically given by the balance of the projectile energy and the barrier.

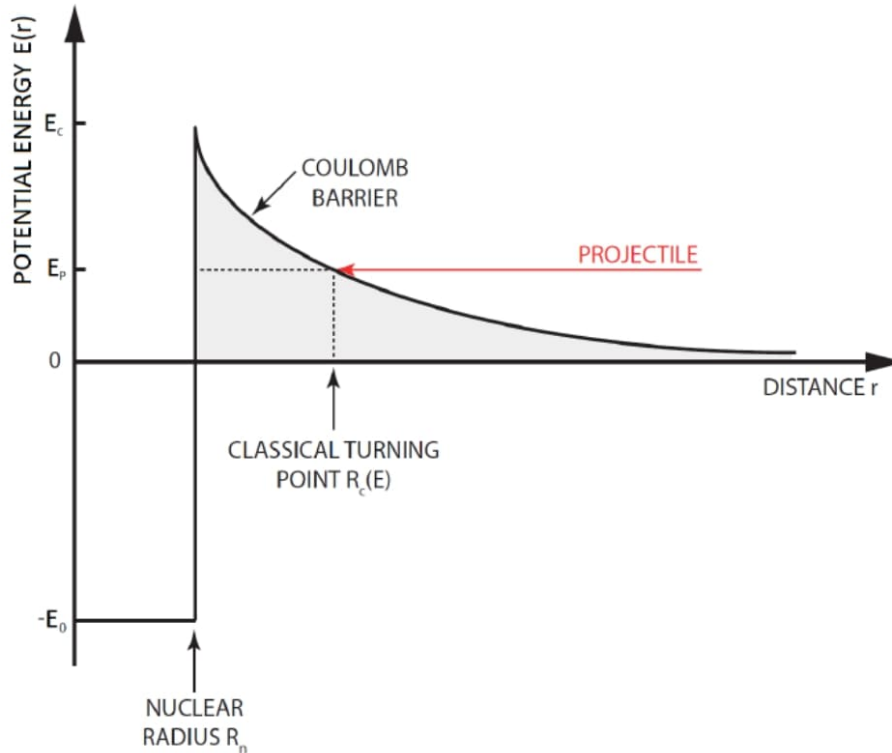


Figure 3: A simple representation of the combined nuclear and Coulomb potentials. An incident projectile with energy $E < E_C$ reaches the minimum distance from the target nucleus (classical turning point) and is bounced back.

This classical limit for fusion has an important consequence. In stars, nuclei kinetic energies arising from internal temperature usually cover a range of $k_b T \approx$ hundreds of keV or less, while Coulomb barrier is higher, of the order of MeV. Projectiles are not energetic enough to overcome the fusion barrier and initiate the reaction. Only introducing quantum mechanics in the picture can solve this 'issue', through the *quantum tunneling effect*: there is a finite probability for a nucleus to overcome the Coulomb barrier, even for $E_p < E_C$. This tunneling probability can be found by solving the *Schrödinger* equation and is given as first approximation by the Gamow factor

$$P_{\text{tunneling}} = e^{-2\pi\eta} \quad \eta = Z_p Z_T \alpha \sqrt{\frac{\mu c^2}{2E}} \quad (6)$$

where η is the Sommerfeld parameter, with α the fine structure constant, μ the reduced mass in amu and E the energy in the center of mass in keV. It is clear that the probability increases with increasing energy. For charged particles, the cross section will be proportional to $P_{tunneling}$ and also to the geometrical cross section, given by the De Broglie wavelength according to

$$\sigma(E) \propto \pi \lambda^2 = \pi \left(\frac{h}{\sqrt{2\mu E}} \right)^2 \quad (7)$$

where h is the Plank constant. Combining the two proportionalities given by Eq. 6 and 7 and residual dependencies, we can finally write the cross section as

$$\sigma(E) = \frac{1}{E} S(E) e^{-2\pi\eta} \quad (8)$$

The quantity $S(E)$ is called *astrophysical S-factor* and contains all the nuclear properties on which the reaction cross section depends. For a non-resonant process, the S-factor energy dependence is usually weak, showing a rather flat and smooth behaviour. This allows an easier extrapolation of $S(E)$ at low stellar energies from experimental data at higher energy values.

Finally, we can write the thermonuclear reaction rate per particle pair as

$$\langle \sigma v \rangle = \left(\frac{8}{\pi\mu} \right)^{1/2} \frac{1}{(k_B T)^{3/2}} \int_0^\infty S(E) e^{-2\pi\eta} e^{-\frac{E}{k_B T}} dE \quad (9)$$

The two exponential have a different energy dependence: while the tunneling probability increases with increasing energy, the exponential coming from the MB distribution decreases for increasing energies. The convolution of this two terms produces a narrow energy window within which most of the reactions take place: the *Gamow peak*. It depends on the mass and the charge of the interacting nuclei and on the typical temperature of the stellar environment of interest. Below the Gamow peak, the Coulomb barrier penetrability is too low, above it the nuclei in the high energy tail of the MB are not enough to produce a significant number of reactions. In Figure 4 the two exponentials dependencies and the Gamow peak are plotted for the $^{20}\text{Ne}(p, \gamma)^{21}\text{Na}$ reaction at a typical temperature of $T=0.4$ GK.

The maximum of the peak can be found putting the derivative of exponentials products to 0 and is given in MeV units by

$$E_0 = 0.122(Z_1^2 Z_2^2 \mu T_9^2)^{1/3} \quad (10)$$

where T_9 is the temperature expressed in units of GK and μ the reduced mass in amu. At first approximation, it is possible to express its effective width Δ by considering the peak Gaussian shaped, giving

$$\Delta = \frac{4}{\sqrt{3}} \sqrt{E_0 k_B T} \quad (11)$$

We can therefore identify the Gamow window with a lower and upper boundary given by $E_0 \pm \frac{\Delta}{2}$: it is crucial to know the reaction rate in this energy range as precisely as possible for each possible stellar scenario where the NeNa cycle is relevant, to give reliable inputs for nuclear network computations.

2.1.1 Direct capture

The direct capture (or radiative capture) is a non-resonant reaction of the type $A + a \rightarrow B + \gamma$, where the projectile a is immediately absorbed by the target nucleus A . The resulting heavier nucleus

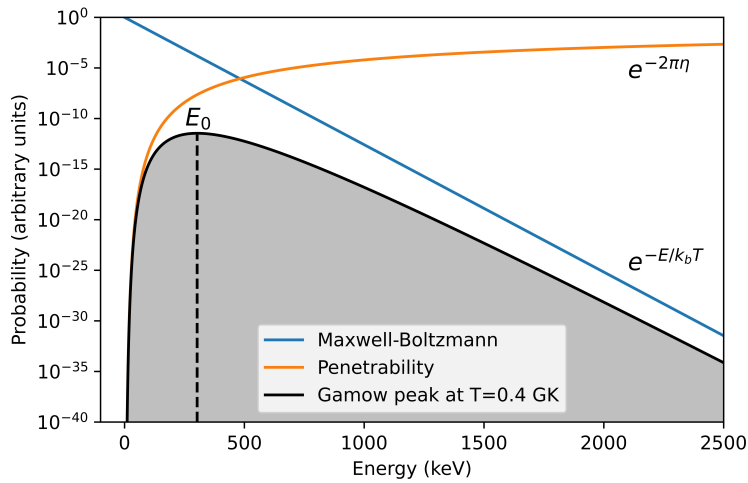


Figure 4: Gamow energy window for the $^{20}\text{Ne}(p, \gamma)^{21}\text{Na}$ reaction at 0.4 GK (typical ONe novae temperature). In orange the tunneling probability, in blue the Maxwell-Boltzmann distribution and in gray the Gamow function given by the products of the two exponentials. The maximum of the peak E_0 is also reported.

B is created either in the ground state or in an excited state, emitting a photon with energy E_γ

$$E_\gamma = Q_{value}^1 + E_{cm} - E_i$$

where E_{cm} is the energy available in the two interacting nuclei center of mass and E_i is the energy of the level populated in the product nucleus. If the B nucleus is excited, a gamma-ray cascade is emitted, eventually leaving the nucleus in its fundamental state.

A schematic representation of the process is presented in Figure 5. Direct capture is a purely electromagnetic process, whose cross section is therefore proportional to the interaction Hamiltonian H matrix element between entrance channel A+a and exit channel B

$$\sigma \propto | \langle B | H | A + a \rangle |^2$$

If in a nuclear reaction cycle there are radiative captures, since they do not involve strong force, they are usually the slowest reactions of the whole cycle, thus controlling its speed and the nucleosynthesis of involved elements. It is therefore important to directly measure their cross-sections at relevant energies, but because of their low occurrence probability, it is at the same time a complex task to fulfil.

All things considered, the reaction rate per particle pair for a direct capture reaction can be written as

$$\langle \sigma v \rangle = \left(\frac{8}{\pi \mu} \right)^{1/2} \frac{1}{(k_B T)^{3/2}} S(E_0) \int_0^\infty e^{-2\pi\eta} e^{-\frac{E}{k_B T}} dE = \left(\frac{8}{\mu} \right)^{1/2} \frac{\Delta}{(k_B T)^{3/2}} S(E_0) e^{-\frac{3E_0}{k_B T}} \quad (12)$$

Note that the S-factor has been taken out from the integral exploiting its weak energy dependence and the integral is evaluated using the Gaussian approximation of the Gamow peak.

¹The Q value is the energy absorbed or emitted by a reaction and is given by the energy difference between the reactants and the products. Namely, for a reaction $A + a \rightarrow B + b$, if m is the mass, we have $Q_{value} = c^2(m_A + m_a - m_B - m_b)$. If $Q > 0$ the reaction is exothermic and releases energy.

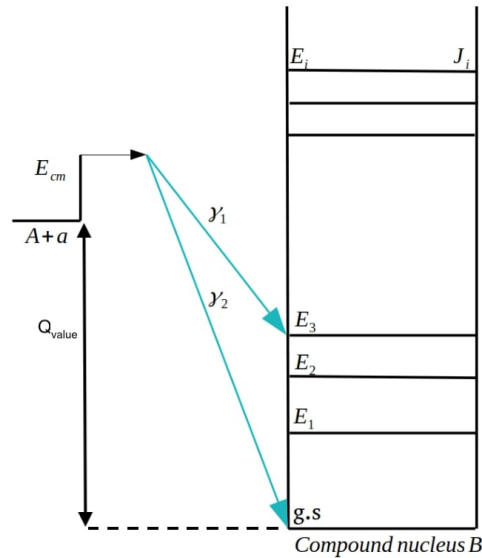


Figure 5: Direct capture reaction scheme.

2.2 Resonant reactions

A nuclear reaction can proceed through a resonant mechanism when the entrance channel (projectile plus target nucleus) has an energy that matches an energy level E_r of a compound nucleus. It is therefore a two-step process where an excited compound nucleus is formed and subsequently decays to lower lying states [2]. The resonant condition is given by

$$E_r = Q_{value} + E_{cm}$$

The excited state can decay either by photons or particles emission, producing a nucleus either equal or different from the compound one. These types of processes show a much stronger energy dependence in their cross-sections with respect to a non-resonant case. In Figure 6 a schematic representation of a resonant process is depicted, with E_R energy in the center of mass required to switch on the resonance.

Considering that the level E_r populated by the reaction decays to a lower level E_f via photon emission, the cross-section can be written as proportional to

$$\sigma \propto | \langle E_r | H_f | A + a \rangle |^2 | \langle E_f | H | E_r \rangle |^2$$

where we have two matrix elements, the first associated to the formation of the compound nucleus with energy E_r starting from the entrance channel $A+a$ and the second to the subsequent γ -emission populating the level with energy E_f . Each of these matrix elements corresponds to a partial² width Γ_i . According to Heisenberg's uncertainty principle, in fact, the energy of a nuclear level is not infinitely precise (in other words, it is not a Dirac delta). On the other hand, it has a certain energy width that makes it possible to achieve a resonant condition even when the entrance channel energy is not exactly E_r . Taking into account all the different ways in which the resonant level can be populated and de-excite, we can also introduce a total width as the sum of the partial widths of all the allowed formation/decay modes $\Gamma = \sum \Gamma_i$.

²Partial means that it refers to the specific decay mode involved.

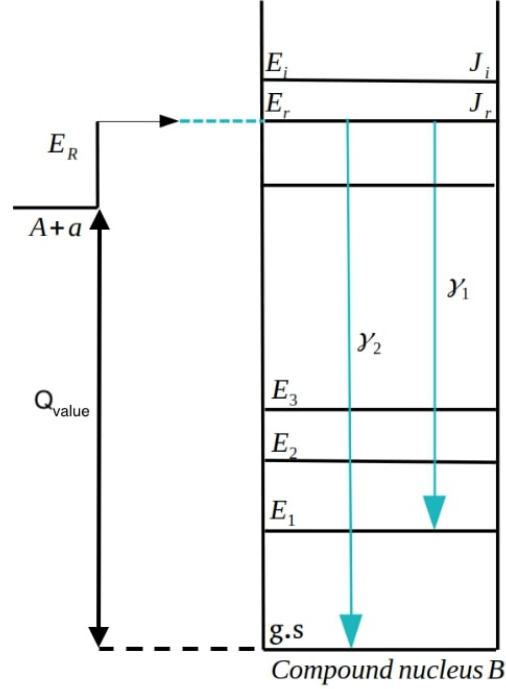


Figure 6: Resonant reaction scheme, with decay via photon emission.

For a resonant reaction, the cross section is well described by the Breit-Wigner formula

$$\sigma_{BW} = \pi\lambda^2 \frac{2J+1}{(2j_a+1)(2j_A+1)} (1 + \delta_{aA}) \frac{\Gamma_{ent}\Gamma_{ex}}{(E - E_R)^2 + (\Gamma/2)^2} \quad (13)$$

where

- $\lambda = \frac{h}{\sqrt{2\mu E}}$ is the De Broglie wavelength of the projectile in the center of mass system and $\lambda = \frac{\lambda}{2\pi}$
- j_a and j_A are the spin of the two interacting nuclei, while J is the spin of the excited state populated in the compound
- δ_{aA} is the Kronecker delta function, necessary to account for the increase in the cross-section for reactions between identical particles
- Γ_{ent} and Γ_{ex} are the partial width for the entrance and exit channel, while Γ is the total resonance width
- E_R is the energy of the resonance in the center of mass frame

One type of resonance is the **narrow resonance**, where the width of the resonance is smaller than the energy of the excited level $\Gamma \leq E_r$. In this case, the quantities λ , Γ_i and Γ are constant over the narrow energy width. Using the Breit-Wigner cross-section by Eq.13, the reaction rate per particle

pair in case of a narrow resonance is given by

$$\langle \sigma v \rangle = \left(\frac{8}{\pi\mu} \right)^{1/2} \frac{1}{(k_B T)^{3/2}} \int_0^\infty E \sigma_{BW} e^{-\frac{E}{k_B T}} dE = \left(\frac{8}{\pi\mu} \right)^{1/2} \frac{1}{(k_B T)^{3/2}} E_R e^{-\frac{E_R}{k_B T}} \int_0^\infty \sigma_{BW} dE \quad (14)$$

This expression is obtained considering that, since the resonance is narrow in energy, the factor $E e^{-\frac{E}{k_B T}}$ is varying very little over the resonance region and we can take its value at $E = E_r$ out from the integral. The remaining integral of the cross-section gives

$$\int_0^\infty \sigma_{BW} dE = 2(\pi\lambda)^2 \omega \gamma \quad (15)$$

where we have introduced the *resonance strength* $\omega\gamma$

$$\omega\gamma = \frac{2J+1}{(2j_a+1)(2j_A+1)} (1 + \delta_{aA}) \frac{\Gamma_{ent}\Gamma_{ex}}{\Gamma} = \omega \frac{\Gamma_{ent}\Gamma_{ex}}{\Gamma} \quad (16)$$

When $\frac{\Gamma}{E_r} \geq 10\%$, we speak of **broad resonance**. In this case, the Breit-Wigner cross-section has to be modified to take into account that λ , Γ_i and Γ have a non-negligible energy dependence. In this case the stellar reaction rate per particle pair is given by

$$\langle \sigma v \rangle = \frac{\sqrt{2\pi}\hbar^2\omega}{\mu(k_B T)^{3/2}} \int_0^\infty e^{-\frac{E}{k_B T}} \frac{\Gamma_{ex}(E_r)\Gamma_{ent}(E)}{(E - E_r)^2 + (\Gamma(E)/2)^2} dE \quad (17)$$

A final relevant type of resonance is the **sub-threshold** one. In this case we have that $Q_{value} > E_r$, but it is still possible to populate the high energy tail of the resonance because of the width of the level associated to E_r . This type of resonance can be modelled using the Breit-Wigner formula, but it is not always easy to take it into account. Still, it can play an important role in nuclear astrophysics, significantly increasing the reaction rate at relevant energies.

The above treatment is of course strictly valid when dealing with isolated resonances. If the resonances peaks are overlapping, complex interactions between them may have to be included, making the general treatment more difficult. If it is possible to neglect resonances interference, the total reaction rate can be written as the sum of non-resonant and resonant contribution.

All resonances lying close to the interacting particles threshold can completely dominate the reaction rate at low stellar temperatures and must be carefully included in nuclear networks calculations.

3 Astrophysical motivation

3.1 The $^{20}\text{Ne}(p,\gamma)^{21}\text{Na}$ reaction

The reaction that has been studied for this master thesis is a direct capture involving ^{20}Ne and a proton. It is an exothermic reaction with $Q_{\text{value}} = 2431.6$ keV.

A simple scheme of the reaction with most important gamma cascades from ^{21}Na de-excitation is shown in Figure 7. The thickness of the arrows in the figure reflects the so called *branching ratio*, a percentage that indicates how many of the reactions proceed through a specific decay scheme.

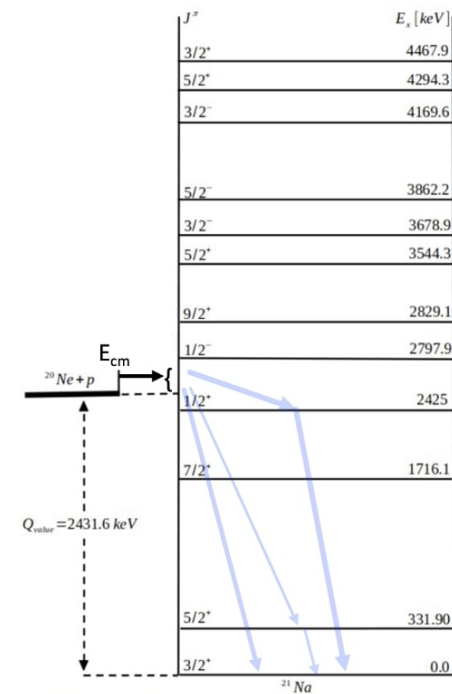


Figure 7: Schematic representation of $^{20}\text{Ne}(p,\gamma)^{21}\text{Na}$ direct capture. ^{21}Na energy levels are reported with the corresponding spin parity. The bluish arrows indicate the most important de-excitation channels involving photons emission in the gamma spectrum regime. Their thickness represents the relevance of the transition.

In Figure 8 the different processes that contributes to the reaction rate as function of stellar temperature are shown. Both resonant and non-resonant mechanisms have a role, with varying contribution to the total reaction rate. The relevant temperature range for the reaction in a star is approximately between 0.1 and 1 GK, as it will be explained in the next section. Within these values, the main contributions are the direct capture to the 2425 keV excited state and the resonance at $E_{cm} = 366$ keV.

In the following sections, the burning cycle in which $^{20}\text{Ne}(p,\gamma)^{21}\text{Na}$ reaction is involved will be presented, followed by a review of the most relevant stellar environments where the cycle is at work.

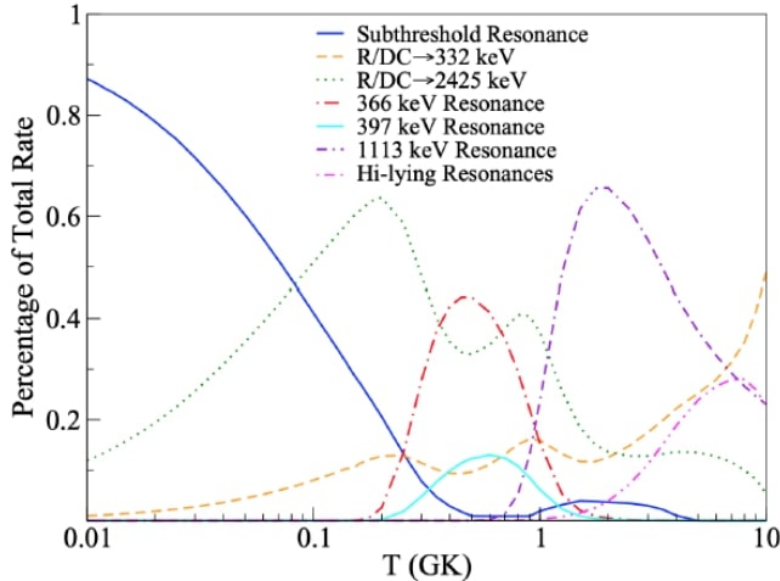


Figure 8: Different contributions to the total $^{20}\text{Ne}(p,\gamma)^{21}\text{Na}$ reaction rate. Figure taken from [3].

3.2 Neon-Sodium (Ne-Na) burning cycle

Hydrogen burning in stars mainly proceeds through two different paths, depending on the initial mass of the star. For stars less massive than $1.2 M_{\odot}$, lower temperatures favour the *pp chain* as the dominant energy source, while for more massive hotter stars the *CNO cycle* is the primary burning process. The net effect of both channels is the conversion of four protons into one helium nucleus through proton captures and β decays.

During the CNO cycle heavier carbon, nitrogen and oxygen nuclei are exploited as catalysts. It can proceed through different branchings depending on the achieved temperature [4]. When $T > 0.1 - 1$ GK, as in supermassive stars, accreting neutron stars, novae or supernovae outbursts, the *hot-CNO cycle (HCNO)* can be activated, involving also neutron deficient neon and sodium isotopes as catalysts.

A scheme of the CNO and hot-CNO cycle is reported in Figure 9. In the same scheme, the *neon-sodium cycle (NeNa)* is also highlighted. This is again a cycle of hydrogen burning using neon and sodium nuclei as catalysts that proceeds in stellar environment where temperature is greater than approximately 0.05 GK [5]. It can take place in many important astrophysical sites, such as hydrogen-burning shells of red giants, asymptotic giant branch stars (AGB), novae and massive stars core. Evidence for the NeNa cycle in red giants and novae had been found in the past ([6],[7]). The NeNa cycle does not represent an important source of energy generation, but its significance lies in the associated nucleosynthesis, which can also pave the way for higher mass isotopes production. The overall cycle rate impacts on the abundances of synthesized Ne, Na and Mg isotopes, among which ^{22}Na is an important stellar γ -ray signature and ^{22}Ne has a crucial role in neutron production for the s-process via the $^{22}\text{Ne}(\alpha, n)^{25}\text{Mg}$ reaction [8].

The whole NeNa cycle is initiated by the proton capture on ^{20}Ne nucleus. This nuclide can be either produced by a proton capture on ^{19}F or by the beta decay of ^{20}Na during HCNO cycle. Furthermore, a ^{20}Ne source can originate during helium burning ($^{12}\text{C}(\alpha, \gamma)^{16}\text{O}(\alpha, \gamma)^{20}\text{Ne}$) or carbon burning ($^{12}\text{C}(^{12}\text{C}, \alpha)^{20}\text{Ne}$) phases. In these two scenarios, however, we are dealing with more extreme

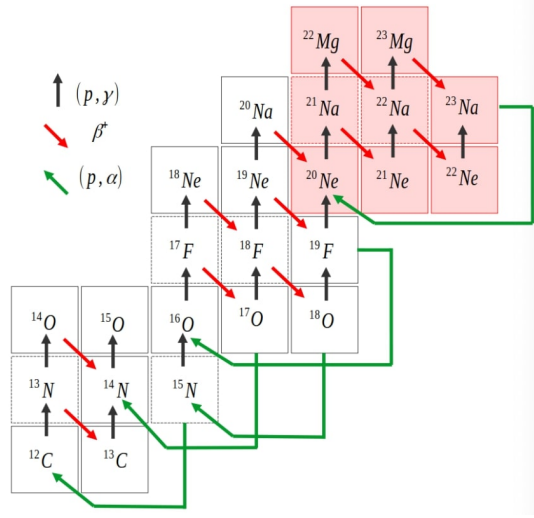


Figure 9: Reaction network of CNO-HCNO and NeNa (red boxes, starting from ^{20}Ne) cycles. Solid line boxes enclose stable nuclides, while radioactive ones are indicated by dashed lines.

conditions, where the rates are lower and do not contribute much to the overall involved isotopes production/destruction.

In Figure 10 a collection of reaction rate for the different reactions with their uncertainty involved in the cycle is shown. Their precise knowledge is fundamental to constrain the role of the cycle in stellar nucleosynthesis sites. In Table 1 the reaction rates available in literature at a temperature $T = 0.2$ GK are also listed, together with β^+ decay half-lives of the radioactive involved isotopes. The total cycle time is about $1.8 \cdot 10^5$ years and the slowest reaction is the $^{20}\text{Ne}(p, \gamma)^{21}\text{Na}$. As previously underlined, this implies that it sets the velocity of the entire cycle and constitutes a bottleneck for the production of the successive isotopes.

Reaction	β^+ decay ($T_{1/2}$)	$N_A \langle \sigma v \rangle$ [$\text{cm}^3 \text{mol}^{-1} \text{s}^{-1}$]
$^{20}\text{Ne}(p, \gamma)^{21}\text{Na}$	^{21}Na (22.5 s)	$4.57 \cdot 10^{-6}$ [3]
$^{21}\text{Na}(p, \gamma)^{22}\text{Mg}$	^{22}Mg (3.9 s)	$1.99 \cdot 10^{-2}$ [11]
$^{21}\text{Ne}(p, \gamma)^{22}\text{Na}$	^{22}Na (2.6 yr)	$2.01 \cdot 10^{-4}$ [9]
$^{22}\text{Na}(p, \gamma)^{23}\text{Mg}$	^{23}Mg (11.3 s)	$2.76 \cdot 10^{-2}$ [11]
$^{22}\text{Ne}(p, \gamma)^{23}\text{Na}$		$3.68 \cdot 10^{-2}$ [11]
$^{23}\text{Na}(p, \alpha)^{20}\text{Ne}$		$1.47 \cdot 10^{-2}$ [11]

Table 1: Reaction rates at a temperature $T = 0.2$ GK from literature and half lives of the NeNa cycle β -unstable isotopes from National Nuclear Data Center.

Until few years ago, the uncertainties connected to the NeNa cycle were governed by the $^{22}\text{Ne}(p, \gamma)^{23}\text{Na}$ reaction. This reaction was however recently deeply studied at LUNA ([12], [13], [14], [15]) and thanks to the combination of these results with other studies ([16], [9]) its reaction rate uncertainty was significantly reduced. Presently the major source of uncertainty are the $^{20}\text{Ne}(p, \gamma)^{21}\text{Na}$ and $^{23}\text{Ne}(p, \alpha)^{20}\text{Ne}$, the first and last cycle reactions [16]. An improvement in their cross-section determination can help the understanding of several astrophysical nucleosynthesis scenarios. In this optic, the entrance channel has been explored at LUNA during the campaign presented in this thesis, in order to better constrain the reaction rate and reduce the overall uncertainties in the input to nucleosynthesis models.

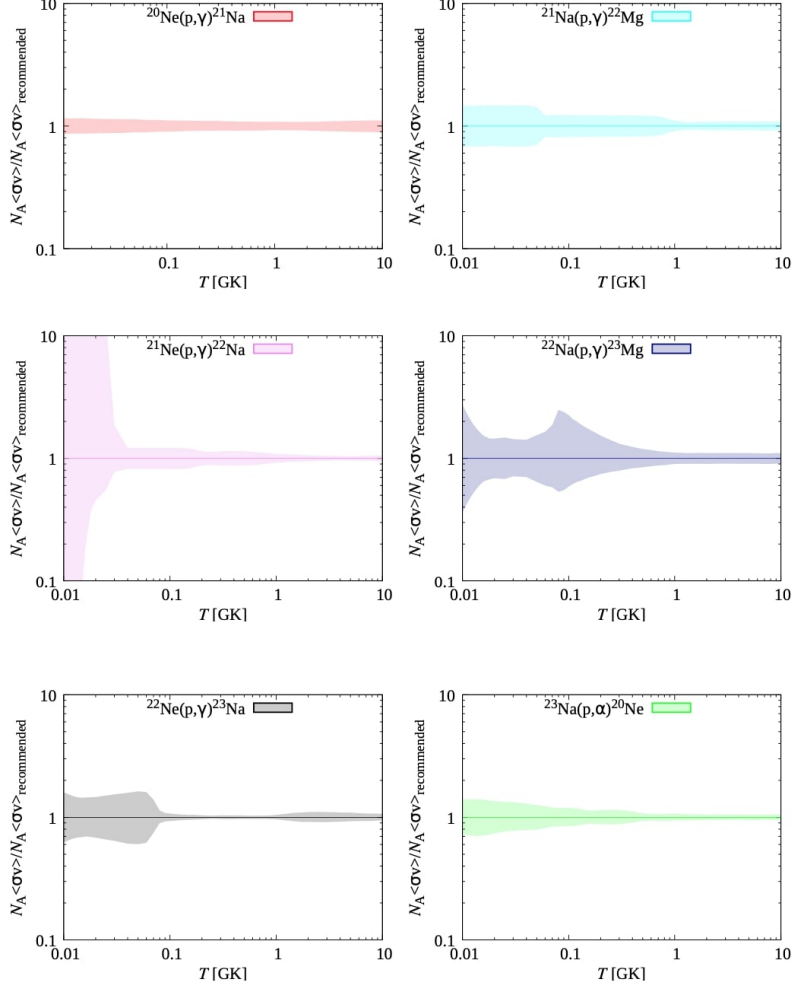


Figure 10: Thermonuclear reaction rates for all nuclear reactions involved in the NeNa cycle. the $^{20}\text{Ne}(p,\gamma)^{21}\text{Na}$ reaction rate has been taken from the most recent work by [3], the $^{22}\text{Ne}(p,\gamma)^{23}\text{Na}$ one from [9], the remaining from [10].

3.3 RGB stars, Globular Clusters and AGB stars

Red Giant Branch (RGB) are stars in which hydrogen has been exhausted in the core and it is now burning in a thin shell around it. It is a transition phase towards core helium burning via 3α reaction³, which can be onset only when the core mass, enriched in helium by the H-shell burning, reaches a certain threshold. During this phase, as the shell burns outwards, the core contracts because of the lack of a nuclear energy source to counteract the gravitational force. The outer layers conversely expands until a convective envelope develops. Typical RGB star structure is schematically reported in Figure 11.

Globular Clusters (GC) are tight spherical distribution of old gravitationally bound stars, orbiting in the extended halos that surrounds most spiral galaxies. Their old age, estimated from their low metallicity content, provide an evaluation of the age of the galaxy to which they belong and, consequently, a lower limit constrain to the age of the Universe. As for GCs origin, it was generally

³This is a two step nuclear process burning carbon out of three helium nuclei: 1) $4\text{He} + 4\text{He} \rightarrow {}^8\text{Be} + \gamma$ 2) $4\text{He} + 8\text{Be} \rightarrow {}^{12}\text{C} + \gamma$



Figure 11: Schematic illustration of the structure of an RGB star.

assumed that all stars belonging to a cluster were formed during a single massive star formation event: this implies that all members have the same age and the same initial chemical composition. However, this assumption was undermined by observations of globular cluster red giants with high resolution spectrometers, opening new scenarios on stellar evolution and galactic chemical evolution. GCs actually host stars with different ages and very different composition [17]. One of the most striking features concerns the abundance of light elements, showing for example O-Na and Mg-Al anticorrelations in GC stars on the Red Giant Branch [18]. The O-Na anticorrelation in particular has been deeply explored combining improved LUNA reaction rates for $^{22}\text{Ne}(p,\gamma)^{23}\text{Na}$ and AGBs evolution models with different prescription in [19]. In Figure 12 the anticorrelated behaviour of sodium and oxygen are clearly shown. Oxygen depletion and sodium enrichment are the results

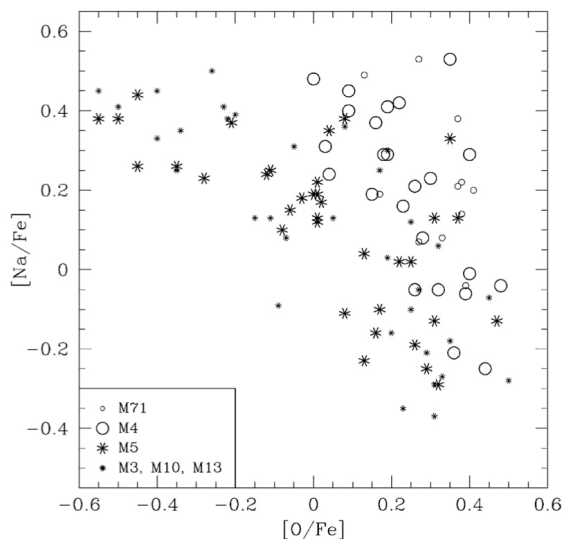


Figure 12: Anticorrelation between sodium and oxygen relative abundances for observed cluster of intermediate metallicity, from [20].

of the combined action of the ON (within CNO) and NeNa cycles in hydrogen burning regions at $T > 40\text{MK}$. Proton capture on ^{20}Ne nuclei at low temperature [21], together with a reduction factor of 2-4 in the $^{23}\text{Na}(p,\alpha)^{20}\text{Ne}$ [22], could solve the observed abundances and explain the origin of the anticorrelation. In general, it has to be stressed that currently stellar models cannot reproduce exactly the situation, either because of a wrong or incomplete astrophysical theory or a lack in the nuclear reaction database.

Still, the mechanism bringing the ashes of the aforementioned hydrogen burning cycles to star surface, regardless of the abundance they are produced with, should be somehow explained. The main hypotheses that have been developed are a deep mixing event occurring during the RGB phase or the existence of old polluting stars which had injected processed material in the interstellar medium from which new stars had then formed [21].

The most promising candidate as polluters of early proto-clusters are *Asymptotic Giant Branch* (AGB) stars undergoing hot bottom burning⁴. The AGB phase is a late stage of stellar evolution between helium and carbon burning. AGB stars structure consists of a partially degenerate carbon-oxygen core, an helium burning shell and a thin hydrogen burning shell separated by an intershell region, and an extended convective envelope, as depicted in Figure 13. CNO cycle at work in

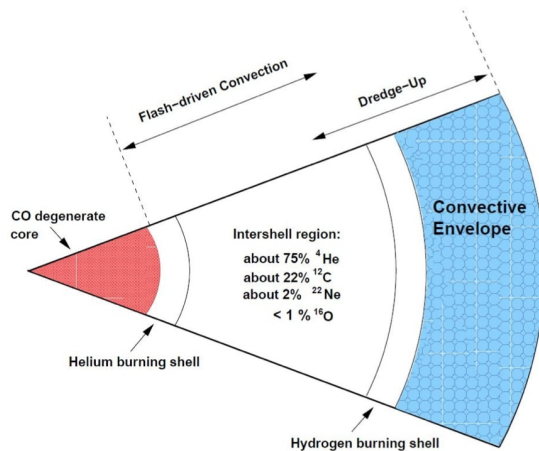


Figure 13: Schematic illustration of the structure of an AGB star. Taken from [24]

the hydrogen shell provides enough energy to sustain the star for long periods, interrupted by the unstable activation of the inner helium burning shell (helium flash), developing the so called *thermal pulses*. This violent ignition leads to the onset of convection in the intershell zone and to the temporary extinction of the hydrogen shell, pushed outwards by outer layers expansion. Moreover, during pulses the convective envelope is able to penetrate towards the intershell, bringing the newly synthesized materials to the surface (Third Dredge Up (TDU)).

Hot bottom burning is a nuclear burning phase involving CNO, NeNa and MgAl cycles. It can take place in intermediate-mass AGB stars ($M > 4M_{\odot}$), where the basis of the convective envelope reaches temperature of 60-100 MK [25]. The hydrogen burning products are then brought to the surface through TDU events and ejected through strong stellar wind, enriching the interstellar medium.

Stellar models trying to reproduce HBB nucleosynthesis and successive interstellar medium chemical enrichment have many inputs to be known with high precision. The efficiency of the process has a strong metallicity dependence and there are only few observations that can significantly constrain it. An accurate knowledge of all the nuclear reactions involved in the cycles involved in HBB is therefore required, especially for those with highest reaction rate uncertainty, such as $^{20}\text{Ne}(p,\gamma)^{21}\text{Na}$ one. To underline this, in the top-left of Figure 14 the correlation between final ^{23}Na abundance and the $^{20}\text{Ne}(p,\gamma)^{21}\text{Na}$ reaction rate is shown: the impact is clearly high. Also other cycle reaction

⁴Other possible contributors to this pollution mechanism are fast rotating very massive stars [23].

rates effects are depicted. These results are part of Monte Carlo post processing nucleosynthesis calculations for thermal pulsing AGBs including a total of 176 nuclear species and 1657 nuclear reactions [26]. For each network's reaction the rate is varied according to the distribution of its associated error. This variation can be then expressed in terms of fraction p_i of the rate standard deviation. If the rate does not affect the considered element final abundance, there should be no correlation between it and p_i values (horizontal line), as in the case of the bottom right plot in Figure 14.

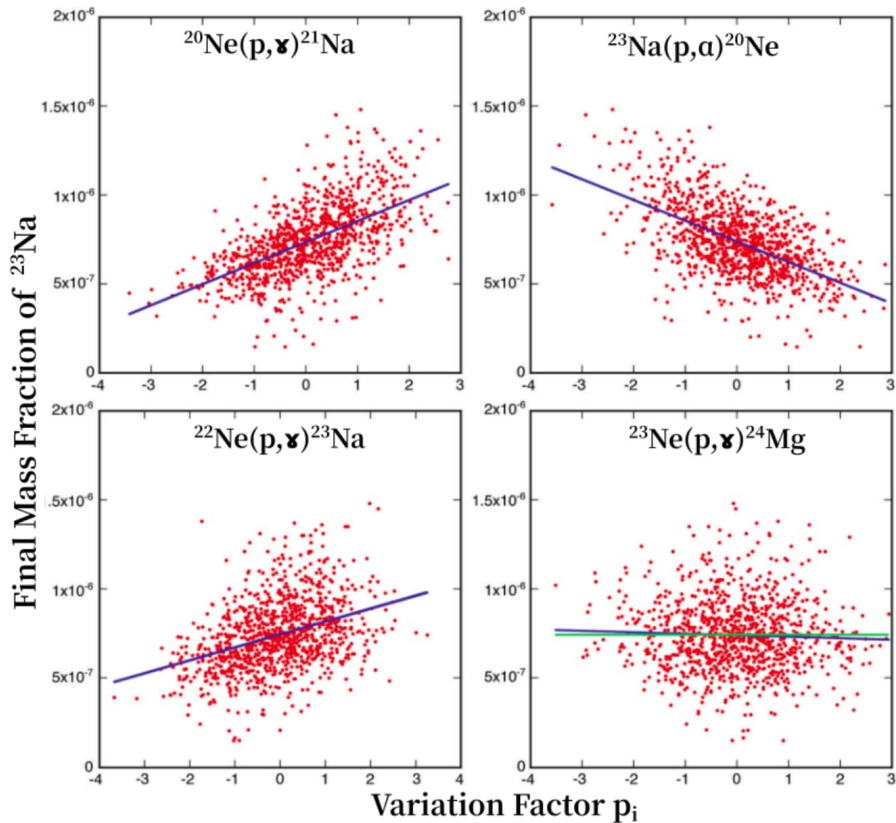


Figure 14: Correlations between the final abundance of ^{23}Na and the rate-variation factor p_i for each of the 1000 samples of the reaction network. The blue lines are linear fits to the correlations. Figure taken from [26].

3.4 One classical novae and Type Ia supernovae

During their AGB and post-AGB phase low and intermediate-mass stars ($M \lesssim 13M_{\odot}$) experience several instabilities and strong mass loss events, ending their life as white dwarfs (WD). WDs are bare degenerate cores supported by degeneracy pressure, slowly cooling down in absence of ongoing nuclear reactions. The core can be either made of carbon and oxygen, in case the last fuel burning was helium, or neon and oxygen, if the star was able to reach the carbon burning stage in its previous evolution.

When one of such objects is in a close binary system with a main sequence (MS) companion star, part of the H-rich material can be transferred from the MS star and accreted onto the WD surface [27] (see Figure 15 for a pictorial representation of the process). If the accretion rate is smaller or

equal to $10^{-7} - 10^{-8} M_{\odot}$, the fresh material is gradually compressed until its temperature reaches a critical point between 0.15 and 0.4 GK [28]. A thermonuclear runaway ignition of outer layers takes place, ejecting the WD envelope into the interstellar medium [27]. These phenomena are known as *classical novae explosion* and represent the most common explosive events in a galaxy, giving important contribution to galactic chemical evolution. During such explosion, the WD is not completely disrupted and can therefore accrete material again and the whole process may be periodically repeated.

The chemical abundances of some of the elements ejected by novae can be used as thermometers for the explosion, since their ratios presents a strong monotonic dependence on the peak temperature. Several studies ([27], [29]) have shown that the peak temperature during the H-burning in classical novae is lower than 400 MK. The CNO cycle proceeds slowly at such temperatures, hence the final abundances stay approximately unchanged during the explosion. In particular, since the proton capture on ^{20}Ne is very slow at novae temperatures (0.1-0.4 GK on surface), most of the neon nuclei produced in star earlier evolution phases are still present after the thermonuclear runaway. Indeed, the ONe novae, which are the most energetic among novae, have been firstly discovered from their ejecta⁵ spectroscopic analysis, which showed strong Ne II lines.

For what concerns NeNa rate impact on classical novae models, a sensitivity study [30] has analyzed the effects of reaction rates variation on the ejecta, finding strong consequences for elements with mass number $A < 40$. Their calculations, involving 176 nuclear species and 1657 nuclear reactions, has shown that ONe nova models that achieve very high peak temperatures require reduced NeNa rate uncertainties to provide accurate ^{20}Ne abundances, which is the dominant neon isotope released by the explosion.

An alternative event that can take place in the binary system is a *Type Ia supernova* explosion. In case of high accretion rate and large WD masses, the accreting star can overcome the Chandrasekhar mass ($\sim 1.44 M_{\odot}$) and ignites explosive thermonuclear reactions throughout the whole star, leading to its total disruption [31]. This explosion is characterized by a light curve powered by the decay of produced radioactive ^{56}Ni , which presents a peculiar fixed magnitude at their maximum. This fact makes SNe optimal standard candles for measuring cosmological distances and probing the geometry of our Universe [31]. Nonetheless, theoretical models which aim at reproducing the full nucleosynthetic output of a SN Ia must include a complex nuclear reaction network with thousands of reactions, requiring as low as possible reaction rate uncertainties [32].

4 State of the art

As previously underlined, the knowledge of $^{20}\text{Ne}(p, \gamma)^{21}\text{Na}$ reaction details is crucial to give a comprehensive account of the outcome of NeNa cycle. In the literature, however, only few measurements have been performed, using both direct and indirect approaches. The most relevant experimental studies and their results will be briefly reviewed in the following.

Tanner et al. 1959 [33]

The non-resonant component of the $^{20}\text{Ne}(p, \gamma)^{21}\text{Na}$ reaction was studied at an energy in the center of mass of $E_{cm}=600$ keV and 1050 keV. A solid neon target, produced bombarding water-cooled

⁵We speak of yields when we indicate the amount of material newly synthesized in the star, while the term ejecta represents the material ejected in the interstellar medium from the star, also including pre-existing amounts.

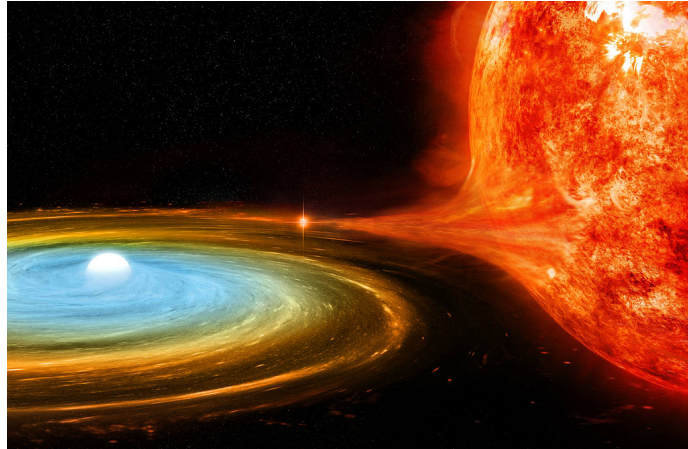


Figure 15: Pictorial representation of a white dwarf accreting material from a main sequence companion star.

thin aluminium backing with 50 keV neon ions, was hit by a proton beam. Experimental yields were then measured from delayed positrons emission from ^{21}Na decay (half life $\tau = 23$ s). To allow the measurement of β activity decay curve, the target was mounted off-axis in a vacuum sealed shaft, which could be rotated to move the target out of the proton beam and close to the β counter. This was a plastic scintillator mounted in close geometry, with a size comparable to the maximum energy of the ^{21}Na positrons. The results for cross-section and S-factor are reported in Table 2. For $E_{cm} = 600$ keV only an upper limit could be estimated. The extrapolated S-factor at zero energy S_0 has a value of 66 keV barn with an uncertainty factor of three. The authors also underlined that at thermal energies the contribution to S_0 from the tail of the 2425 keV resonant state should be considered. Adopting values from Marion and Fowler (1957) [5], they gave a final value of $S_0 = 80$ keV barn

E_{cm} (keV)	σ (μbarn)	S-factor (keV barn)
600	< 0.14	< 25
1050	1.3 ± 0.2	17 ± 3

Table 2: Cross-sections and S-factor for $^{20}\text{Ne}(p,\gamma)^{21}\text{Na}$ by [33].

Van der Leun et al., 1964 [34]

Three resonances at $E_p^6 = 1169, 1955, 2138$ keV were found and studied using a thin target made of ^{20}Ne adsorbed on tantalum and the proton beam from the 3.2 MV Van Der Graaff accelerator of the Utrecht University. Gamma spectrum from the reaction was obtained using 10cm x 10cm NaI crystals enclosed in 10 cm thick lead shielding. The detector was located at 1 cm from the target and at 55° with respect to the proton beam. The spectra could be acquired either as single or in coincidence mode. Resonance yields curves, indicating the reaction yields slightly varying the energy around the resonance one, were explored in the range 2.2-2.6 MeV with 2-6 keV energy steps. Only transitions from the resonant levels to the ground and first excited state were considered in the analysis, determining the corresponding intensities.

⁶ E_p refers to beam energies in the laboratory rest frame. The conversion from lab to center of mass frame is performed according to $E_{cm} = E_p \cdot \frac{m_{\text{target}}}{m_{\text{target}} + m_{\text{projectile}}}$.

The widths and strengths of the resonances are reported in Table 3

E_p (keV)	Γ (keV)	$\omega\gamma$ (eV)
1169 ± 2	3.5	1.13 ± 0.07
1955 ± 4	5.3 ± 1.0	4.0
2138 ± 5	21 ± 3	1.6

Table 3: Resonance widths and strengths for $^{20}\text{Ne}(p,\gamma)^{21}\text{Na}$ obtained by [34]. The resonance strengths are normalized to the resonance strength of 1.13 ± 0.07 eV for the 1169 keV resonance reported in Thomas and Tanner (1960) [35].

Rolfs et al., 1975 [36]

The $^{20}\text{Ne}(p,\gamma)^{21}\text{Na}$ reaction was widely studied in the energy range between $E_p=0.37$ and 2.10 MeV. Using the California State University's Van Der Graaff accelerator a proton beam was delivered on an extended natural neon windowless gas target. The gas was purified using a LN₂ trap. Beam currents were not measured, but in order to monitor beam intensity, target density and contaminants level, a collimated silicon detector was placed at 135° to detect protons elastically scattered. Photons emitted by the reaction were collected by two Ge(Li) detectors placed at 0° and 90° with respect to the beam direction.

The analysis led to the determination of excitation energies and branching ratios for ^{21}Na states, as well as a re-measurement of the Q_{value} of the reaction ($Q_{value} = 2432.3 \pm 0.5$ keV). In particular, a new resonance at $E_{cm} = 384 \pm 5$ keV (corresponding to an excited state at $E_x = 2797.6$ keV) was found. Values for the cross-sections of different direct capture transitions were also evaluated. A summary of these results is given in Table 4 and 5.

Transition (MeV)	σ (μbarn)
$DC \rightarrow 0$	< 0.012
$DC \rightarrow 0.33$	0.32 ± 0.05
$DC \rightarrow 1.71$	< 0.007
$DC \rightarrow 2.43$	0.63 ± 0.07
$DC \rightarrow 2.80$	< 0.012
$DC \rightarrow 2.83$	< 0.006

Table 4: Direct capture (DC) transitions and cross-sections for $^{20}\text{Ne}(p,\gamma)^{21}\text{Na}$ by [36] at $E_p=1050$ keV.

Excitation energies (keV)
332.0 ± 1.0
1716.3 ± 1.3
2425.2 ± 0.4
2797.6 ± 1.4
2829.4 ± 1.4
3544.8 ± 0.6
4175 ± 15
4295 ± 2

Table 5: ^{21}Na excitation energies in keV found by [36].

The authors gave an estimate of $S_0=3500$ keV barn, based on their experimental results. They

have also calculated the S_0 using the formula found by Marion and Fowler (1957) [5] $S_0 = 1.3(E - E_r)^{-2} \cdot 10^{14}$ eV barn, where $E - E_r$ given in eV is the binding energy of the considered state. They have found that the 2425 keV state is involved in the dominant gamma decay channel, and using their experimental value $(E - E_r) = 7.1 \pm 0.6$ keV, their estimate for S_0 became 2600 keV barn. They concluded that their high S-factor value showed very fast ^{20}Ne burning into ^{21}Na , which subsequently undergoes β^+ decay into ^{21}Ne .

Keinonen et al., 1977 [37]

This study performed at Helsinki University was focused on the $^{20,21,22}\text{Ne}(p,\gamma)^{21,22,23}\text{Na}$ reactions in the energy range $E_p = 0.5 - 2.0$ MeV. Neon ions with energies between 5 and 50 keV were implanted into 1 mm thick carbon backings. Then, an alpha beam was sent on the target to analyse its composition and possible contaminants from the spectrum of the back-scattered α particles, finding a Ne/C atoms ratio of 0.1. Proton beam from 2.5 MV Van Der Graaff accelerator was then delivered on the solid targets, producing gamma photons detected with a Ge(Li) detector placed at 55° with respect to the beam line.

Many resonance strengths were measured. For $^{20}\text{Ne}(p,\gamma)^{21}\text{Na}$ reaction, $E_p = 1169$ keV resonance measurement gave a value of $\omega\gamma = 1.6 \pm 0.3$ eV. Consequently, a value of $S_0 = 2500$ keV barn was evaluated, in good agreement with the value presented by Marion and Fowler (1957) [5]. Fast hydrogen burning of ^{20}Ne was confirmed, mainly due to the high cross section of the sub-threshold resonance at $E_r \approx -7.1$ keV.

Mukhamedzhanov et al., 2006 [38]

The authors provided an indirect measurement of $^{20}\text{Ne}(p,\gamma)^{21}\text{Na}$ reaction rate focusing on the capture to the ground state through the tail of the 2425 keV sub-threshold resonance state. The normalization to the direct capture of this state and its partial width were calculated using the asymptotic normalization coefficient (ANC) formalism⁷. The experiment was performed at Nuclear Physics Institute of the Czech Academy of Sciences, delivering 25.83 MeV ^3He beam from the U-120M isochronous cyclotron on a high-purity isotopic ^{20}Ne (99.99%) gas target. Reaction products were measured by a pair of collimated ΔE -E telescopes consisting of 220- μm Si surface barrier detectors and 4-mm-thick Si(Li) detectors. The value for S_0 given in this work took into account both the direct capture and resonant contribution involving the sub-threshold state indicated above and amounts to 5900 ± 1200 keV barn. This is higher than S_0 from Rolfs et al. (1975) [36]: according to the authors this is due to their more accurate extrapolation of the S-factor down to zero energy.

Lyons et al., 2018 [3]

The direct cross-section of $^{20}\text{Ne}(p,\gamma)^{21}\text{Na}$ reaction was measured in a wide proton energy range between 500 keV and 2000 keV. The measurements were performed using the 5U-4 accelerator at the Nuclear Science Laboratory at the University of Notre Dame and a differentially pumped gas target of isotopically enriched ^{20}Ne gas. Transitions to the ground state and to the 331.5 and 2425 keV excited states were observed using an HPGe detector with 100% relative efficiency⁸, placed at 90° , with respect to the beam line. This work determined the contribution of the sub-threshold resonance

⁷Details on the technique can be found in [39].

⁸HPGe detector efficiency is usually expressed as the efficiency relative to the one of a 7.6 cm x 7.6 cm (diameter x height) NaI(Tl) crystal, based on the 1.33 MeV peak of a ^{60}Co source positioned at 25 cm from the detector.

and of the direct capture to the total cross-sections performing an R-matrix fit of experimental data. Results for the S-factor are reported in the summarizing Figure 16,17,18. Finally, an improved total reaction rate was given, showing an overall reduction of 20% with respect to the previous reaction rate libraries from Iliadis et al. (2010) [10].

A.L. Cooper, PhD thesis, 2019 [40]

This work was focused on the measurement of the $E_p = 384$ keV resonance and on the direct capture at $E_p=330$ keV. The reaction was reproduced at Laboratory for Experimental Nuclear Astrophysics (LENA) making a proton beam ($E_p = 380 - 404$ keV for the resonant component) from the JN accelerator impinge on a target of neon implanted on tantalum backings. The yield from the 373 keV peak (arising from the subsequent decay of the 2798 keV state populated by the resonance to the 2425 keV state) was obtained at each proton energy through the $\gamma\gamma$ Coincidence Spectrometer of LENA. This apparatus consists of three detector clusters: an HPGe crystal closely positioned at 0° behind the target, a segmented array of 16 thallium-doped sodium iodide (NaI(Tl)) scintillating detectors and five plastic scintillator panels that encase the other two clusters on the sides and on the top. The 384 keV resonance strength was estimated for several targets, giving a final weighted average value of $\omega\gamma = (7.22 \pm 0.68) \cdot 10^{-5}$ eV. This value disagrees with the one previously presented by Rolfs et al. (1975) [36]. Another disagreement is found in the branching ratios, especially in the weakest branch involving the 331.5 keV state, as shown in Table 6.

Transition (keV)	Branching ratio % (Rolfs et al. (1975))	Branching ratio % (Cooper (2019))
2797.5 \rightarrow 2425.9	56.4 ± 4	61.5 ± 7.3
2797.5 \rightarrow 331.5	$11 \pm$	1.6 ± 1.1
2797.5 \rightarrow 0	33 ± 4	35.9 ± 5.3
$\omega\gamma [10^{-4} \text{eV}]$	1.1 ± 0.2	0.722 ± 0.068

Table 6: Comparison between branching ratios for the $E_p = 384$ keV resonance (upper part) and resonance strengths (lower part), from [36] and [40].

For what concerns the direct capture component, due to background contamination it was not possible to clearly distinguish it from the resonant capture to the 2425 keV sub-threshold state. Therefore, only an upper limit on DC contribution to the total cross-section was given. In conclusion, an average S-factor of $S_{tot}(E_{eff}^{lab}) = (2.84 \pm 0.37)$ keV barn at 334 keV proton energy was found.

J. Karpesky, PhD thesis, 2020 [41]

The reaction was studied at the DRAGON facility (TRIUMF) using an inverse kinematics approach. The center of mass energy range 265.5 - 519.6 keV was explored using isotopically pure ^{20}Ne ion beam on an hydrogen windowless gas target. Produced photons were detected with a BGO scintillator array consisting of 30 closely packed scintillation detectors, reaching an angular coverage of approximately 90%. At four beam energies, cross-sections and S-factor for the transitions $R/DC^9 \rightarrow 0$ keV, $R/DC \rightarrow 331.5$ keV and $R/DC \rightarrow 2425$ keV were obtained. The evaluated total S-factor is reported in Table 7.

Of note, the results for the total S-factor within this work are consistently lower than results presented in prior experiments performed by Rolfs et al. (1975) [36] and Lyons et al. (2018) [3].

⁹This notation indicates both resonant and direct capture components, which were not distinguishable.

E_{cm} (keV)	S-factor (keV barn)
265.5	21.9 ± 4.7
319.0	13.5 ± 3.5
441.9	13.4 ± 1.6
519.6	12.7 ± 1.4

Table 7: Total S-factor measurements for $^{20}\text{Ne}(p,\gamma)^{21}\text{Na}$ reaction at the four beam energies explored at DRAGON by [41].

Moreover, experimental data seems to suggest a higher than originally expected contribution of the direct capture directly to the ground state at lower energies, disagreeing with the flat behaviour found by [36], but compatible with the suggested R-matrix trend by [3].

As previously pointed out, the $^{20}\text{Ne}(p,\gamma)^{21}\text{Na}$ reaction sets the timescale of the NeNa cycle. Precise data on reaction cross-sections and deep knowledge of ^{21}Na energy levels are therefore needed to determine an accurate total reaction rate and detailed final abundances of isotopes synthesized in the cycle.

Current adopted level scheme for ^{21}Na has already been shown in Figure 7, while S-factor values for the direct capture to the 0, 331.5, 2425 keV states from [36], [3] and [41] are reported in Figure 16, 17 and 18. The reaction rates available in literature over a quite wide temperature range are reported in Figure 19. In particular, the new experimental data given by Lyons et al. (2018) [3] produce a lower rate at low temperatures below 1 GK and an overall reduction of the rate uncertainty.

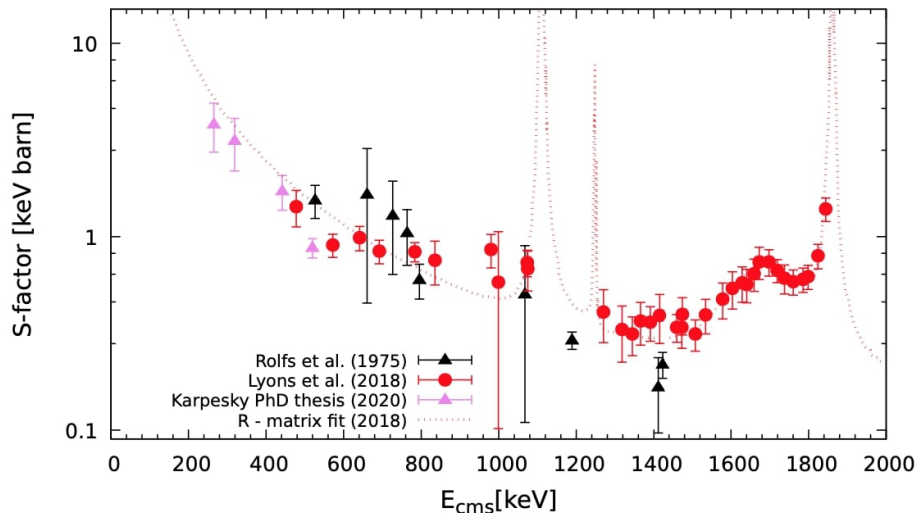


Figure 16: $DC \rightarrow 0$ keV state S-factor for $^{20}\text{Ne}(p,\gamma)^{21}\text{Na}$ reaction from [36], [3] and [41]. Figure from [42].

5 The LUNA experiment

The main goal of experimental nuclear astrophysics is to measure cross-sections of nuclear reactions relevant for astrophysics. At stellar temperatures, these cross-sections are extremely low, down to femtobarn, thus creating the necessity to increase as much as possible the *signal to noise* ratio,

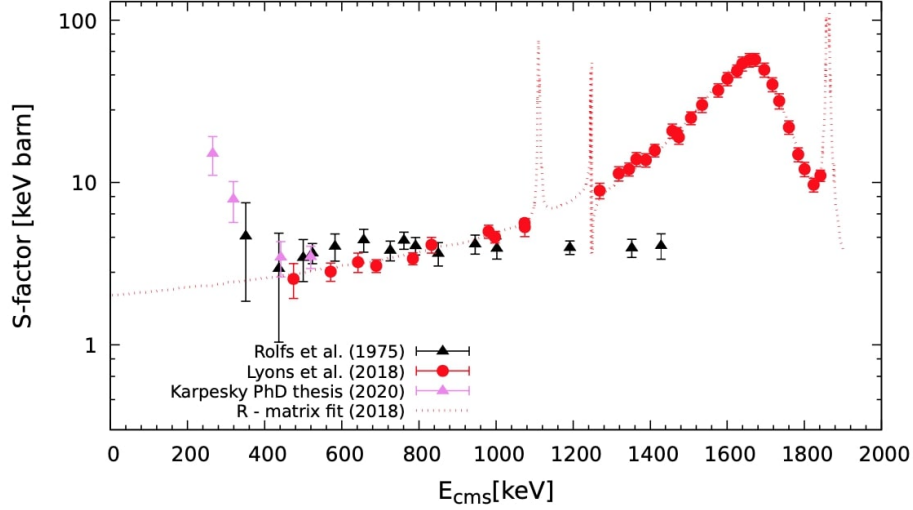


Figure 17: $DC \rightarrow 331.5$ keV state S-factor for $^{20}\text{Ne}(p, \gamma)^{21}\text{Na}$ reaction from [36], [3] and [41]. Figure from [42].

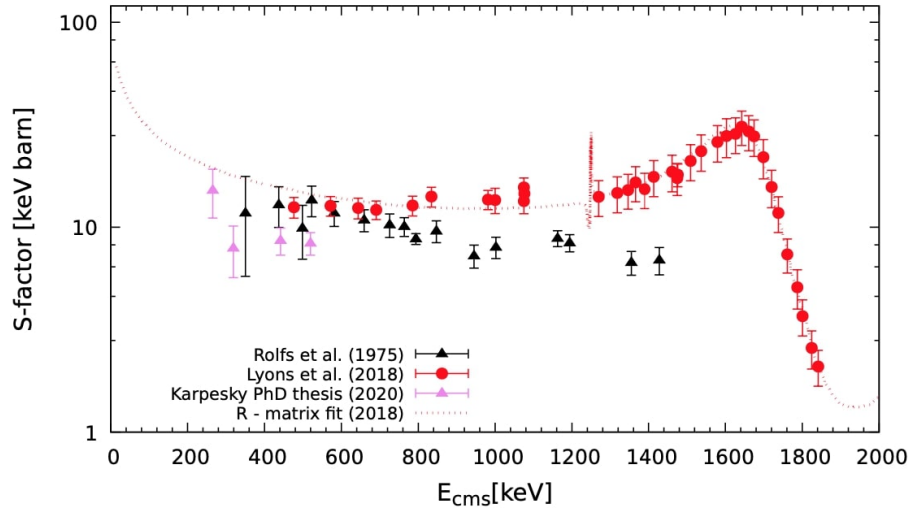


Figure 18: $DC \rightarrow 2425$ keV state S-factor for $^{20}\text{Ne}(p, \gamma)^{21}\text{Na}$ reaction from [36], [3] and [41]. Figure from [42].

especially when dealing with radiative captures.

In a typical nuclear astrophysics experiment, a beam of projectile nuclei is accelerated towards the target nuclei, which can be either in a solid or gaseous state, either pure or in some compounds. It follows that the achievable signal is limited by the accelerator capability¹⁰ and by the need to not destroy or deteriorate too much the target with too high beam currents. Another things that has to be considered when trying to achieve a good signal is that all layers with which the beam interacts are a source of beam energy loss and as the energy decreases also the cross-section steeply decreases.

One of the possible successful approach is therefore to reduce as much as possible the background in

¹⁰The higher is the beam intensity that the accelerator can produce, the higher will be the number of projectiles in the beam and the more reactions will be produced by projectile-target interaction.

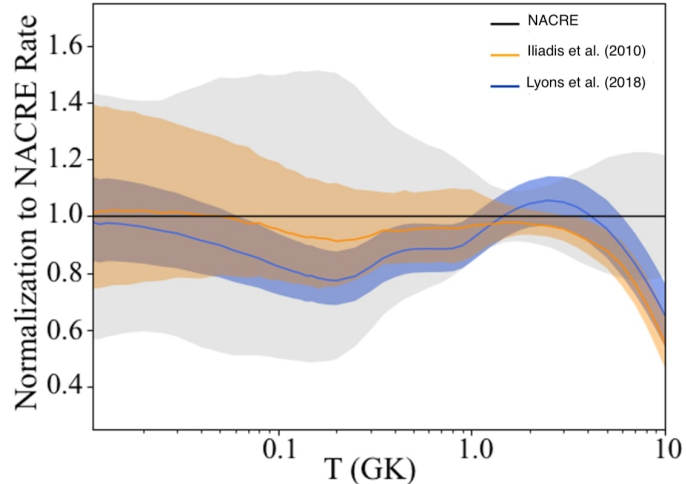


Figure 19: Total $^{20}\text{Ne}(p, \gamma)^{21}\text{Na}$ reaction rate $N_A \langle \sigma v \rangle$ versus temperature given in Iliadis et al. (2010) [43] and Lyons et al. (2018) [3] compared to that of NACRE [44], including respective error bands as shadow areas. Values are normalized to NACRE data.

the spectra. In this context, LUNA (Laboratory for Underground Nuclear Astrophysics) has been developed in 1991 with the aim of suppressing considerably cosmic rays-originated background by performing experiments in deep underground (see Section 5.4 for further details).

LUNA is located at Gran Sasso National Laboratories (Italy) (LNGS), which are naturally shielded against cosmic radiation by 1400 meters of mountain rocks (3800 meters of water equivalent¹¹). Over the last decades, LUNA has provided valuable contribution to our present understanding of primordial and stellar nucleosynthesis during hydrogen and helium burning [45]. The experiment started in 1993 with a homemade 50 kV accelerator, installed at the underground facilities of LNGS and operating until 2003. The LUNA-50 kV accelerator has been used primarily to study H-burning reactions relevant for our Sun, producing important results [46]. Since 2001, LUNA-400 kV accelerator has been operating to study Big Bang nucleosynthesis and CNO, NeNa and MgAl cycles [47]. Next year (2023) a new machine will finish being installed at LNGS. Its terminal voltage up to 3.5 MV will allow to study more advanced stages of nuclear burning, in particular C-burning [45].

5.1 400 kV Accelerator

LUNA 400 kV accelerator is a commercial single-ended electrostatic accelerator [47], built by High Voltage Engineering Europe (HVEE) (Netherlands).

The machine is enclosed in a tank filled with an insulating gas mixture composed of N_2 (75%), and CO_2 (25%) at 20 bar. The high-voltage is generated by an Inline-Cockroft-Walton power supply and stabilized by an RC filter located at the power supply module and by an active feedback loop based on a chain of resistors.

A radio-frequency ion source (see Figure 20) is mounted in the accelerator tube and provides stable proton or α beams with intensities on the target respectively up to 500 μA and 250 μA . Long-term stability, high intensity and contained beam spread are crucial parameters for measuring low and

¹¹This indicates the amount of water that produces the same flux attenuation and it is useful for comparison with other underground laboratories.

highly energy-dependent astrophysical cross-sections. LUNA 400 kV accelerator is able to provide all of them. The beam has a long term stability of 5 eV/h and its energy spread has been measured to be about 100 eV [47].

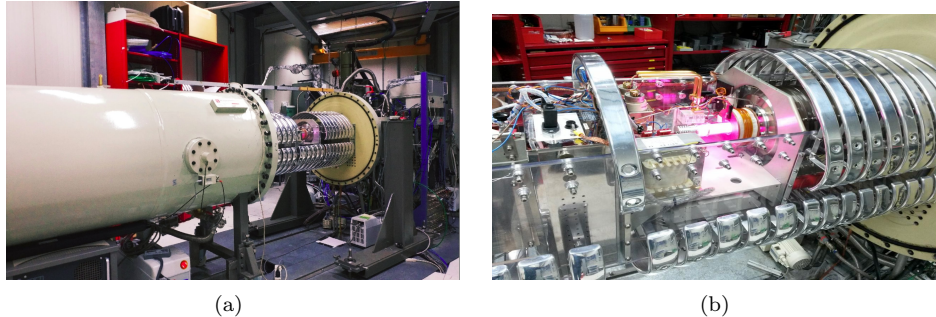


Figure 20: (a) Open tank of the LUNA 400 kV accelerator. The metallic rings keeping the ion source area free from electric fields are visible. (b) Radio frequency ion source. The hydrogen plasma is recognizable by the glowing pink light.

The ion beam can be delivered to a solid target or to a windowless gas target using a vertical steering magnet and respectively a 0° or 45° analyzing magnet. The beam can be properly focused onto the gas target line by minimizing the current on three water cooled collimators of decreasing diameter. The accelerator can work in optimal condition at energies between 50 and 400 kV. The focusing at lower energies in the range, where the intensities are also lower, can be improved using a manual shorting rod to short-circuit some of the accelerator column ring, reducing the number of active elements. A pumping system keeps the vacuum inside the accelerator tube at about 10^{-7} mbar (see section 5.2).

In Figure 21 a top view from LUNA experimental hall of the accelerator and of the two beamlines are shown. All the accelerator parameters can be set and monitored through the HVEE software from LUNA control room. The actual beam energy is a function of the accelerator terminal voltage (TV) and the ion source probe voltage (PV). The energy calibration of the machine over a wide energy range has been done working on solid target line using the well-known radiative capture reaction $^{12}C(p, \gamma)^{13}N$ and resonances in $^{23}Na(p, \gamma)^{24}Mg$, $^{25}Mg(p, \gamma)^{26}Al$ and $^{26}Mg(p, \gamma)^{27}Al$ reactions, particularly useful to get energy spread and beam stability over long run time [48]. To check the calibration validity also on the gas line, known resonances in $^{20}Ne(p, \gamma)^{21}Na$ and $^{21}Ne(p, \gamma)^{22}Na$ have also been analyzed.

The energy calibration function obtained is given by:

$$E = (0.9933 \pm 0.0002) \frac{keV}{kV} \cdot (TV + PV) - (0.41 \pm 0.05) keV \quad (18)$$

Proton beam energy is found to be calibrated with 0.3 keV accuracy, allowing precise determination of the energy in the center of mass of the nuclei interacting during each experiment.

5.2 Windowless gas target

The choice of a gas target during a nuclear astrophysics experiment has a number of advantages. First of all, since measurements are very long in order to improve counting statistics, the target need

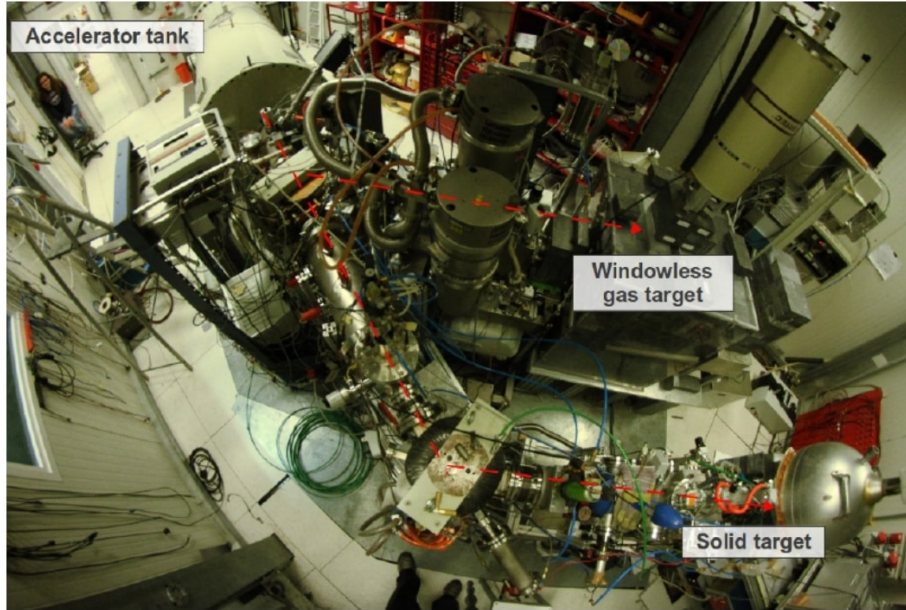


Figure 21: Wide angle view of the LUNA experimental hall. The solid and gas target beam lines are indicated.

to be stable under intense beam bombardment. Gases are good candidates in this sense, because their deterioration can be contained continuously injecting new gas in the chamber. Moreover, gases can achieve high degree of isotopic purity, limiting the amount of contaminants which can produce unwanted background during measurements. Finally, using a windowless gas target, without any entrance foil separating the beam from the gas chamber, has the great advantage of limiting beam energy loss and energy straggling. These effects arise from the particle-particle interactions as projectiles proceed along the beam line. Each interaction transfers a little amount of energy from the beam to the target nuclei, but having many particles in the beam enhances the effect (energy loss). In addition, since the nature of the interaction is stochastic, the amount of transferred energy varies from particle to particle, introducing a variation of the shape of the projectile energy distribution (energy straggling). Further information on this effects related to the reaction of interest in this study will be given in the followings.

Of course, using gaseous targets also add some complication, because measuring nuclear cross-sections with them requires a precise knowledge of the gas density and detection efficiency along the whole beam path.

A scheme of LUNA windowless gas target is reported in Figure 22

The system consists of three differential pumping stages, the interaction chamber (see Figure 23), a gas distribution line and a gas recycling system.

The beam from the accelerator is collimated through three water-cooled apertures of decreasing diameters (AP3, AP2, AP1). Each of these apertures is provided with an ammeter in order to check the current loss during the beam focusing. They also work as increased impedance for the gas flow from the target chamber back to the accelerator.

The target chamber is filled of gas through an inlet copper tube located at the end of the chamber

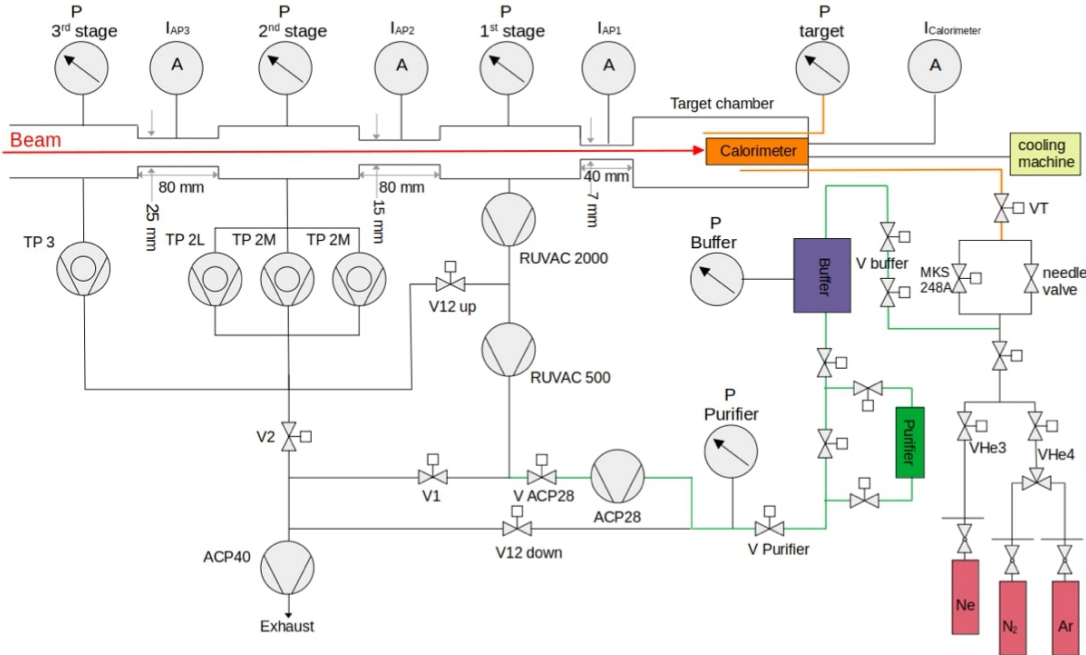


Figure 22: Sketch of the gas target components, including differential pumping system. The red arrow represents the beam line from the accelerator.

flange when the VT valve is open. The gas can come from a bottle located outside (VHe4 valve open) or inside (VHe3 valve open) the experimental room. The second line is used for more expensive gases, such as the enriched ones, since the line itself is shorter and possible losses are therefore reduced. The injection of gas is actually split in two branches: one with a needle valve providing a constant influx, the other equipped with a feedback-controlled valve (model MKS 248A) that adjusts the gas flow to keep a constant pressure inside the target.

The gas flowing out from the chamber through the AP1 collimator is continuously pumped thanks to the three pumping stages, preserving vacuum inside the accelerator tube. The first pumping stage, closer to the chamber, is equipped with a RUVAC WS 2001 (pumping capacity $2050 \text{ m}^3/\text{h}$) pump-backed by a RUVAC WS 501 ($505 \text{ m}^3/\text{h}$) pump. Here, 99.5% of the gas is pumped out, achieving pressures of about $6 \cdot 10^{-3}$ mbar¹². The remaining gas then reaches the second stage by crossing the longer AP2 collimator, where three TMP1000C ($3600 \text{ m}^3/\text{h}$) turbopumps (TP2L, TP2M, TP2R) work to achieve $\sim 10^{-6}$ mbar pressure. In the last stage, the residual gas is pumped out by a TURBOVAC 361 ($1250 \text{ m}^3/\text{h}$) turbopump, achieving $\sim 10^{-7}$ mbar pressure.

The gas from the first two pumping stages can either be flushed out and wasted or collected and purified to be re-used. This second approach is crucial when dealing with expensive enriched or rare gases: an ACP28 pump collects the discards and send them to a Monotorr PS4-MT3-R-2 purifier with a chemical getter, designed to remove hydrocarbons, oxygen and nitrogen from noble gases. The cleaned gas is then stored in a buffer volume until being re-injected in the system, adjusting properly the valves.

The gas target is controlled by LabVIEW software and an NI FieldPoint based system. They allow to operate the gas from remote and monitor the status of the pumps and valves. Moreover, the

¹²Reference values for a neon target gas pressure of 2 mbar.

software also log every 1 second the pressures in the different pumping stages, in the target chamber, the purifier and the buffer, allowing a detailed knowledge of the gas behaviour during measurements.

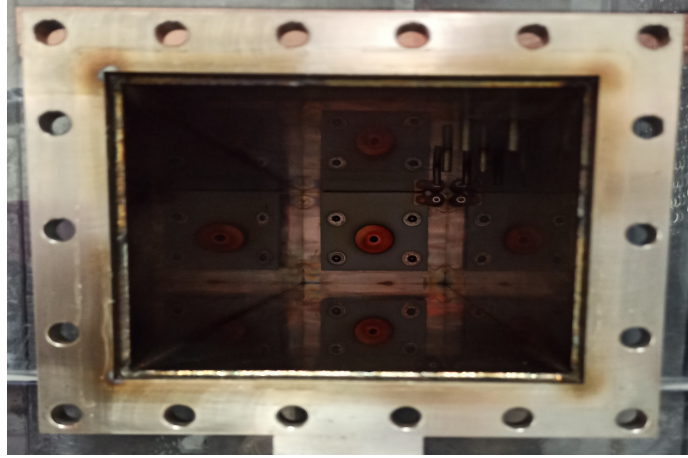


Figure 23: View of the target chamber from the calorimeter side. The AP1 copper collimator is visible.

5.3 Calorimeter

After entering the target chamber, the ion beam reacts with the target nuclei and is stopped on a copper calorimeter mounted on the chamber end flange. The interaction with the gas and the beam stop surface produces many secondary electrons and many low-energy protons can be neutralized as well. The classical approach for electrically reading beam currents with a Faraday cup cannot therefore be applied in such a setup. Instead, the current intensity is measured using the calorimeter with a constant temperature gradient applied on its sides [48].

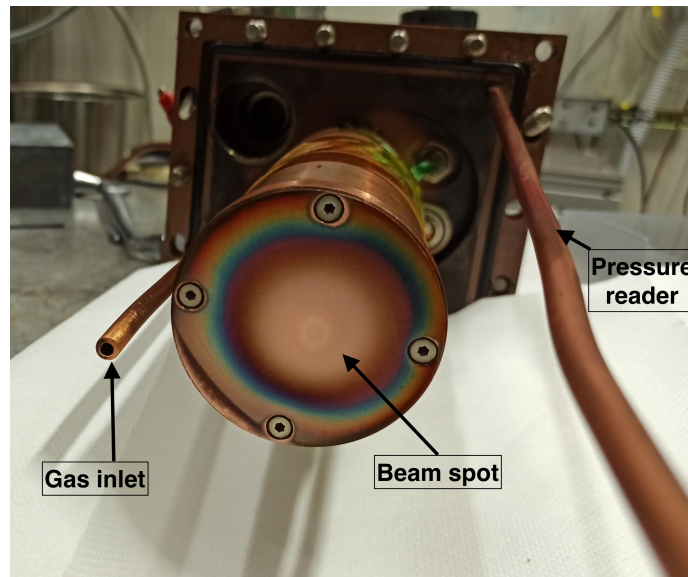


Figure 24: Picture of the calorimeter taken after the $^{20}\text{Ne}(p,\gamma)^{21}\text{Na}$ campaign. The spot produced by the impinging proton beam can be seen. Inlet tubes for gas injection with constant flux or with feedback pressure reading are also indicated.

The calorimeter (Figure 24) is composed of a hot side and a cold side in thermal contact with each other. The hot side is measured and kept at a constant temperature of 70°C by a set of five PT100 thermoresistors driven by electrical current and an active feedback control system, while the cold side is kept at -5°C by an insulating cooling liquid. The feedback system works adjusting resistors' current to compensate possible fluctuations in the beam current which can lead to different heat amount provided by the beam itself to the hot side. A picture from outside the chamber of the inserted end flange holding the calorimeter is shown in Figure 25. The tubes connected to the refrigerating system are also visible, as well as the pressure and power readers.

In Figure 26 a schematic representation of the calorimeter functioning is reported. In the absence of



Figure 25: Picture of the target chamber's rear side, where the calorimeter is inserted. The black tubes are connected to the refrigerating system that keeps the cold calorimeter side at the desired temperature.

the beam, the power provided by the resistors (zero power W_0) is recorded over 10 minutes period before and after each beam time. When the active measurement is ongoing, the beam hits the calorimeter hot side, providing a certain amount of heat that contributes to keep the temperature at 70°C. As a consequence, the power W supplied by the resistors during beam run decreases with respect to W_0 .

The beam current can be derived from those power readings following

$$I_{beam} = \frac{W_0 - W}{E_p - \Delta E} \quad (19)$$

where E_p is the proton beam energy at the entrance of the target chamber and ΔE is the total beam energy loss from the target chamber entrance to the calorimeter. Once the current is known, from the total time of the measurement is possible to obtain the charge deposited by simply multiplying it to the current value.

The output calorimetric power is measured by a NI cRIO 9207 module and logged every two second by a LabVIEW control software. The software, as well as monitoring all parameters (temperatures,

resistors current and voltage from where power is derived), is able to stop the beam from reaching the target if the temperature read is too high, preventing calorimeter overheating. More detail can be found in [49]. In Eq. 19, the numerator $W_{calo} = W_0 - W$ should actually be replaced by the

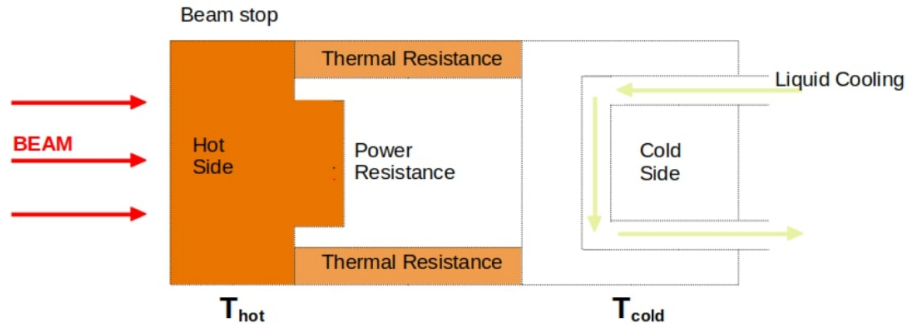


Figure 26: A schematic draw of the beam calorimeter.

correct electric power $W_{el} = m \cdot W_{calo} + q$. The numeric parameters m and q are found with a calorimeter calibration procedure during which the chamber is evacuated from all the gas and used as a Faraday cup to measure beam currents. This usually gives a relation close to 1 to 1. The calibration adopted for $^{20}Ne(p, \gamma)^{21}Na$ will be better explained in Section 6.2.

5.4 Background

Background of a gamma spectrum can be divided into two main components: **natural background**, always present with variable magnitude, and **beam-induced background**, which is strictly connected to having energetic beam particles interacting with others. Their contribution depends on many variables, among which the location of the setup, the type and size of the detector used, the shielding adopted, the purity of the target and the energy of the beam.

5.4.1 Natural background

Natural background is a source of noise that is due to the environment in which we perform our experiments. It can be further divided into a component at energies above approximately 3 MeV and one below this threshold.

The main advantage of going underground is a significant reduction of the high-energy component, which is due to gamma photons arising from cosmic rays and cosmic neutrons interaction with matter. Among these sources, neutrons and muons are the most problematic ones, causing background either interacting directly with various components of the setup or producing other troublesome energetic particles. At LUNA, thanks to its 1400 meters of rock shielding, muon and neutron fluxes are reduced by a factor 10^6 and 10^3 respectively, significantly improving the signal to noise ratio above 3 MeV ([50], [51]).

The low-energy component is instead connected to the gammas produced by the decay chains of radioactive isotopes naturally embedded in rocks. Major radioisotopes at LNGS are ^{232}Th , ^{238}U and ^{40}K . To protect the setup from this contamination source, passive shielding made of high Z elements such as copper or low-activity lead are used. At LUNA, it is possible to use thicker shielding layers with respect to a surface facility, thanks to the lower cosmic ray flux producing less spurious counts when interacting with the shield.

As a result, the overall natural background is reduced significantly over a wide energy range. This is clearly seen in Figure 27, where it is shown a comparison of a typical gamma spectrum on surface and in underground, with and without shielding.

As a final note, natural radioactivity of detectors themselves has also to be considered and detectors should be manufactured as purer as possible in order to limit this unwanted effect.

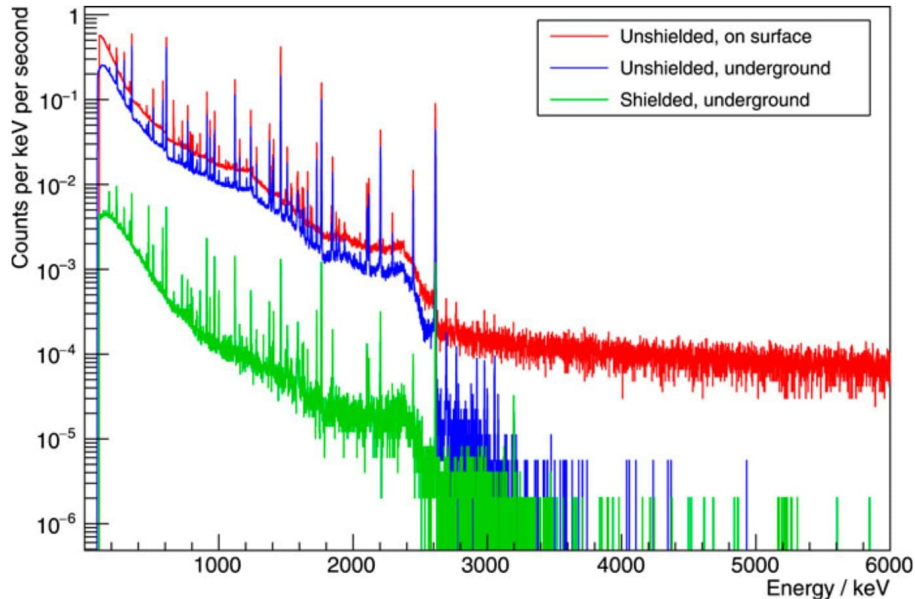


Figure 27: Typical γ -ray background taken at LNGS with a HPGe detector in the surface laboratory (red), at LUNA experimental underground hall (blue) and at LUNA with 15 cm lead shielding (green).

5.4.2 Beam-induced background

When the beam enters the target chamber, it will interact not only with the nuclei relevant for the reaction under study, but possibly with other kind of nuclei. These can be deposited on the surfaces of the chamber, of the collimator and of the calorimeter, or also present in the target itself¹³. This kind of background is highly dependent on the beam energy and on the location of the contaminants along the beam path, which is usually difficult to determine exactly.

As a general rules, because of the increasing Coulomb barrier for increasing charge number Z , only contaminants having $Z < Z_{target}$ can spoil significantly the spectra from the reaction. If the energy of the transitions associated with beam-contaminants reaction falls in the same energy region of the studied nuclear reaction, those contaminants can significantly limit the signal from relevant transitions. Moreover, even when this is not the case, the *Compton background*¹⁴ from other peaks can still increase the overall background. Additionally, when the gamma energy exceed the rest-mass of a electron-positron system ($E_\gamma > 1022$ keV), pair production process may occur. This produces the so called *single and double escape peaks* in the spectrum, located respectively at 511 and 1022 keV left with respect to the initial (or full) energy peak.

¹³This is a major problem for solid targets, both because they are less pure and because they can be built using compounds of the target nuclei.

¹⁴A photon which loses some of its initial energy through Compton scattering in the detector material before being fully detected, will produce a signal in the spectrum at energies lower than its initial one, over a quite wide energy range that depends on the scattering angle.

Typical beam-induced background at LUNA is due to boron, carbon, nitrogen, boron and fluorine. In particular, when using a proton beam, the following reactions can be initiated:

- $^{11}\text{B}(p, \gamma)^{12}\text{C}$ ($Q_{value}=15957$ keV): this reaction plays a significant role when running the accelerator at energies close to the resonance at $E_{lab}=163$ keV. A peculiar observed peak is at $E=4439$ keV coming from the ^{12}C level de-excitement.
- $^{12}\text{C}(p, \gamma)^{13}\text{N}$ ($Q_{value}=1943$ keV): the reaction produces photons with energies $E=Q_{value} + E_{cm}$. Carbon could be originated from the hydrocarbons in the pumping system oils and then easily adsorbed onto metallic surfaces. We could have traces of it both on the collimator and on the calorimeter: in this case two gamma rays may be visible, depending on the position of the carbon along the beam path, where different E_{cm} are achieved.
- $^{13}\text{C}(p, \gamma)^{14}\text{N}$ ($Q_{value}=7551$ keV)
- $^{14}\text{N}(p, \gamma)^{15}\text{O}$ ($Q_{value}=7297$ keV): various peaks from this reaction can be seen in the spectrum, connected to the many possible gamma cascades through which the ^{15}O nucleus can de-excite. A particularly problematic beam energy is $E_{lab}=273$ keV, for which a resonance is onset. The nitrogen might be brought into the setup from air entering through leaks or being implanted in the surfaces during different test with nitrogen gas.
- $^{15}\text{N}(p, \alpha\gamma)^{12}\text{C}$ ($Q_{value}=4965$ keV) and $^{15}\text{N}(p, \gamma)^{16}\text{O}$ ($Q_{value} = 12126$ keV)
- $^{19}\text{F}(p, \alpha\gamma)^{16}\text{O}$ ($Q_{value}=8114$ keV): the reaction produces major background contribution when the beam has energies matching two resonances at $E_{lab} = 223$ and 340 keV. A complex structure showing full energy peak at $E=6130$ keV (^{16}O level de-excitement to the ground state) together with single and double escape ones, with traces of Doppler effect increasing their widths. The fluorine is an ingredient in the heat-conducting paste of the calorimeter and of Viton O-rings used in various part of the setup.

In Section 9.1 the major contamination sources encountered during $^{20}\text{Ne}(p, \gamma)^{21}\text{Na}$ reaction study campaign will be presented, also showing the associated transitions appearing in the acquired spectra.

6 Experimental setup for $^{20}\text{Ne}(p, \gamma)^{21}\text{Na}$ reaction study

The setup used at LUNA for studying $^{20}\text{Ne}(p, \gamma)^{21}\text{Na}$ reaction is reported in Figure 28. The same setup was used to study both the resonance at $E_{cm} = 366$ keV (2020-2021 campaigns, see [42]) and the direct capture component (2022 campaign reported in this thesis).

LUNA 400 kV accelerator delivered its intense proton beam on the windowless gas target, filled with natural neon (^{20}Ne isotopic abundance $(90.48 \pm 2.01)\%$) at a constant pressure of the order of few mbar (depending on the beam energy used).

The detection system consists of two high-purity germanium detectors: an Ortec low background detector with 90% relative efficiency (shown here also as GeDD) and a Canberra low background detector with 130% relative efficiency (shown here also as GePD).

Germanium detectors are widely used for gamma spectroscopy because of their good energy resolution and the possibility of using them as total absorption detectors thanks to their large active thickness. Moreover, their high Z increases the probability of gamma-ray interaction. The energy resolution is improved by the low average energy necessary to create an electron-hole pair in the

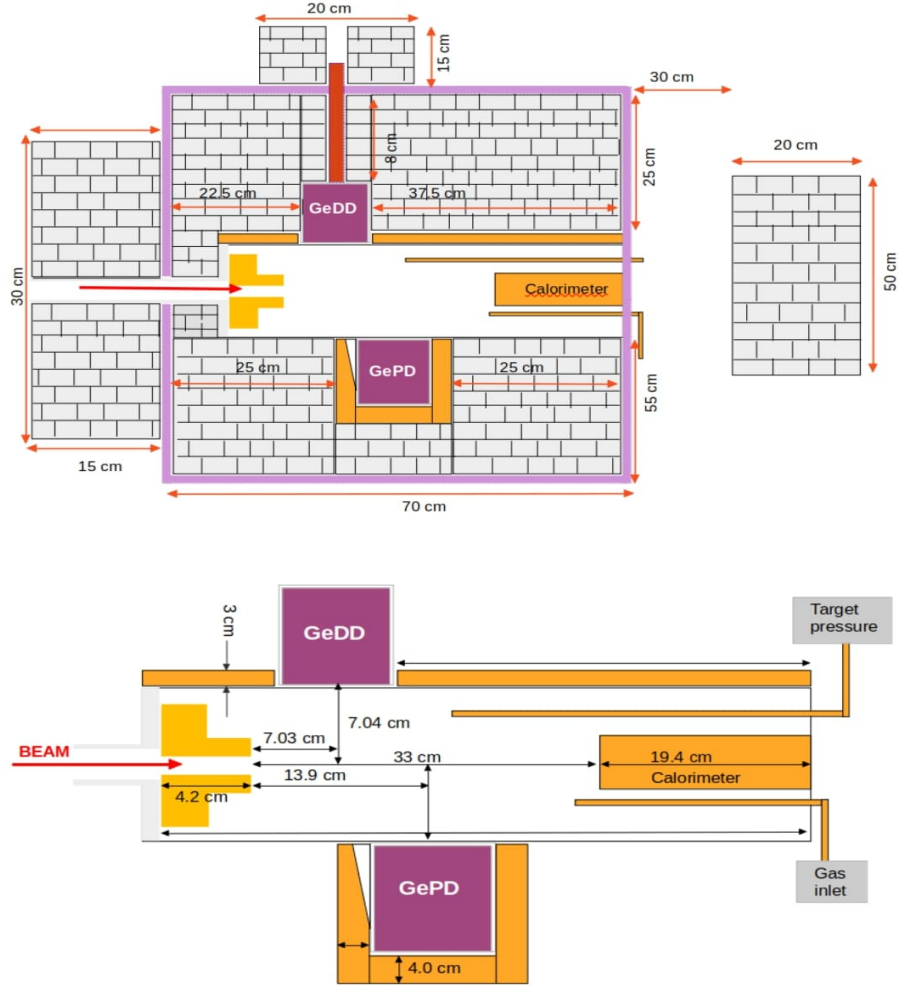


Figure 28: Drawing of the experimental setup used for the $^{20}\text{Ne}(p,\gamma)^{21}\text{Na}$ reaction. The lead bricks (gray) and copper shielding (yellowish) used are shown. The anti-radon box is shown in violet.

semiconductor depletion zone (2.9 eV versus the 3.6 eV required by silicon detectors), therefore producing the electric signal converted into photon counts in the acquired spectrum. Of course, this fact also introduces a drawback: the germanium crystals need to be constantly refrigerated at very low temperatures (77 K), to avoid room temperature causing thermal excitation and production of spurious counts [52]. At LUNA, the two detectors are refrigerated with liquid nitrogen (LN_2).

The GePD detector, which is also the largest one, is located below the target chamber at 13.9 cm from AP1 collimator and is surrounded by a 4 cm thick copper shielding plus a 25 cm thick lead shielding. The copper shielding is effective in reducing the bremsstrahlung γ -rays produced in the lead shielding by the electrons emitted in the β -decay of ^{210}Bi (daughter of radioactive ^{210}Pb , which can be found in the shielding). The GeDD detector is instead located on top of the target chamber at 7.03 cm from AP1 collimator and is surrounded only by the lead shielding.

Between the lead shielding above the chamber and the chamber itself, a 3 cm thick copper shielding is also used. Furthermore, a lead shielding was also built behind the chamber end flange, to shield properly GePD detector from background photons entering the chamber through the calorimeter side. For the same reason, photons coming from the AP2 collimator after beam interaction are

stopped by 15 cm thick lead shielding between the first pumping stage and the chamber (see Figure 28).

The main lead castle, which was visible also in Figure 21, is enclosed in a plexiglass anti-radon box, depicted by the violet line in the upper part of Figure 28. The box establishes a nitrogen over-pressure around the lead castle which prevents radon gas from flushing inside the setup.

6.1 Campaign details

This thesis is focused on the analysis of the spectra acquired during LUNA campaign devoted to the direct capture component of the $^{20}\text{Ne}(p, \gamma)^{21}\text{Na}$ reaction. The measurements have been performed at LNGS along four weeks between March and April 2022.

The data acquisition system providing the spectra I have analyzed is an analogue multichannel one. The signals of the two detectors go to the preamplifiers. Thereafter, the amplified signals are sent to two active splitters (multiple distribution modules) and split in order to link them to each other and to different signal processors. One of the two split signals is then sent to an ORTEC Spectroscopy Amplifier (671 for GePD and 672 for GeDD). Those signals are finally sent to an EtherNIM analog multichannel analyzer (4 channels) and read by Maestro software. This approach allowed an offline preliminary analysis from the control room, because the Maestro software also provides directly the acquired spectra, which can be monitor at all time and automatically saved every hour. The other split signal is sent to CAEN N6724 digitizer module. This is a different data acquisition system that allows the storage of the single events recorded by the two detectors in list mode configuration, saving time, energy and pile-up of each registered event. The resulting spectra were not analyzed for the present campaign.

During the available beam time at LUNA 400 keV, ten long runs (1-2 days long) have been performed. In Table 8 beam energy, target pressure and GePD detector live time¹⁵ are reported. The pressure of the $E_{beam} = 400$ keV run is reduced with respect to other runs in order to avoid exciting the $E = 384$ keV resonance and focus the analysis only on the direct capture. As it will be shown, the beam interaction with the neon gas at 2 mbar leads to an energy loss within the target of approximately 22 keV. Therefore, considering an initial energy of 400 keV, it is possible to have proton beam at 384 keV at some point along the beam path, populating there the resonant state. Instead, working at a lower pressure of 0.5 mbar, the energy loss amounts to just 5 keV and the resonance is not excited.

6.2 Calorimeter calibration

As previously introduced, the calorimeter can be used to measure beam currents once it has been calibrated. The calibration adopted in this analysis has been performed in October 2020 for the 366 keV resonance study. The procedure consists in evacuating the target chamber (reaching 10^{-5} mbar) and using the calorimeter connected to the target chamber as a Faraday cup, with both elements electrically insulated during the whole process. The beam currents were stable and intense, more than $450 \mu\text{A}$, and the calorimeter sides were kept at 80°C and -15°C to guarantee proper functioning under intense currents. Several runs have been performed varying the proton energy from 50 keV to 390 keV, using a current integrator to get I_{target} and a counter unit to collect the total charge q

¹⁵Live time is the actual time during which the detector was able to record photons. Real time of the measurement is longer and does not consider the detector dead time, which is the time after a recorded event during which the system is not able to record another one.

Beam energy (LAB) (keV)	Pressure (mbar)	Live time (s)
400.1	0.5	151603
380.4	2	80884
329.7	2	76402
329.7	2	80339
319.0	2	75350
309.7	2	81558
299.4	2	82657
299.2	2	80844
259.7	2	75558
259.7	2	82867

Table 8: Beam energies explored during $^{20}\text{Ne}(p,\gamma)^{21}\text{Na}$ campaign on direct capture at LUNA. Pressure and live time of the different runs are also shown.

reaching the calorimeter.

For each run the calorimetric electric power is calculated as:

$$W_{el} = \frac{E_{beam}I_{target}}{q} \quad (20)$$

while the power read by the calorimeter as previously explained as

$$W_{cal} = W_0 - W_{beam} \quad (21)$$

It is then possible to fit W_{el} as function of W_{cal} using a straight line $W_{el} = mW_{cal} + q$. The fit of the obtained data are given in Figure 29, together with the fit parameters m (slope) and q (offset). Fit residuals are also shown and are less than 1%. In the plot, October 2020 data points, giving calibration adopted in the present analysis, are given in blue. Red points are instead referring to a previous calibration (February 2020), where the achieved beam currents were lower and the setup for the calibration still not completed.

7 Target characterization

When dealing with a gaseous target it is crucial to characterize precisely its density, since the beam energy loss coming from beam collisions with matter is linked to its value $\rho(z)$ along the beam path. This density profile is connected to variation in pressure $p(z)$ and temperature $T(z)$. While pressure is kept at a constant level inside the chamber thanks to the feedback system, a temperature gradient is established because of the presence of the calorimeter hot side and of the water cooled collimator. Once $p(z)$ and $T(z)$ are known, it is possible to obtain the density profile from the ideal gas equation of state according to

$$\rho(z) = \frac{p(z)}{k_b T(z)} \quad (22)$$

where the density is given in $\frac{\text{at}}{\text{m}^3}$, the pressure in Pa and the temperature in K. The differential energy loss along a certain path dz , the so-called *stopping power*, is given by the Bethe-Bloch formula. A charged particle travelling in matter loses energy depending on many properties, such as the projectile charge and velocity (the less-charged and faster it is, the lower the interaction probability) and the target atomic number and density (the higher they are, the more stopped is

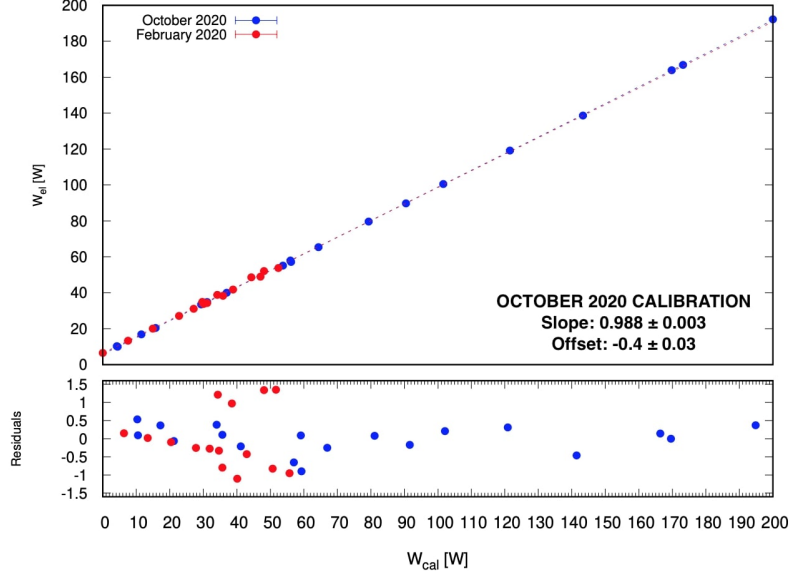


Figure 29: Comparison of two different calorimeter calibrations: February 2020 and October 2020. Calorimeter calibration function (top) and relative residuals (bottom). The error bars are smaller than the point dimension. October 2020 calibration parameters, which have been used in the present analysis, are also written.

the projectile). The stopping power $\frac{dE}{dz}$ or $\frac{dE}{d(\rho z)}$ is usually tabulated taking into account experimental data and theoretical simulations based on the Bethe-Bloch formula. In the end, the energy loss along a finite path can be evaluated as the integral

$$\Delta E = \int_{z_{in}}^{z_{fin}} \frac{dE(z)}{d(\rho z)} \rho dz \quad (23)$$

where $\frac{dE}{d(\rho z)}$ represents the stopping power for proton in ^{20}Ne gas in units of $\frac{eV}{atoms/cm^2}$, ρ is the density in $\frac{atoms}{cm^3}$ and z the position along the beam path given in cm . For the present analysis, the stopping power has been taken from SRIM [53], where it is tabulated with an uncertainty of 1.7%. In Figure 30 the stopping power as function of proton projectile energy tabulated in SRIM database is reported.

The integral calculation has been implemented from an initial z_{in} located in the tube connecting the first pumping stage and the chamber. Then, at each integral step, the amount of energy lost per unit path length is re-evaluated taking into account the precise energy at the beginning of the step. This allows to take into account the non-linearity of the stopping power: for the energy range explored in the present campaign, as the beam proceeds the loss effect is enhanced because of the reduction in beam energy.

In Figure 31 the energies as function of the position along beam path for some of the energy explored during LUNA measurements are shown. The coordinate z follows the beam path and its origin is located in the tube connecting the first stage to the chamber. Even if the density of the gas in the tube is considerably lower than in the chamber, it has been found sufficient to produce a $\Delta E \simeq 0.6$ keV before the collimator. This energy loss can modify the measured strongly energy-dependent cross-section values and has therefore to be taken into account. The proton beam loses energy inside

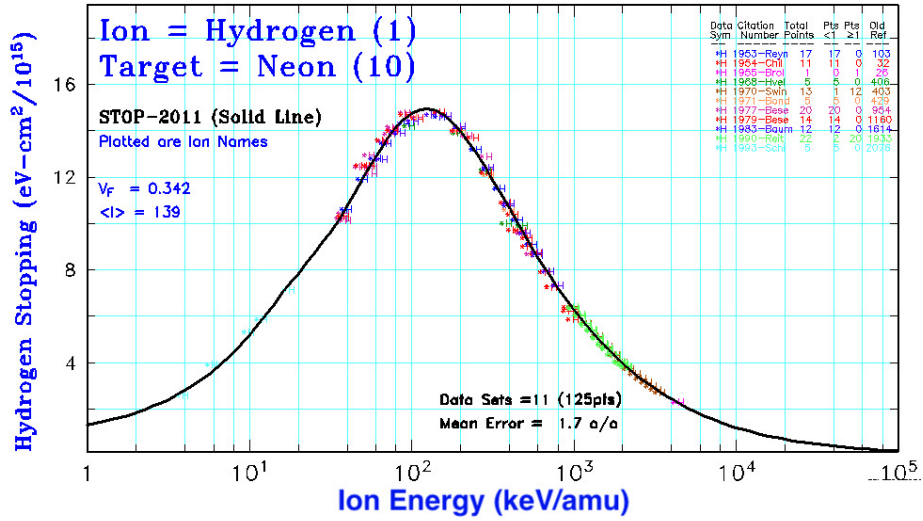


Figure 30: The graph presents the SRIM stopping power calculation for hydrogen in neon gas as function of the energy, together with 124 experimental data points taken from 11 different papers shown in the legend. Graph from SRIM database [54]

the neon gas depending on its initial energy: the higher is the energy, the weaker is the effect. At different points inside the chamber, the $^{20}\text{Ne} + p$ reaction will therefore occur at different energies in the center of mass and also the energy deposited on the calorimeter will not be the same as the initial one.

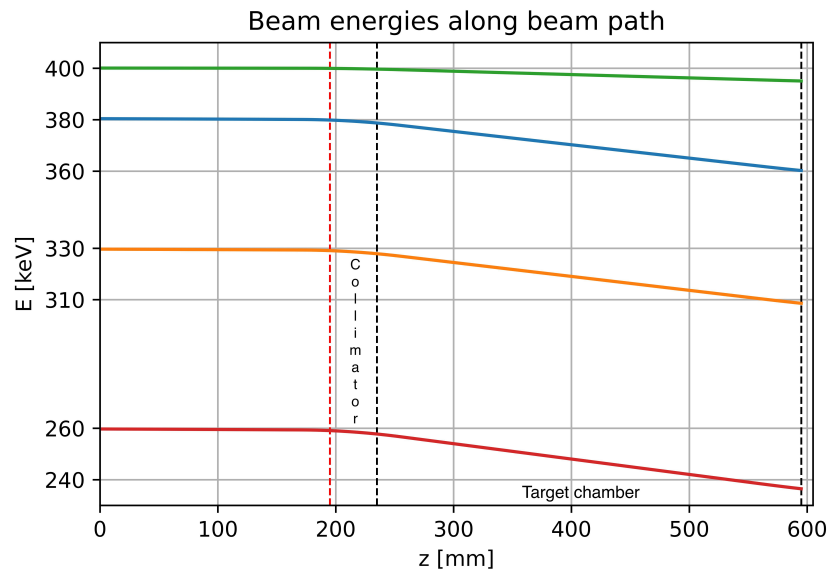


Figure 31: Some of the beam energies ($E_{beam} = 260, 330, 380, 400$ keV) explored during the present campaign as function of position along the beam path. The energy loss effect is clearly visible: the energy of the beam decreases as coordinate z increases. At $E_{beam} = 400$ keV, the effect is reduced because of the lower pressure (therefore density) at which the run has been performed.

7.1 Gas density without beam

Pressure and temperature are independent on the particular neon isotope considered. For the present analysis gas density profile in the chamber without proton beam has been obtained starting from pressure and temperature values measured during $^{22}\text{Ne}(p, \gamma)^{23}\text{Na}$ measurement campaign [55]. For the purpose, a mock chamber with the same geometry as the one used for the reaction study was used. The chamber was equipped with several flanges through which temperature and pressure gauges could be inserted (see Figure 32). The gas pressure has been measured with three capacitance

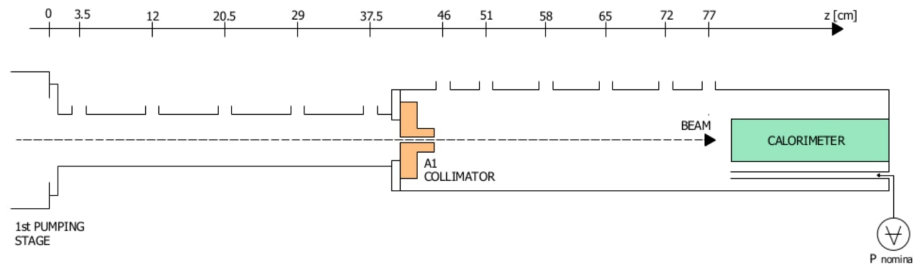


Figure 32: Schematic view of the target chamber used for the pressure and temperature profiles measurement. The position of each flange is reported on the top axis. Precise values were obtained from the gauge at $z=20.5$ cm up to the last gauge at $z=77$ cm, right before the calorimeter.

manometers: two Pfeiffer manometers with 0.20% accuracy and one MKS manometer with 0.25% accuracy. Another MKS manometer with 0.25% accuracy was connected to the end flange of the chamber and used as a reference for the feedback system, keeping the pressure at constant selected value. One manometer was always mounted on the $z = 65$ cm flange, while the other two were moved from run to run in order to cover all possible positions shown in Figure 32. In Figure 33 the pressure profiles interpolated from the experimental points taken at the relevant target pressures of $p=0.5$ and 2 mbar are shown. The pressure raises within the collimator and is constant between it and the calorimeter.

As for the temperature profile, it has been measured with four resistance temperature detectors PT100 with an accuracy of 0.3 K. Further uncertainty of 1 K comes from temperature variation when modifying the gauge's orientation, while differences observed from repeated measurements in same conditions adds other 0.5 K of uncertainty. The interpolated temperature profile at $p=0.5$ and 2 mbar target pressures are reported in Figure 33. As expected, the gas temperature increases monotonically from the water cooled collimator to the hot calorimeter side, where the temperature is kept at 343 K.

By combining all the uncertainties, the density profile obtained following the ideal gas formula is evaluated with 1.1% of systematic uncertainty [12] (see Figure 34).

7.2 Beam heating effect

The density profile derived as described in the previous section does not take into account the effect of the proton beam during measurements, also known as *beam heating effect*. The interaction of the beam with the gas leads to an increase of its temperature and, consequently, to a decrease in the overall gas density profile.

This effect has been widely studied in different gases ([56],[57]). Beam heating characterization in neon gas has been performed at LUNA during the $^{22}\text{Ne}(p, \gamma)^{23}\text{Na}$ campaign ([14],[12]), using the

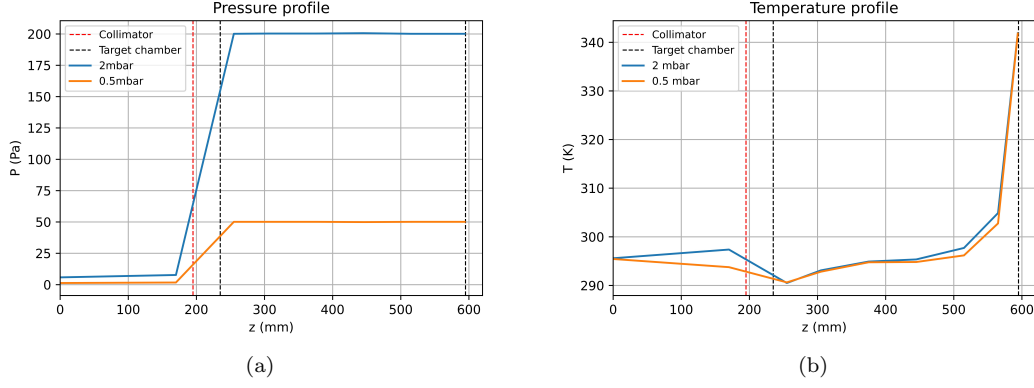


Figure 33: (a) Pressure and (b) temperature profiles interpolated from measured values along the beam path. The profiles reported are referring to a target pressure of 2 mbar (blue line) and 0.5 mbar (orange line).

resonance scan technique. This technique exploits the dependence of energy loss on the gas density: following Eq. 23, since beam heating affects only the density term appearing in it, we can write the density reduction factor as the ratio

$$\frac{\rho}{\rho_0} = \frac{\Delta E^{exp}}{\Delta E_0^{exp}} \quad (24)$$

where the subscript 0 represents the numerical density and energy loss measured without the beam. The energy loss can be evaluated precisely from the study of a well-known resonance, such as the one at 271.56 keV in the $^{21}\text{Ne}(p, \gamma)^{22}\text{Na}$ reaction ([10], [58]). The measurements were performed using the same target chamber as the actual campaign one, filled with natural neon (90.48% ^{20}Ne , 0.27% ^{21}Ne , 9.25% ^{22}Ne), and a collimated (2" x 2") NaI detector placed perpendicularly to the beam path. Various resonance scans were performed varying beam energy with steps between 0.5 and 2 keV, at different gas pressure and beam intensities. When the position at which the beam has an energy matching the resonant level is in front of the detector (where the detector has the maximum efficiency), the scan shows a maximum in the corresponding resonant yield. This implies that the energy loss between starting beam position and detector position is exactly equal to the difference between the beam energy at the yield maximum and the energy of the resonance:

$$\Delta E = E_{beam,max} - E_{res} \quad (25)$$

As the beam intensity increases, the density decreases and the energy loss is reduced. Once ΔE at different beam intensities is known, it is possible to extrapolate the value of ΔE_0 at $I=0$ (no beam). Previous studies ([56],[59]) have shown that the beam heating effect is proportional to the specific power dissipation of the beam in the target gas:

$$\frac{dW}{dz} = \frac{dE}{d(\rho z)} \rho I \quad (26)$$

where I is the beam current in μA , ρ the numerical density in $\frac{\text{atoms}}{\text{cm}^3}$ and $\frac{dE}{d(\rho z)}$ the stopping power, taken from SRIM.

It is then possible to parameterize the density reduction function $\frac{\rho}{\rho_0}$ as:

$$\frac{\rho}{\rho_0} = 1 - \alpha_{BH} \cdot \frac{dW}{dz} [mW/cm] \quad (27)$$

where $\alpha_{BH} = (0.44 \pm 0.05) \cdot 10^{-3}$ cm/mW is the beam heating coefficient experimentally determined for proton in neon gas [60].

The above formula has been used to find the density reduction function for the beam currents achieved during the $^{20}\text{Ne}(p, \gamma)^{21}\text{Na}$ campaign with an iterative approach. An iterative procedure was required since the density appears also in the right-hand term of the equation, within the expression of the power dissipated. Another complication comes from the fact that to estimate beam current from calorimeter data (see Eq. 19), energy loss and therefore gas density is also required. Starting from initial guessed values for density and current, the ratio between densities at each point along the beam path is calculated, taking into account the stopping power change along the path. Beam current is then re-evaluated starting from the new density profile, and the whole procedure is repeated until reaching the desired convergence. Results for density profiles with and without beam heating effect are shown in Figure 34 for a target pressure of 2 mbar and a beam energy of 330 keV. The uncertainty on the profiles taking into account beam heating effect are between 1.1-1.5%, depending on beam energy.

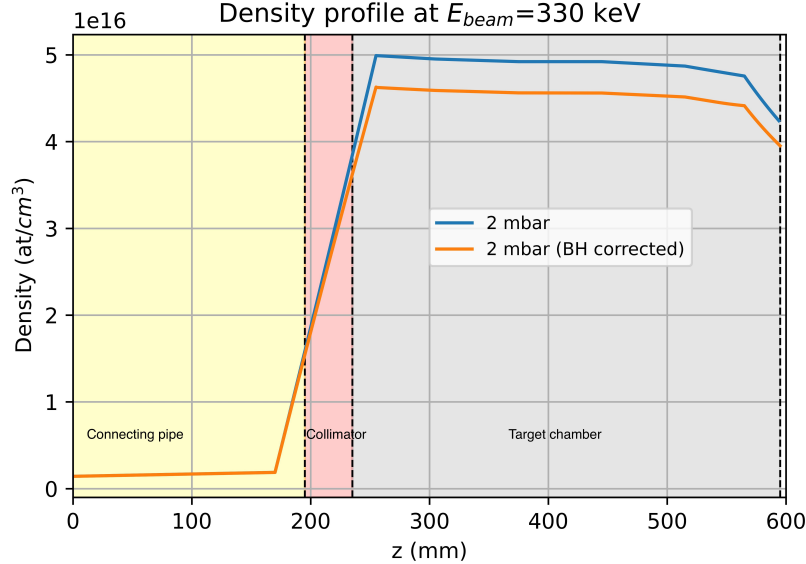


Figure 34: Numerical density profiles at target pressure $p=2$ mbar without (blue) and with (orange) beam-heating effect. As expected, the effect is larger at larger densities in the target chamber.

8 Detection efficiency

In an extended gas target, the interaction of the proton beam with ^{20}Ne target nuclei takes place at different position along the beam line. The emitted gamma rays are consequently seen at different angles from the two detectors: their efficiency η in detecting photons is maximum in front of them and decreases with increasing distance. Moreover, not only the detection efficiency is position-

dependent, but also energy-dependent. Because of the photon cross-section energy dependence, the higher is the energy of emitted photons the lower is the total absorption probability and, consequently, the HPGe photopeak efficiency. For $^{20}\text{Ne}(p, \gamma)^{21}\text{Na}$, the emitted photons have energies up to ≈ 3 MeV: η has therefore to be measured at several positions in the chamber over a wide energy range.

Detection efficiency was accurately determined during previous campaigns on $^{20}\text{Ne}(p, \gamma)^{21}\text{Na}$ 366 keV resonance (see [42]). Since the gas target detection set-up has not been dismantled after the last campaign, it was reasonable to assume that the efficiency was not changed. We decided to start this March 2022 campaign on direct capture by checking that the efficiency has been indeed preserved. To do so, we proceeded in measuring the efficiency at low energies as function of z (position along beam line). The usual approach is to employ three point-like radioactive sources of known activities: ^{60}Co , ^{137}Cs and ^{133}Ba . For each source $\eta(z)$ is measured with steps of 0.5 - 1 cm. The main properties of the sources are summarized in Table 9. For these measurements,

Source	Reference date (t_0)	A_0 (kBq)	$T_{\frac{1}{2}}$ (yr)	E_{gamma} (keV)	Br (%)
^{137}Cs	1/7/16	6.46 ± 0.04	30.08 ± 0.09	661.66	85.10
^{60}Co	1/7/16	9.01 ± 0.04	5.2711 ± 0.004	1173.23	99.85
				1332.49	99.9
^{133}Ba	4/11/19	28.36 ± 0.03	10.55 ± 0.10	276	7.16
				302	18.33
				356	62.05
				383	8.94

Table 9: List of known properties of radioactive sources used for low energy efficiency determination. Activity at a reference time, half-life and the most intense emitted gamma rays are reported. For ^{133}Ba source only the transitions relevant for efficiency measurements have been reported.

dedicated source holders consisting of central PVC frame were designed to hold the sources at the same height as the center of the AP1 collimator. The source holders can be mounted on a long movable flange that closes the chamber on the calorimeter side and allows the positioning of the source at different z along the target chamber. Figure 35 shows the source holder mounted on the flange and the flange with z -ticks 0.5 cm separated, used as reference to select the distance of the source from the collimator.

At each z , HPGe spectra of the sources are acquired. They show peaks at the energies of the known decay radiation, reported in Table 9. The corresponding efficiency are then obtained as the ratio between the measured net area N of the peak and the number of gamma rays emitted at the same energy of the peak in the whole solid angle by the radioactive source:

$$\eta_\gamma = \frac{N}{A(t_{\text{meas}})\Delta t \text{Br}} \quad (28)$$

where A is the activity at the time of the measurement t_{meas} (number of decays per second), Δt is the duration of the measurement in seconds and Br the branching ratio of the considered gamma ray. The activity at t_{meas} can be derived from the reference data given by Table 9 using the decay law:

$$A(t) = A_0 e^{-\frac{t-t_0}{\tau}} \quad (29)$$

with A_0 certified activity at a given t_0 reference time and τ the isotopic mean life time, given by $\frac{T_{1/2}}{\ln(2)}$. In March 2022 campaign this measurement was firstly performed for the ^{137}Cs source, de-



Figure 35: (a) ^{60}Co source mounted on its holder, which is fixed on a graduated movable flange (b), through which the chamber is closed on the calorimeter side during efficiency measurements.

giving the $\eta(z)$ curve for each of the two detectors. The curve was compared to the analogue one acquired in the previous campaign. The result of the comparison is reported in Figure 36. For a better visualization, blue and salmon data points represent the efficiency at the different target positions taken during March 2022 campaign, while the curves are the interpolation of the efficiency at the same positions taken during November 2021 campaign. The discrepancy was less than 2% and for the purpose of this analysis, it is assumed that the detector efficiency has been reasonably stable.

It has to be stressed that, in general, efficiency determination using radioactive sources can be extended only up to the maximum energy of the gamma rays they emit, so not above $E \approx 1333$ keV in our case. To extend the measurement of the detection efficiency to the high energy region, a standard procedure is to use the well-known resonance at $E_p = 278$ keV in $^{14}\text{N}(p, \gamma)^{15}\text{O}$ reaction. Working with a nitrogen gas target pressure of 4 mbar, it is possible to achieve an almost point-like configuration and, by changing beam energy of 1-2 keV steps, the energy loss allows to populate the resonance at different positions in the target. From the reaction yield at the different positions, it is possible to derive the efficiency for the two high energy gamma rays characterizing the resonance ($E_\gamma = 6171$ and 6790 keV). More details on the approach can be found in [42].

MONTECARLO SIMULATION

During the 366 keV resonance campaign, the experimental setup had been implemented in the

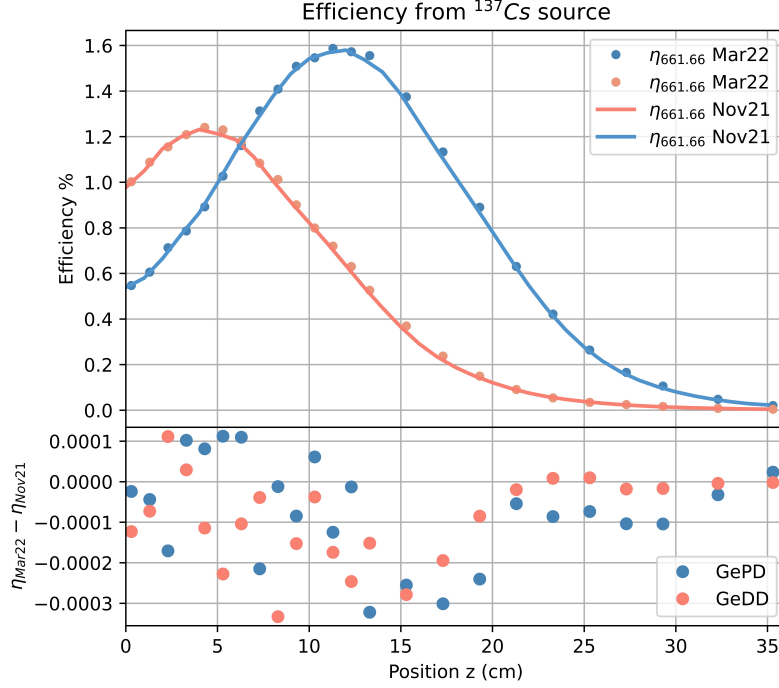


Figure 36: Comparison of detectors efficiency at different position in the target chamber obtained in November 2021 campaign with the same efficiency from the latest March 2022 campaign. Values refer to ^{137}Cs source, emitting photons at 661.66 keV.

Geant 3 simulation written in FORTRAN, in order to complete the detection efficiency and to better define the experimental conditions for $^{20}\text{Ne}(p,\gamma)^{21}\text{Na}$ reaction study ([42]). Geant 3 version was chosen since it already contained various effects due to the beam passing through the target gas, such as the beam energy spread, and had been previously validated in several LUNA experiments ([49],[61],[62]). Moreover $^{20}\text{Ne}(p,\gamma)^{21}\text{Na}$ reaction nuclear case was implemented in the code too. In Figure 37 a side view of Geant 3 geometry of LUNA setup for the reaction study is shown.

Considering that the individual pieces of the setup can be positioned with a slight offset, it is necessary to fine-tune the implemented geometry setup by comparing the performance of the simulation with the experimental data. For this purpose, the efficiency vs position curve and the spectra obtained from the standard ^{60}Co and ^{137}Cs sources as described above were used. The sources have been simulated inside the chamber at fixed positions along the beam line, reproducing the experimental spectra. For each position and for each source gamma the experimental efficiency calculated with Eq. 28 was compared with the simulated one, given by

$$\eta_{sim} = \frac{N_{peak}}{N_{events}} \quad (30)$$

where N_{peak} is the net peak area and N_{events} the total number of simulated events.

In order to achieve the best possible agreement between experiment and simulation, the following parameters appearing in the code can be adjusted:

- Position of the detectors along the beam line
- Detectors' dead layers

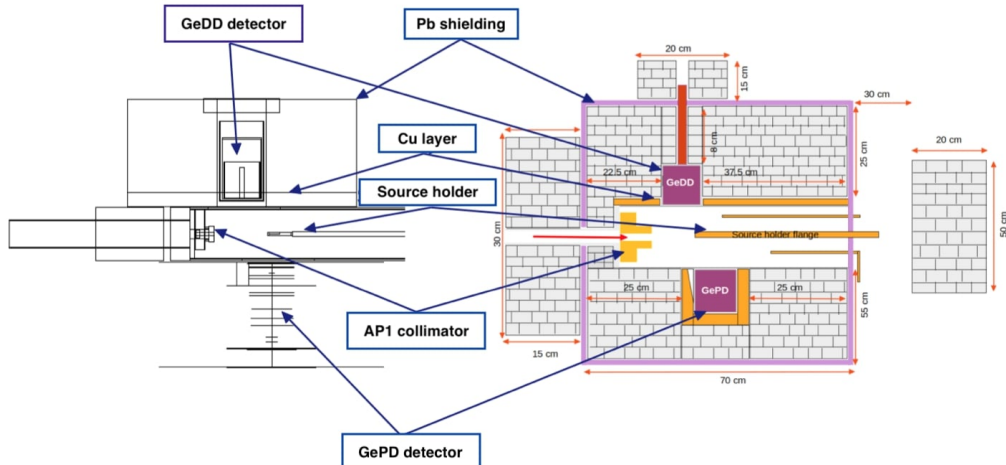


Figure 37: Side view of Geant 3 geometry with matching features to the drawings of experimental setup adopted for $^{20}\text{Ne}(p, \gamma)^{21}\text{Na}$ reaction study.

- Detector distance from the axis of the beam
- Distance of the Pb and Cu shieldings from the detectors and the chamber

The comparison between experimental and simulated efficiency for both detectors is shown in Figure 38. The discrepancies achieved after the fine-tuning are all below 4%. There is a good agreement, except for the positions further away from the detectors, where the efficiency is in any case very low. In Figure 39 the comparison between experimental and simulated GePD spectra for the standard sources is shown.

EFFECTIVE EFFICIENCY

Once the Montecarlo is validated, a realistic simulation of the $^{20}\text{Ne}(p, \gamma)^{21}\text{Na}$ direct capture in LUNA setup can be performed. The energy spectrum was obtained generating a total number of events $N_{events} = 10^8$, weighted along the beam line taking gas density profile and energy cross-section dependence into account. This implies that in the tube connecting the first stage to the chamber the number of reactions will be very low due to the low density, then it will start to increase through the collimator because of more available target nuclei, but, as we proceed along the target chamber, it will start to decrease because of the energy loss that diminish the energy in the center of mass of the interacting nuclei.

In the Montecarlo simulation, the cross-section is usually parameterized for a non resonant process as

$$\sigma(E) = (a + bE + cE^2) \cdot \frac{e^{-2\pi\eta_s(E)}}{E} \quad (31)$$

with η Sommerfeld parameter. In the case of a direct capture, the constancy of the astrophysical S-factor in the considered energy range is implemented in the simulation by putting b and c parameters to 0. As a consequence, the remaining parameter a does not impact the simulation's results, since it does not influence how events are generated along the target chamber. The total number of events is fixed at the beginning and is then distributed among the possible direct capture transitions following the respective branching ratios, which can be found in literature. In particular, direct capture branching ratios from [36] were adopted:

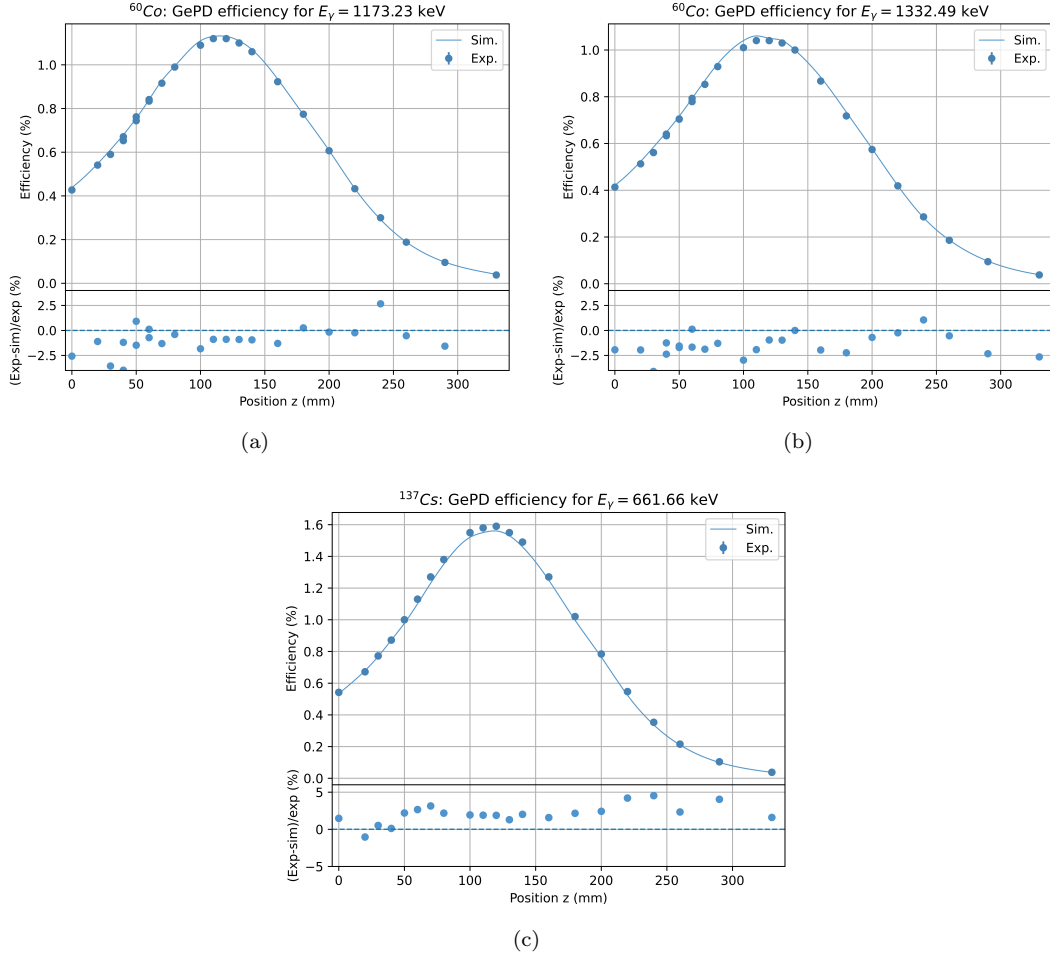


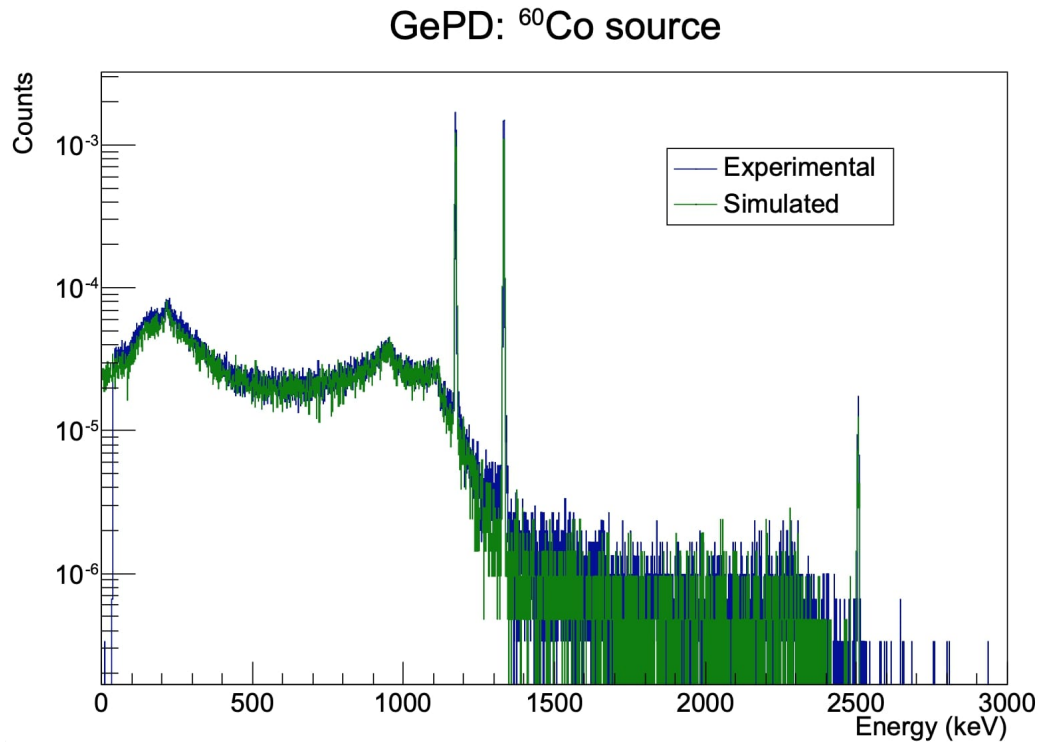
Figure 38: Comparison of experimental efficiency for the standard sources with the fit of the simulated one for GePD detector. The residuals are shown as well. Experimental uncertainties are within the data points.

- $DC \rightarrow 0$ keV: 15.3%
- $DC \rightarrow 332$ keV: 16.1 %
- $DC \rightarrow 2425$ keV: 68.6 %

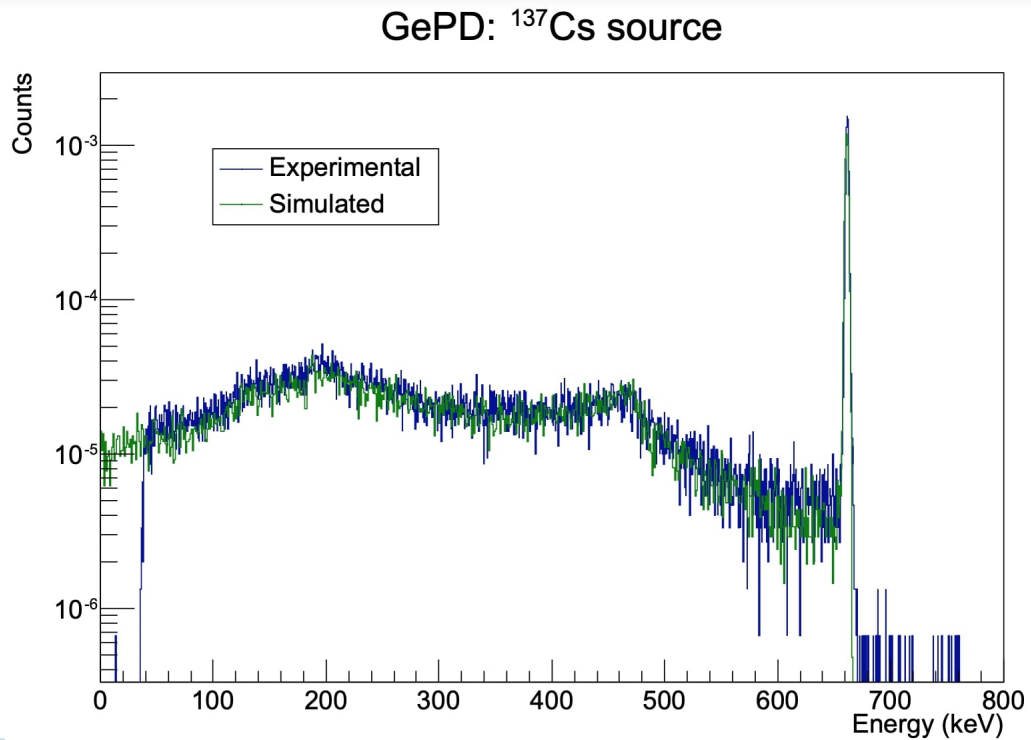
The *effective efficiency* η_{eff} of the detector for a given transition (given photon energy) is defined as the ratio between the number of events detected at the desired energy (net peak area) and the number of transitions at that energy generated by the Montecarlo simulation:

$$\eta_{eff} = \frac{N_{peak}}{N_{events,tot} \cdot Br} \quad (32)$$

This definition includes the efficiency dependence on z , averaging it through a simulation which realistically includes all the possible experimental effects. For example, the *true coincidence summing effects* are considered. A nuclear reaction can proceed through gamma cascades that populate intermediate excited states. If the lifetime of the states is shorter than the time resolution of the detector, the detected signal is equal to the sum of the cascade photon energies. This leads to a loss of counts in the photopeak of the single photons. The entity of the effect depends on the probability



(a)



(b)

Figure 39: Comparison between simulated and experimental spectra for ^{60}Co (a) and ^{137}Cs (b) sources. Spectra are normalized to the total area.

of simultaneous detection of simultaneously emitted photons and it is therefore a function of the geometry of the setup. The further from the detector is the photon emission, the less probable the simultaneous detection is. Our simulation code reproduces this effect: since in this case the number of generated photons for each possible transition is known, the simulations can be used to compute correction factors for each transition.

Energy spectra were obtained simulating the reaction at different beam energies. An example of the spectra for the two detectors at a beam energy of 330 keV is shown in Figure 40. The spectral resolution is infinite, so that peaks coming from ^{21}Na excited state de-excitation have only an intrinsic delta width and peaks due to transitions from initial $p + ^{20}\text{Ne}$ continuous state to ^{21}Na excited levels are widened only by Doppler effect (these are respectively referred to as secondary and primary peaks, as better explained in Section 9.1).

Applying Eq. 32 to the peaks corresponding to the transitions we observe in the experimental spectra, I obtained the values for effective efficiency at the different beam energies. Results for two relevant transitions, which will be used in the successive data analysis, are collected in Table 10. The uncertainty associated to effective efficiency can be derived from the discrepancies between the

EFFICIENCY				
$E_{beam}(LAB)(keV)$	2425 \rightarrow 0 keV transition		$DC \rightarrow$ 2425 keV transition	
	GePD	GeDD	GePD	GeDD
400.1	3.7168E-03	2.0868E-03	-	-
380.4	3.7325E-03	2.0990E-03	-	-
329.7	3.7384E-03	2.1349E-03	9.3126E-03	7.0925E-03
319.0	3.7508E-03	2.1400E-03	9.6881E-03	7.6617E-03
309.7	3.7498E-03	2.1738E-03	1.0347E-02	8.6587E-03
299.3	3.7601E-03	2.1741E-03	9.5790E-03	7.4315E-03
259.7	3.7839E-03	2.2495E-03	9.4940E-03	7.3177E-03

Table 10: Effective efficiency for 2425 \rightarrow 0 keV and $DC \rightarrow$ 2425 keV transitions for the two detectors at different beam energies. Only values from peaks visible in experimental spectra are reported.

simulated and the experimental spectra at the different beam energies. A relative uncertainty of $\sigma_{\eta,PD} = 4\%$ is found for GePD, whose efficiency was better reproduced by Geant 3 simulation. For GeDD the uncertainty is slightly higher, $\sigma_{\eta,DD} = 5\%$.

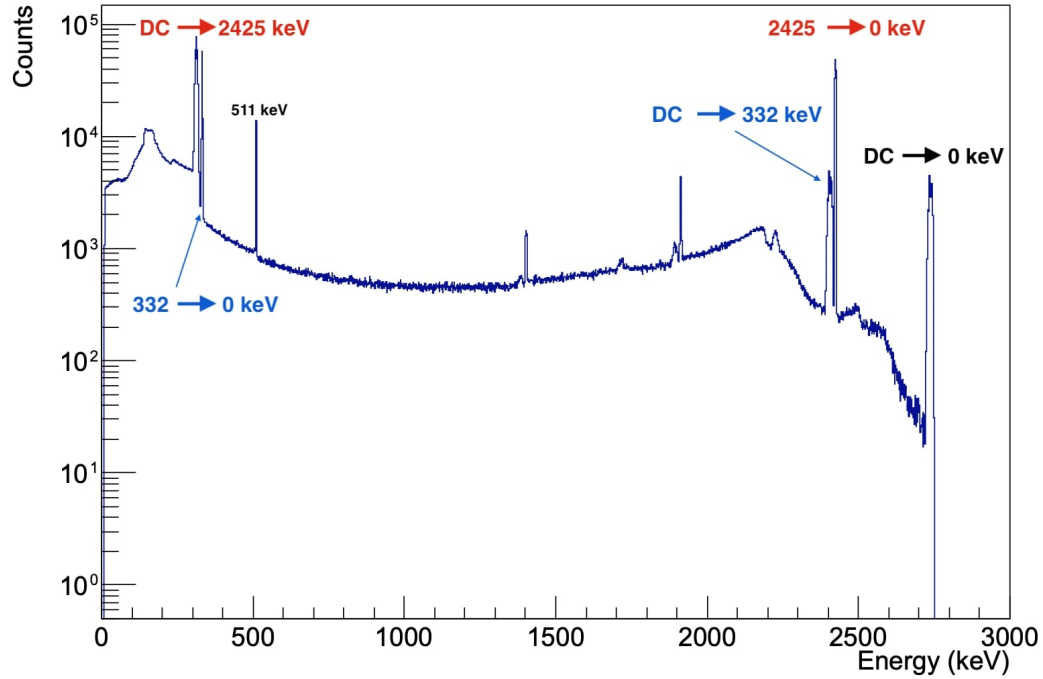
9 Data analysis

The goal of this analysis is to associate a cross-section to the $^{20}\text{Ne}(p,\gamma)^{21}\text{Na}$ at the energies explored during the measurement campaign. Since we are dealing with a direct capture, this is equivalent to evaluate the S-factor of the reaction. In particular, this analysis is focused on the direct capture branching involving the 2425 keV excited level, which is the transition contributing more to the total cross section, having the higher branching ratio.

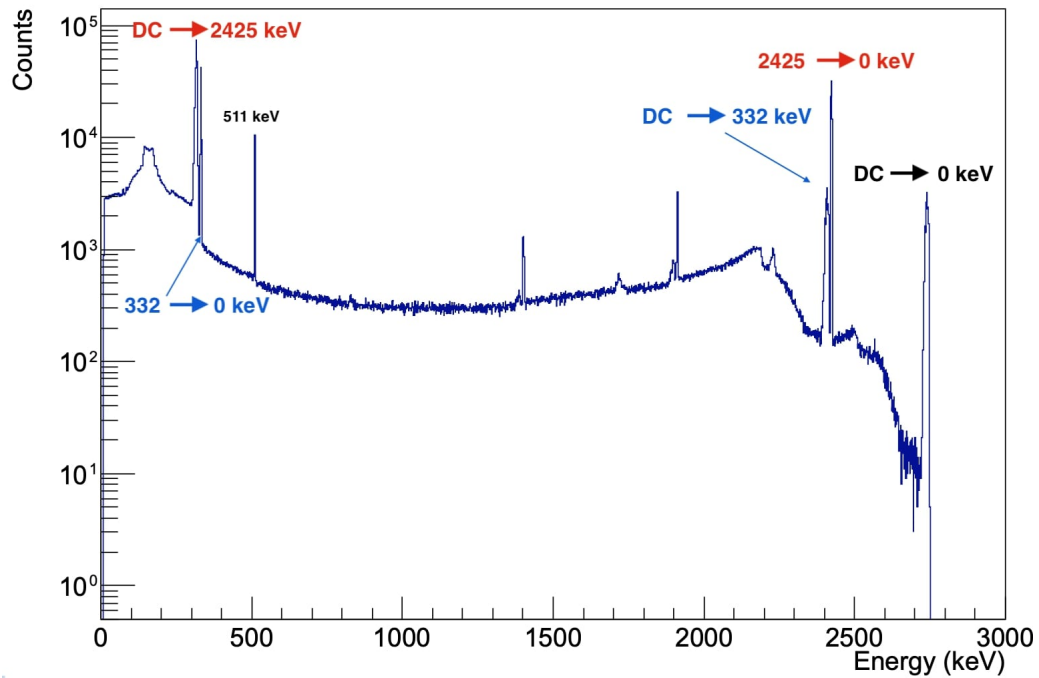
First of all we can define the measured reaction yield as

$$Y = \frac{N_{reaction}}{N_{projectiles}} = \frac{A \cdot e}{Q} \quad (33)$$

where A is the detected number of photons produced by the reaction, e the elementary charge and Q the total charge (in coulomb) deposited on the calorimeter. The number of protons reaching

GePD simulated spectrum at $E_{\text{beam}} = 330$ keV

(a)

GeDD simulated spectrum at $E_{\text{beam}} = 330$ keV

(b)

Figure 40: Simulated spectra of $^{20}\text{Ne}(p, \gamma)^{21}\text{Na}$ direct capture for GePD (a) and GeDD (b) at a beam energy of 330 keV. Most relevant transitions are highlighted. Other peaks that appear in the spectra correspond to single and double escape peaks.

the target chamber and possibly reacting with neon nuclei is in fact given by $N_{projectile} = \frac{Q}{e}$. It has to be stressed than in the usual yield definition at the denominator there is also the detection efficiency η_γ for the energy E_γ of the photons produced by the reaction. The number of reactions that has actually taken place is the number of detected photons corrected for this efficiency. In this analysis, however, we are dealing with an extended target: this means that, as mentioned in the previous section, the detector will see the photons coming from different target position with different intrinsic efficiency. The η_γ has therefore to be found not only at the desired photon energy, but also at the position in the target where the reaction has taken place. The efficiency is therefore included in the yield definition in a different way, as explained below.

We can imagine to divide the target into slices of thickness Δz , such that the beam energy loss in each slice is infinitesimal. This implies that both cross-section σ and stopping power ϵ are constant over each Δz . We can then use the cross-section definition

$$\sigma = \frac{\text{number of reactions per unit time}}{\text{number of projectiles per unit area and time} \cdot \text{number of target nuclei within projectile beam}} \quad (34)$$

$$\sigma = \frac{N_R/t}{N_p/tA \cdot N_t} \xrightarrow{\text{target area} \gg \text{beam area}} \frac{N_R}{t} = \frac{N_p}{t} \cdot \frac{N_t}{A} \cdot \sigma \quad (35)$$

and the stopping power definition in units of $\frac{eVcm^2}{atoms}$

$$\epsilon = \frac{1}{\rho} \frac{dE}{dz} \quad (36)$$

where ρ is the number density of target active ^{20}Ne nuclei, such that, if Δz is the unit path length,

$$\rho = \frac{N_t}{A\Delta z} \quad (37)$$

Combining these, we can write the yield produced by the i-th target slice as

$$Y_i = \frac{N_{R,i}}{N_p} = \sigma_i \frac{N_t}{A} = \sigma_i \rho_i \Delta z_i \quad (38)$$

or, considering that the experimental (measured) yields must be corrected by the detector efficiency η in measuring the number of reactions,

$$Y_i = \sigma_i \eta_i \rho_i \Delta z_i \quad (39)$$

If we integrate over all the target slices, we obtain a link between the experimental yield and the cross-section according to

$$Y_{\text{exp}}(E_0) = \int_{z_{in}}^{z_{fin}} \sigma(z) \rho(z) \eta_\gamma(z) dz = \int_{z_{in}}^{z_{fin}} \sigma(z) \rho(z) \eta_\gamma(z) \frac{dE(z)}{dz} \frac{dz}{dE(z)} dz \quad (40)$$

$$Y_{\text{exp}}(E_0) = \int_{z_{in}}^{z_{fin}} \frac{\sigma(z)}{\epsilon(z)} \eta_\gamma(z) \frac{dE}{dz}(z) dz \quad (41)$$

where

- z_{in} is the initial position introduced for density profiles calculations in Section 7
- z_{fin} is the position of the calorimeter

- E_0 is the initial beam energy (namely the beam energy at z_{in})
- $\frac{dE}{dz}(z) = \epsilon_{SRIM}(z) \cdot \rho(z)$ is the the stopping power for hydrogen in neon gas in units of $\frac{keV}{cm}$ at z , position where the beam has a certain energy E , on which the stopping power depends. The neon number density is ρ , referring here to the whole mixture.
- $\eta_\gamma(z)$ the detection efficiency for a photon of energy E_γ emitted at the position z . This implies that we perform the integral along the beam path taking into account the profile of the detection efficiency through the target.

The term ϵ in Eq. 41 is the *effective stopping power*. Effective here means that you need to exclude the presence of neon isotopes other than ^{20}Ne , considering that tabulated values (for example in SRIM) of stopping power refers to the whole isotopic mixture. While for energy loss calculations we had to consider the stopping given by all neon isotopes, for the yields we need to take into account only the proton interaction with the target one, in this case ^{20}Ne (active nuclei). In general, when more than one species is present, the effective stopping power is given by

$$\epsilon = \epsilon_x + \frac{n_y}{n_x} \epsilon_y \quad (42)$$

where x is the active element, y is the inactive element, ϵ_x/ϵ_y is the stopping power for the active / inactive element from SRIM, and n_x/n_y is the number of active / inactive nuclei per unit area. In the case of active ^{20}Ne nuclei in a natural neon gas, with percentage abundances given by 90.48 (2.01)% (^{20}Ne), 0.27(1.44)% (^{21}Ne), 9.25(0.72)% (^{22}Ne), the effective stopping can be found by assuming that for all isotope ϵ is essentially the same, giving

$$\epsilon = \frac{\epsilon_{Ne,SRIM}}{0.9048} \quad (43)$$

The value of $\epsilon_{Ne,SRIM}$ is given in units of $\frac{keV}{atoms/cm^2}$ if in Eq. 41 we use the energy in units of keV. It has to be noted that Eq. 40 and Eq. 41 are essentially the same. In fact, looking at $\frac{dE}{dz}$ and ϵ expression, it is clear that that in Eq. 41 the term $\frac{dE}{dz}$ simplifies with the effective stopping power appearing at the denominator, leaving the neon number density times the ^{20}Ne isotopic fraction (0.9048) at the numerator. This product is exactly the number density of active ^{20}Ne target nuclei, which appears in Eq. 40. I have decided to adopt Eq. 41 for my data analysis, since it gives a more operative way to implement the evaluation of the integral starting from experimental data, in particular the tabulated stopping power and the density profiles, which are respectively referred and measured considering the whole neon mixture and not just the active ^{20}Ne nuclei.

We can then further express the cross-section as already done in Section 2.1 and assume with good approximation the constancy of the S-factor for the direct capture process, thus obtaining

$$Y_{exp}(E_0) = S(E_{eff}) \cdot \int_{z_{in}}^{z_{fin}} \frac{e^{-2\pi\eta_S(E(z))}}{E(z)} \frac{\eta_\gamma(z)}{\epsilon(E(z))} \frac{dE}{dz}(E(z)) dz \quad (44)$$

Notice that since $\frac{dE}{dz} = \epsilon_{SRIM} \cdot \rho$, the dependence of the cross-section on the density is now explicit. The energy profile $E(z)$ represents the energy of the beam in the center of mass and takes into account beam energy loss. All quantities in the integral depend on the position z because of their dependence on the energy of the beam at that position. The energy profiles are the ones given in Figure 31 after the conversion in the center of mass frame.

The quantity E_{eff} represents the effective energy that we can associate to the S-factor value to

which the analysis will lead. For the present work, I have chosen it to be the energy at which half of the total experimental yields are obtained.

A good alternative approach to perform the integral considering $\eta_\gamma(z)$ profile has been adopted for this analysis. We can define the efficiency in detecting a photon with energy E_γ produced by a nuclear reaction as the ratio between the number of counts observed in a peak at E_γ and the number of photons actually produced at E_γ by the reaction. In the previous section we have found the effective efficiency following this reasoning applied to the Montecarlo simulation of $^{20}\text{Ne}(p, \gamma)^{21}\text{Na}$ direct capture, as:

$$\eta_{eff} = \frac{N_{c,sim}}{N_{r,sim}} \quad (45)$$

Of course, the same reasoning can be applied to the reaction reproduced in the laboratory, such that:

$$\eta_{eff} = \frac{N_{c,exp}}{N_{r,exp}} = \frac{A}{N_p \cdot S(E_{eff}) \cdot \int_{z_{in}}^{z_{fin}} \frac{e^{-2\pi\eta_S(E(z))}}{E(z)} \frac{\eta_\gamma(z)}{\epsilon(E(z))} \frac{dE}{dz}(E(z)) dz} \quad (46)$$

where we have used Eq. 33 to express the number of reaction as the yield times the number of projectiles and the definition of yield given by Eq. 44. By combining Eq. 45 and 46 it follows that we can express the yield $Y_{exp}(E_0) = \frac{A}{N_p}$ using the effective efficiency derived from the Montecarlo simulation of the reaction with our setup, obtaining

$$Y_{exp}(E_0) = S(E_{eff}) \cdot \eta_{eff} \cdot \int_{z_{in}}^{z_{fin}} \frac{e^{-2\pi\eta_S(E(z))}}{E(z)} \frac{1}{\epsilon(E(z))} \frac{dE}{dz}(E(z)) dz \quad (47)$$

All quantities in Eq. 47, apart from the S-factor, can be evaluated from the experimental data derived as explained in following sections. In the end, inverting the formula, the S-factor value for the explored beam energies can be found.

9.1 Spectra energy calibration and net peak areas

The first needed quantity for the analysis is the number of photons coming from the reaction that has been recorded by LUNA HPGe detectors. During the campaign 10 HPGe gamma spectra for the different beam energies explored were acquired. Spectra from the runs performed at same beam energy were summed.

The spectral energy calibration was performed following a standard procedure. The goal of the calibration is to derive the relation between channels in the original spectrum (counts per channel) and energy bins of the final spectral energy distribution (counts per unit energy).

The calibration at *low energies* has been performed using standard radioactive sources emitting photons at well-known energies. In this analysis I have used the already introduced ^{60}Co and ^{137}Cs sources. With this approach it is possible to perform the calibration only up to $\simeq 1333$ keV, while $^{20}\text{Ne}(p, \gamma)^{21}\text{Na}$ reaction produces gamma rays also at higher energies. To extend the calibration to the *high energy* domain, the $^{19}\text{F}(p, \alpha\gamma)^{16}\text{O}$ reaction was exploited. Fluorine is a known contaminant in LUNA experimental setup and its reaction with the proton beam produces many lines, among which the $E_\gamma = 6130$ keV and its corresponding single and double escape peaks are easily recognizable in the spectrum (see Figure 42). This triplet adds three more energy vs channel data points that combined with sources' ones allow to perform the linear fitting with a relation of the type

$$E_\gamma = q + m \cdot channel$$

Results of the calibration for GePD and GeDD detectors are plotted in Figure 41. The calibration curve parameters m and q are also reported.

Typical calibrated spectra from the two detectors for a reference energy of $E_{beam} = 330$ keV,

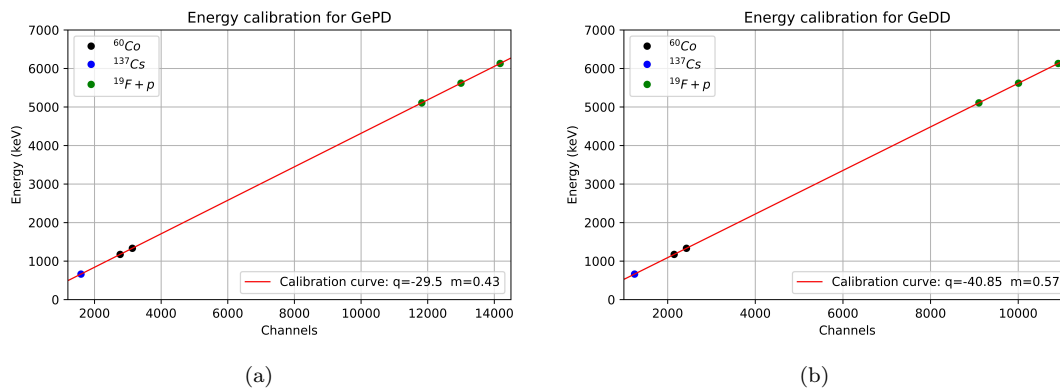
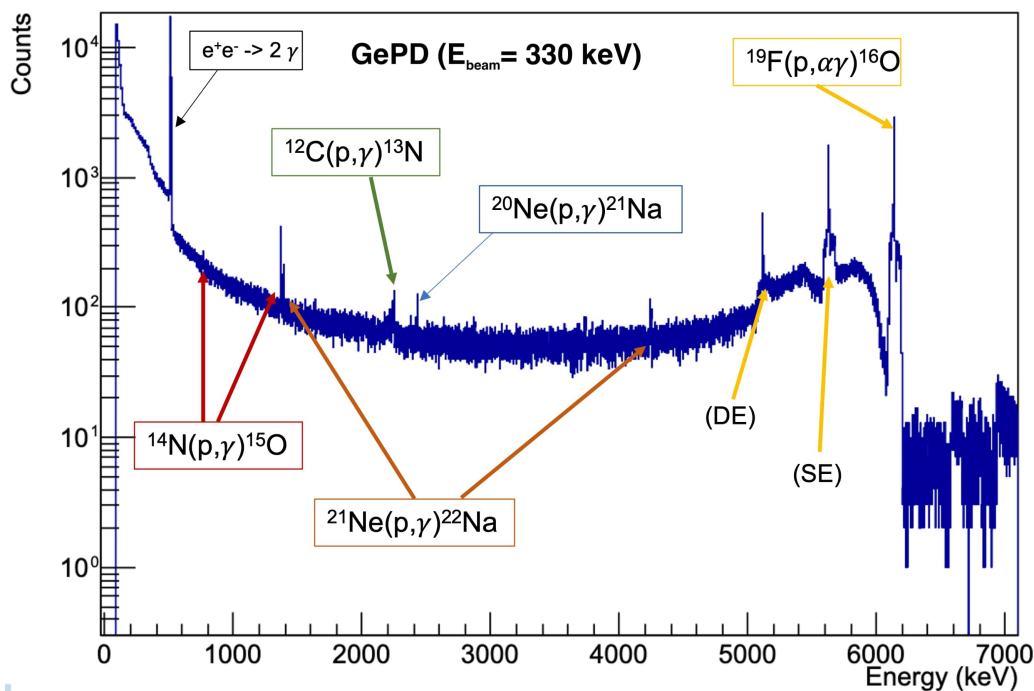


Figure 41: Energy calibration curve for the two detectors. Curve parameter m and q are reported, as well as experimental data points used for the calibration.

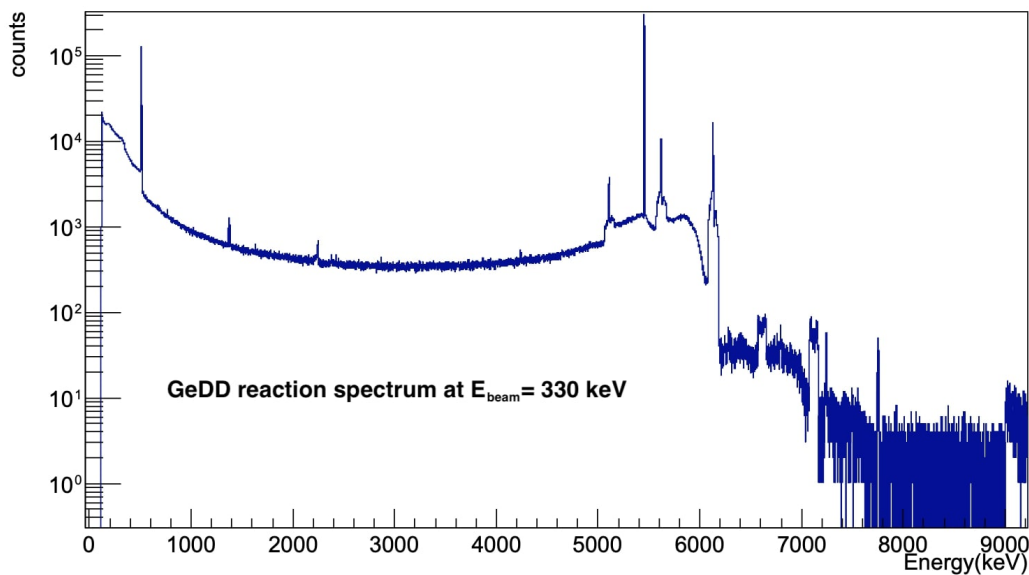
obtained applying to the channels the relation with energy found above, are shown in Figure 42. In GePD spectrum some of the most visible spectral peaks are highlighted and associated to the corresponding nuclear reactions. There are many peaks emerging from the continuum background and not connected to $^{20}\text{Ne}(p, \gamma)^{21}\text{Na}$ reaction. Focusing on Figure 42, the intense line at $E = 511$ keV is for example a typical feature of a germanium spectrum and corresponds to photons emitted when a positron and an electron annihilate each other and the resulting photons are successfully detected. The other peaks are instead mainly associated to contaminants contributing to the experimental background. There are no contaminants transitions which fall exactly in the regions of interest for the $^{20}\text{Ne}(p, \gamma)^{21}\text{Na}$ reaction, but the Compton background, especially that coming from $^{19}\text{F}(p, \alpha\gamma)^{16}\text{O}$ peaks, represents a challenge for net peak area calculations and precision of final results. This is due to the fact that we are always subtracting the background to find reaction's photon counts. The higher the background, the higher the uncertainty on the counts that will be carried on through all successive analysis steps.

A zoom-in of GePD spectrum at energies where direct capture transitions (introduced in Section 3.1) for beam energy of 310 keV are visible is reported in Figure 43. With current campaign achieved statistics we were able to observe with enough significance only the peaks involved in the direct capture (DC) to the 2425 keV ^{21}Na excited level. The so-called *primary peak*, associated with $DC \rightarrow 2425$ keV transition, is found at an energy which moves to lower values as beam energy decreases ($E_{gamma} = (Q_{value} + E_{cm} - 2425)$ keV, where E_{cm} changes from run to run). In Figure 43 (a) the primary peak maximum is located, as expected for $E_{lab} = 310$ keV, at $E \simeq 292$ keV¹⁶. At the two higher beam energies of $E_{lab} = 380$ and 400 keV the primary peak was not distinguishable from the background. The *secondary peak*, coming from excited level de-excitement to the ground state, is instead centered at $E = 2425$ keV independently on the beam energy and it is found in all spectra acquired. It is also possible to see a bump rising at $E \simeq 332$ keV. This correspond to the

¹⁶Actually it would be $E_{gamma} = Q_{value} + E_{cm} - 2425 \simeq 301$ keV, but we have to take into account the energy loss suffered by the initial beam energy of 310 keV at the position where the detector has its highest efficiency, right in front of it. Since for GePD this ΔE amounts to $\simeq 9$ keV, we expect the primary transition to be peaked around $\simeq 292$ keV



(a)



(b)

Figure 42: GePD (a) and GeDD (b) spectra of $^{20}\text{Ne}(p,\gamma)^{21}\text{Na}$ at 330 keV beam energy. Most important peaks arising from proton capture involving contaminants are highlighted in (a). Single and double escape peaks are also reported. Notice that, since the target is natural neon, also other neon isotopes may react with protons, especially if the beam energy is running close to a resonance involving that isotope (in this case ^{21}Ne). In (b), the intense line between $^{19}\text{F}(p,\alpha\gamma)^{16}\text{O}$ single and double escape peaks is the the pulser, which is part of the DAQ for GeDD detector. This produces a pulse signal at regular time intervals and from the comparison of the number of generated pulses with those actually detected, the dead time of the detector can be estimated.

secondary peak of $DC \rightarrow 331.9$ keV transition, but it is located right on the Compton edge¹⁷ of the 511 keV peak, making background subtraction quite challenging with such counting statistics. Further runs have therefore been performed in a more recent campaign in order to improve the statistics in the region and to allow the determination of a significant net peak area. Also the peak from the proton direct capture to the ground state of ^{21}Na could be better analyzed once higher counts in the peak are achieved by combining latest runs at same energies. These transitions will not be further considered in the following analysis. It can be however noted that the contribution to the total S-factor of the direct capture involving the 331.9 keV level and the direct capture to the ground state are not as much relevant as the one from the direct capture to the 2425 keV level, as hinted by the associated branching ratios. The number of photons with energies within the peak range is given by the *net peak area*. Net peak area of 2425 keV peak will be for example proportional to the number of direct capture reactions which have proceeded through the 2425 keV excited level. If we call B the average background counts per spectral bin and A the net peak area, we have that:

$$B = \sum_{i=L-m_{low}}^{L-1} C_i - \sum_{i=U+1}^{U+m_{up}} C_i \quad A = \sum_{i=L}^U C_i - \frac{nB}{m_{low} + m_{up}}$$

where n is the number of bins within the peak, m_{low} the number of considered background bins to the left of the peak, m_{up} those to the right, L the bin corresponding to the lower peak limit and U the analogous upper one. C_i represents the counts in the *i*-th bin. The statistical uncertainty associated to A is then given by:

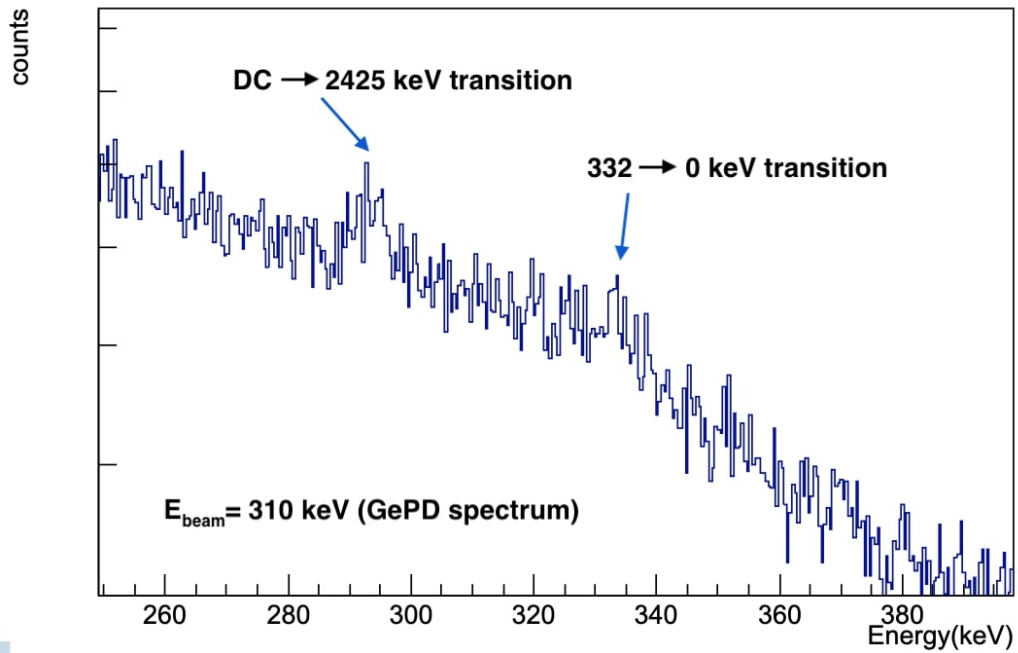
$$\sigma_A = \sqrt{A + B\left(1 + \frac{n}{m_{low} + m_{up}}\right)}$$

Different peak and background regions widths were adopted until A value was, within the uncertainty, independent on the boundaries choice. This approach was adopted for both primary and secondary peaks and the results are reported in Table 11. Generally speaking, the detector with lower relative efficiency (GeDD) shows a lower counting rate and higher uncertainties on net peak areas.

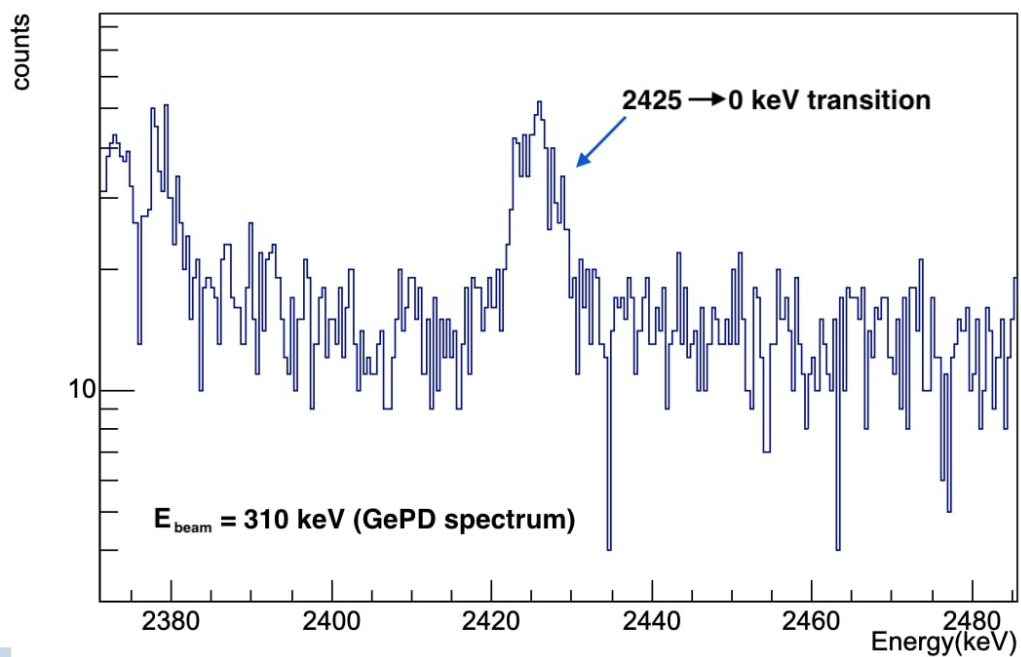
	E_{beam} (LAB) (keV)	A (GePD)	σ_A (GePD)	A (GeDD)	σ_A (GeDD)
Secondary peak	400.1	1416	267	1066	323
	380.4	1810	382	841	466
	329.7	1483	117	913	135
	319.0	547	54	377	58
	309.7	481	42	259	45
	299.3	662	53	434	50
	259.7	193	30	128	50
Primary peak	329.7	3445	573	2846	741
	319.0	1569	236	1155	295
	309.7	1037	217	920	238
	299.3	1864	451	1355	318
	259.7	350	185	448	237

Table 11: Photon counts (net peak areas A) and associated uncertainties derived from reaction spectra. values for both secondary and primary peaks relative to the $DC \rightarrow 2425$ keV transitions are shown.

¹⁷This is a sharp energy cut-off in a gamma spectrum, corresponding to photons Compton scattered at 180° in the detector, transferring to the electrons the maximum possible amount of energy.



(a)



(b)

Figure 43: Zoom-in of relevant regions in GePD spectra at a beam energy of 310 keV. The secondary peak from 2425 keV level de-excitation is well visible in (b), while in (a) the corresponding primary is seen, together with a slowly raising 332 keV level de-excitation secondary peak.

9.2 Energy loss and charge determination

Other two important quantities that has to be determined are the charge Q and the total energy loss in the target ΔE . The total energy loss is found from Eq. 23, integrating over the whole beam path. The charge Q in C is found by multiplying the run beam current given by Eq. 19 to the corresponding live time of the run, reported in Table 8. The powers provided by resistors with and without beam (respectively W and W_0 in Eq. 19) are measured and recorded during/before each run, so that the value used in the equation is simply the mean value of all the powers for the corresponding run. The associated errors are the quadrature sum of systematic and statistical errors associated to the charge. The systematic uncertainty is given by the usual propagation of uncertainties rules, considering errors combination on:

- Energy loss: relative uncertainty of 1.7% for the stopping power and 1.1% for the density profile
- Beam energy: 0.3 keV absolute uncertainty
- Power read by the resistors on the calorimeter: relative systematic uncertainty of 1%

The statistical error is instead given by the standard deviation of the mean of the resistors powers. All the obtained values are summarized in Table 12.

E_{beam} (LAB) (keV)	Charge Q (C)	σ_Q (C)	Energy loss ΔE (keV)
400.1	43.65	0.52	4.82
380.4	17.00	1.64	19.35
329.7	47.94	1.42	20.19
319.0	24.75	0.29	20.48
309.7	22.85	1.00	20.73
299.3	48.17	0.73	21.06
259.7	43.75	1.05	22.30

Table 12: Charge accumulated on the calorimeter during each run with its total uncertainty and beam energy loss in the target for each of the explored beam energies.

9.3 Experimental yields

Using Eq.33, we can finally calculate the experimental yields for the two transitions seen in the spectra and for each of the two detectors. Statistical and systematic uncertainties are obtained propagating the uncertainties with the partial derivatives method, according to:

$$\sigma_Y^{stat} = e \sqrt{\left(-\frac{A}{Q^2} \cdot \sigma_Q^{stat}\right)^2 + \left(\frac{1}{Q} \cdot \sigma_A\right)^2} \quad \sigma_Y^{syst} = \frac{eA}{Q^2} \cdot \sigma_Q^{syst} \quad (48)$$

The obtained experimental yields for primary and secondary peak are plotted in Figure 44 as counts normalized to a charge of 100 μC . The error reported is the sum in quadrature of systematic and statistical one. We can see an increasing trend with increasing energies, due to the corresponding expected increase in the cross-section at larger energies in the center of mass. The value at $E_{beam}=400$ keV is lower than the trend, because the run was performed at a lower pressure (and density) with respect to the others.

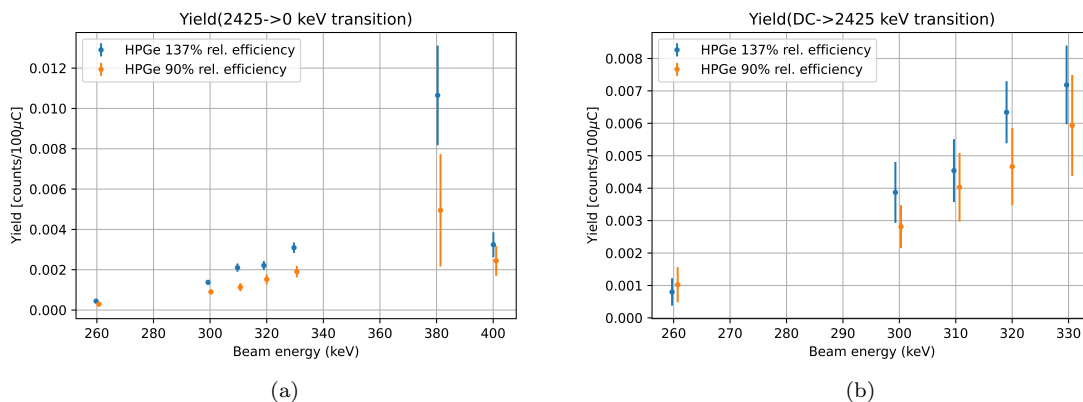


Figure 44: Experimental yields of $^{20}\text{Ne}(p, \gamma)^{21}\text{Na}$ direct capture for the two transitions involving the 2425 keV excited state at the beam energies explored during the campaign. Yields are normalized to counts per $100\mu\text{C}$ charge.

9.4 S-factor

The S-factor for the $^{20}\text{Ne}(p, \gamma)^{21}\text{Na}$ direct capture component involving the 2425 keV excited level can be now evaluated by inverting the formula given by Eq. 47. The final S-factor formula is therefore:

$$S(E_{eff}) = \frac{Y_{exp}}{\eta_{eff} \cdot \int_{z_{fin}}^{z_{in}} \frac{e^{-2\pi\eta_s(E(z))}}{E(z)} \frac{1}{\epsilon(E(z))} \epsilon_{SRIM}(E(z)) \cdot \rho(z) dz} \quad (49)$$

The corresponding statistical and systematic uncertainties can be found propagating the relative errors following standard rules for products. The former depends only on the statistical uncertainty of the experimental yields, while the latter includes the major systematic uncertainties linked to:

- experimental yields: σ_Y^{stat}
- stopping power: $\sigma_\epsilon = 1.7\%$
- efficiency: $\sigma_\eta = 4\%$ (GePD) and $\sigma_\eta = 5\%$ (GeDD)
- density profile including beam heating effect: $\sigma_\epsilon = 1.1 - 1.5\%$, depending on beam energy
- beam energy: $\sigma_E = 0.3/E_{beam}$

In formulas (denoting as I the integral term):

$$\sigma_S^{stat} = \frac{1}{\eta_{eff} \cdot I} \sigma_Y^{stat} \quad \sigma_S^{syst} = \sqrt{(\sigma_{Y,rel}^{syst})^2 + (\sigma_\eta)^2 + (\sigma_I)^2} \quad \sigma_I = \sqrt{(\sigma_\rho)^2 + (\sigma_E)^2 + (\sigma_\epsilon)^2}$$

Calculations performed using the quantities relative to secondary and primary peak give the preliminary results reported in Table 13 and Table 14. The S-factor is written in units of $\text{keV} \cdot \text{barn}$, where $1 \text{ barn} = 10^{-24} \text{ cm}^2$. The effective energy has been found with the approach previously mentioned: beam energy in the center of mass where half of the experimental yields were produced. Since the efficiency curve for the two detectors is different, half yields are reached at slightly different position in the chamber. In particular, GeDD efficiency's maximum is closer to the beam start and will therefore reach half of the total yield at a higher beam energy and a higher effective energy is associated to the S-factor. The final systematic uncertainties are of 5% for GePD S-factor and 6% for GeDD one.

Of course, the number of photons decaying from the 2425 keV state (counts in the secondary peak)

PRELIMINARY S-FACTOR $DC \rightarrow 2425$ keV (secondary peak)					
$E_{effective}$ (keV)	S_{GePD} (kev barn)	$\sigma_{S,PD}$	$E_{effective}$ (keV)	S_{GePD} (kev barn)	$\sigma_{S,DD}$
379.5	9.02	1.75	380.1	12.10	3.73
355.2	12.41	2.93	357.8	10.25	5.79
306.7	11.14	1.07	309.4	12.01	1.93
296.5	10.40	1.14	299.2	12.56	2.05
287.5	12.68	1.37	290.2	11.81	2.21
277.6	11.03	1.03	280.4	12.52	1.61
239.5	12.66	2.07	242.5	14.13	5.57

Table 13: S-factor and its uncertainty for the $DC \rightarrow 2425$ keV transition, calculated analyzing the secondary peak at $E_\gamma = 2425$ keV from both detectors. The beam energy reported are the effective ones.

PRELIMINARY S-FACTOR $DC \rightarrow 2425$ keV (primary peak)					
$E_{effective}$ (keV)	S_{GePD} (kev barn)	$\sigma_{S,PD}$	$E_{effective}$ (keV)	S_{GePD} (kev barn)	$\sigma_{S,DD}$
306.7	10.39	1.75	309.4	11.27	2.95
296.5	11.78	1.78	299.2	11.24	2.87
287.5	10.71	2.29	290.2	12.25	3.21
277.6	12.06	2.92	280.4	11.09	2.61
239.5	8.38	4.43	242.5	12.81	6.78

Table 14: S-factor and its uncertainty for the $DC \rightarrow 2425$ keV transition, calculated analyzing the primary peak from both detectors. The beam energy reported are the effective ones.

must be equal to the number of photons produced by the direct capture to the 2425 keV excited state (counts in the primary peak). This means that we expect, at fixed beam energy, that the values for the S-factor derived from the two transitions to be compatible within their uncertainties. In Figure 45 the aforementioned S-factor are plotted for the two detectors for the beam energies at which both peaks were visible. The values are congruent. The higher uncertainty of the S-factor derived from the primary peak are due to the fact that the net peak areas of the primary peak are considerably more uncertain than secondary peak ones, also because of the more challenging background subtraction. By looking at LUNA S-factor values coming from the secondary peak analysis, which have a higher precision, it can be seen that GePD and GeDD S-factor are compatible within their error bars, as shown in Figure 46. Since the two detectors has a maximum in their efficiency at different position in the target chamber, they will see most of the reactions products from different target regions. The compatibility of the derived S-factor therefore implies that there are no particular further effects to be taken into account, such as the angular distribution of emitted photons. LUNA S-factor for the direct capture to the 2425 keV state of $^{20}\text{Ne}(p, \gamma)^{21}\text{Na}$ reaction is plotted in Figure 47, together with relevant results from literature presented in Section 4. LUNA reported values are in this case the weighted average of the S-factor from the two detectors, using the associated statistical uncertainties as weights. The S-factors effective beam energies are an average of the values from each germanium. Only statistical errors are reported for a true comparison with the state of the art. LUNA S-factor values are in agreement with the trend provided by previous works, providing data with small uncertainty in a low energy region poorly explored by previous experiments.

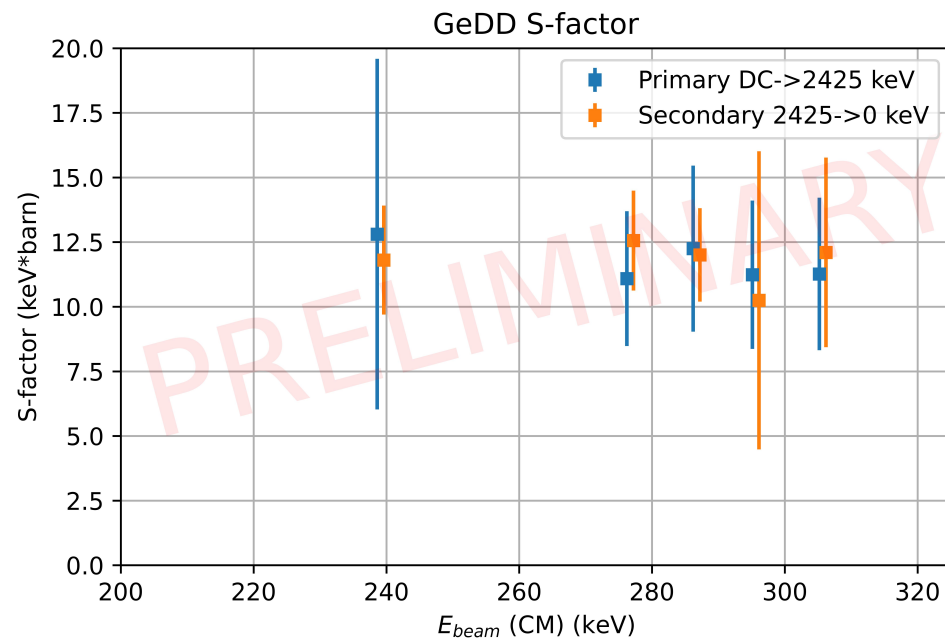
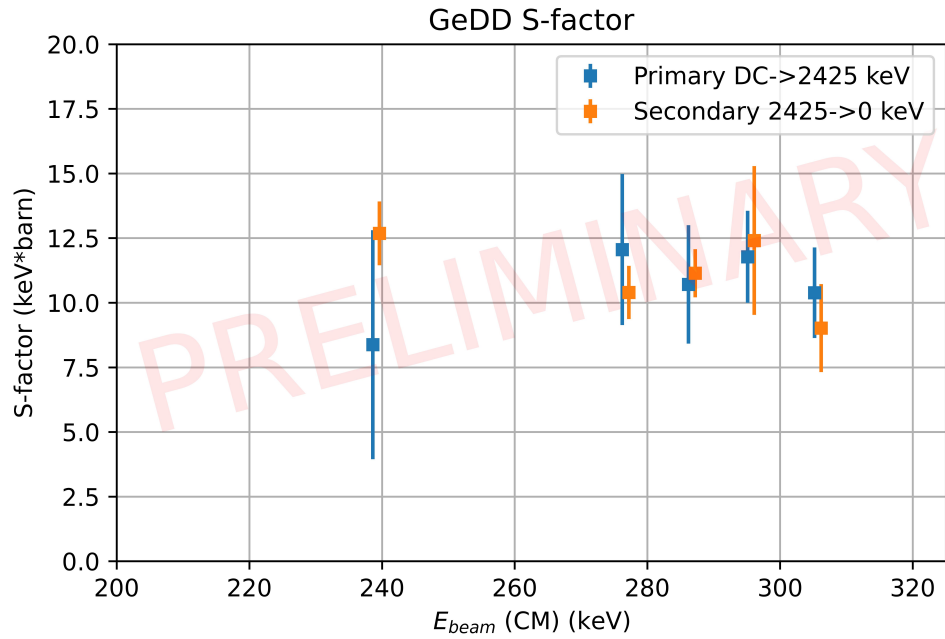


Figure 45: Comparison between S-factor from primary and from secondary peaks for the two detectors. The values are compatible within their statistical uncertainties.

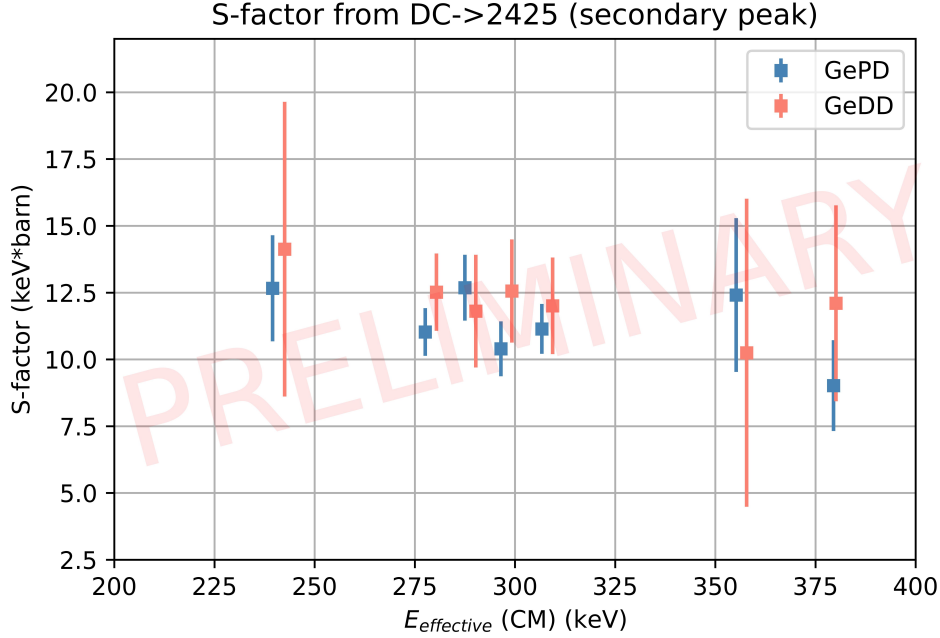


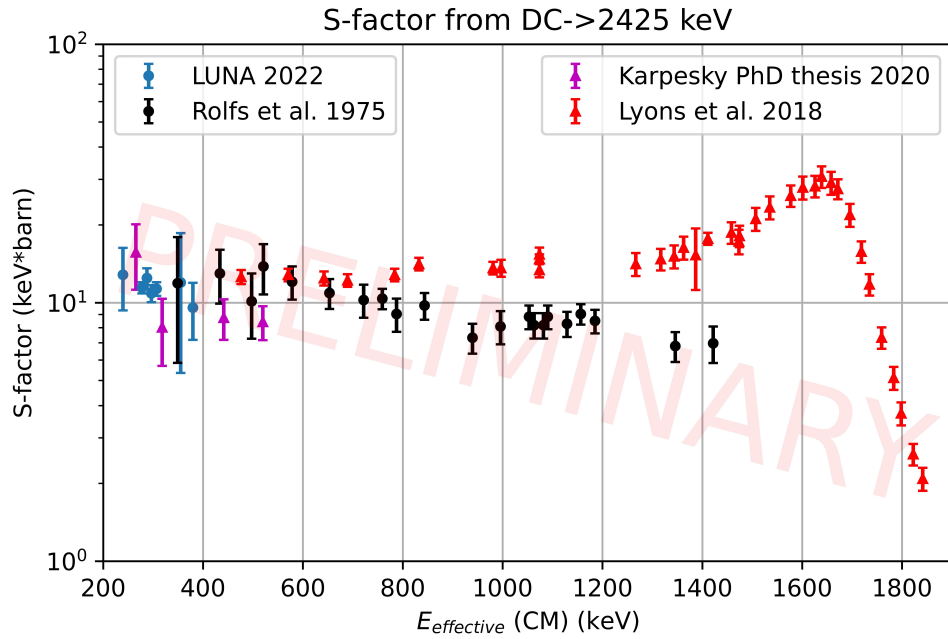
Figure 46: S-factor values derived from the analysis of secondary peak, corresponding to 2425 keV level de-excitation. Values from both detectors are reported with the corresponding independent uncertainties. GePD and GeDD provide values for S compatible within their uncertainties. The difference in the effective energy of the measurement is due to the different efficiency of the detectors.

10 $^{20}\text{Ne}(p, \gamma)^{21}\text{Na}$ reaction rate

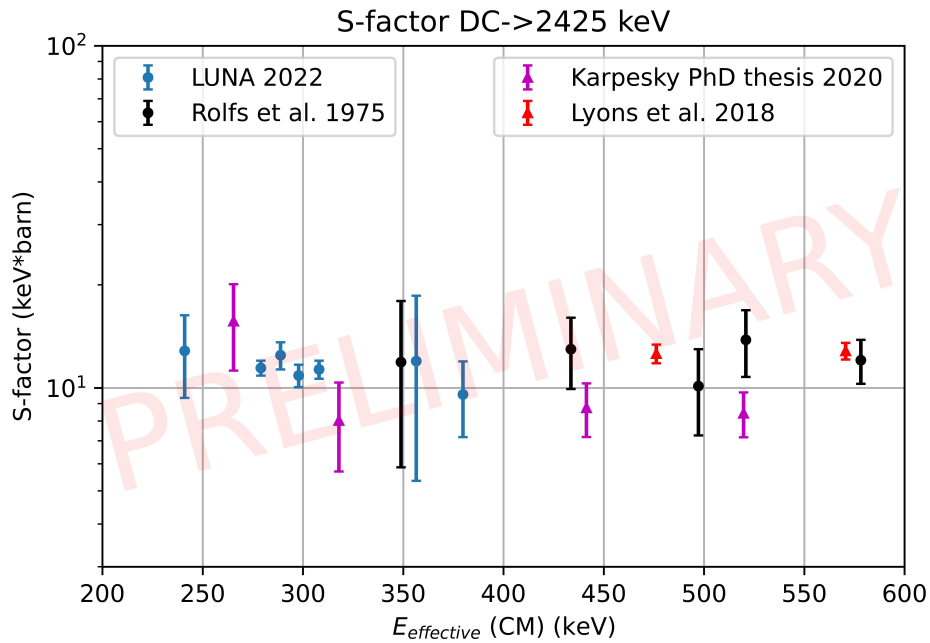
Combining S-factor literature data ([3],[41],[36]) and LUNA data provided by this thesis, a complete extrapolation of the S-factor for the direct capture was performed using AZURE2 R-matrix code [63]. AZURE2 is a multilevel code of various nuclear astrophysics applications. The code allows simultaneous analysis and extrapolation of reaction cross-sections relevant for stellar hydrogen, helium, and carbon burning. In Figure 48 the S-factor at different energies in the center of mass is reported. The plots refer to the $DC \rightarrow 2425$ keV component, on which this analysis was focused, and to the total S-factor, obtained from the combination of the three main components of the direct capture process. This is a preliminary extrapolation, which will be refined also including data coming from a more recent measurement campaign.

Using the extrapolated S-factor, a reaction rate calculation for $^{20}\text{Ne}(p, \gamma)^{21}\text{Na}$ following the approach described in [64]. The resonance strength for the 366 keV narrow resonance, which has been deeply studied at LUNA [42], was also included in the calculation. In particular, since narrow resonances are challenging to be included in the integration, a non resonant S-factor extrapolation was used, obtaining at first a non resonant reaction rate. Then, the narrow resonances contribution was added to the reaction rate as described by [64].

Preliminary results for the $^{20}\text{Ne}(p, \gamma)^{21}\text{Na}$ reaction rate are reported in Figure 49. The rate is calculated over a wide range of stellar temperatures and is compared with the more recent available in literature from [3]. In the plot both rates are normalized to [3] for a simpler visualization. The relevant temperature range for $^{20}\text{Ne}(p, \gamma)^{21}\text{Na}$ reaction in astrophysical nucleosynthesis environments is approximately between 0.2 and 1 GK. This preliminary analysis shows a slightly higher



(a)



(b)

Figure 47: (a) $^{20}\text{Ne}(p,\gamma)^{21}\text{Na}$ S-factor for $DC \rightarrow 2425$ keV state at effective beam energies from literature. LUNA data are reported in blue and correspond to the weighted mean of the S-factors found from the two detectors. Only statistical errors are reported. (b) A zoom in of the S-factors in the energy region explored by LUNA campaign.

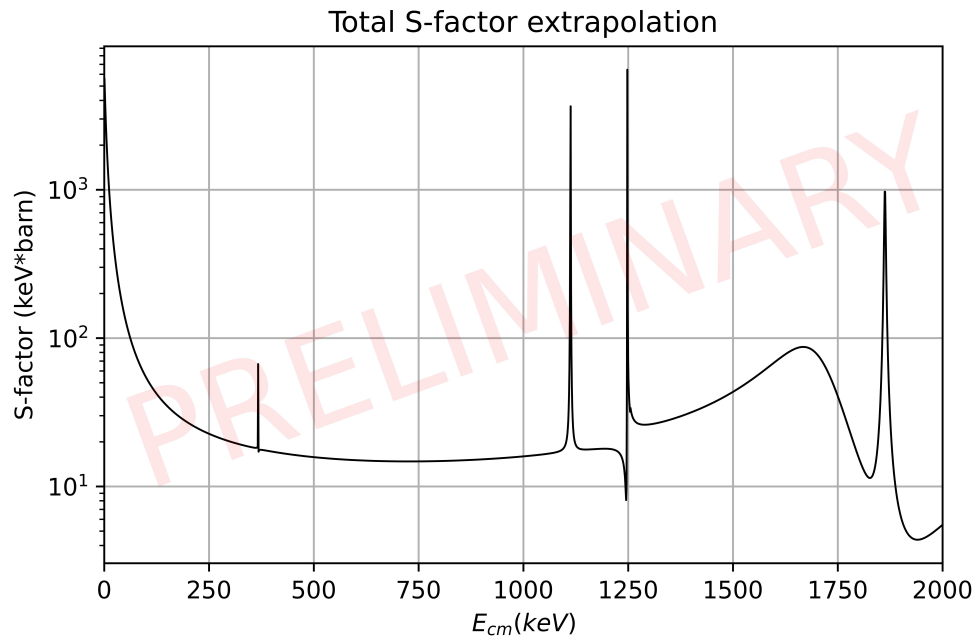
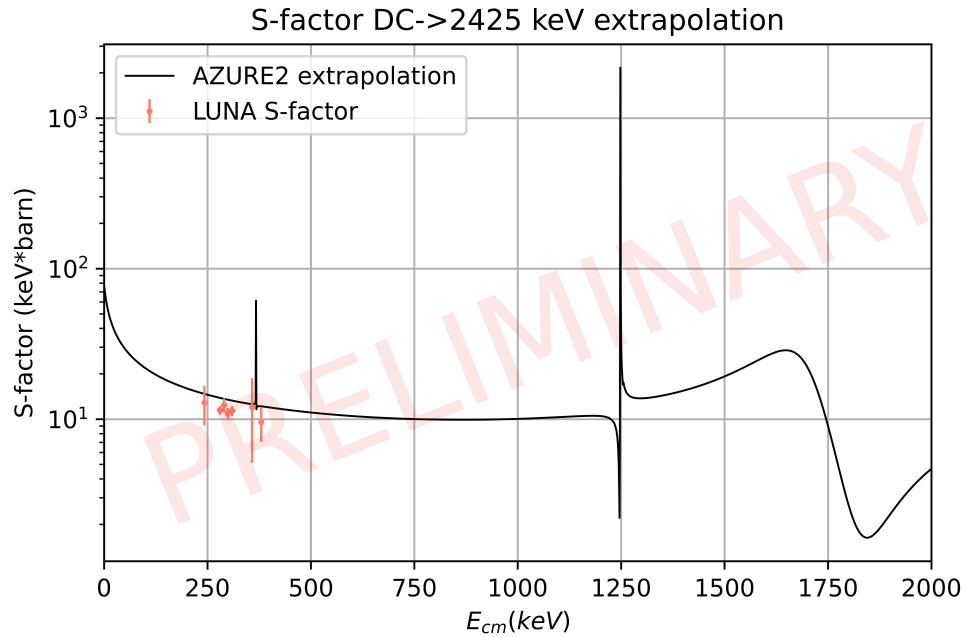


Figure 48: Preliminary S-factor extrapolation over a wide range of energies in the center of mass. The calculation has been performed using AZURE2 code. In (a) is shown the S-factor $DC \rightarrow 2425$ keV component, with LUNA values from Figure 47 also reported in salmon, in (b) the total S-factor extrapolation.

rate than the one provided by [3] in the lower temperature region, while rates are in agreement in the higher temperature side. The uncertainties have not been included in the calculations yet, but

they will be evaluated for the upcoming LUNA paper on $^{20}\text{Ne}(p, \gamma)^{21}\text{Na}$ reaction.

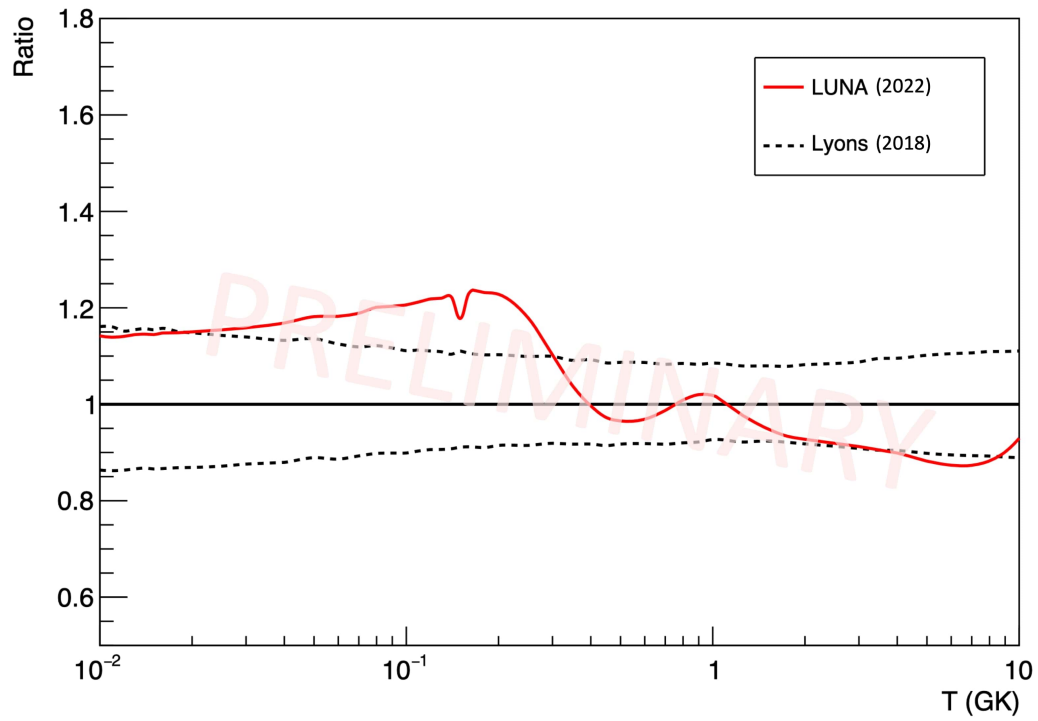


Figure 49: Lyons et al. (2018) [3] and preliminary LUNA (2022) $^{20}\text{Ne}(p, \gamma)^{21}\text{Na}$ reaction rates at various stellar temperatures. The rates are plotted normalized to [3]'s one. LUNA rate does not include the associated uncertainties yet.

11 Conclusions and future perspectives

The goal of the present master thesis was the study of the direct capture of $^{20}\text{Ne}(p, \gamma)^{21}\text{Na}$, an important nuclear reaction taking place during the Ne-Na cycle in various stellar environments. Cross-section measurements were performed at LUNA laboratory, using a windowless gas target filled with natural neon and two HPGe detectors. Beam energies between 260 and 400 keV in the laboratory rest frame were explored, providing S-factor values in a poorly explored energy window close to the relevant one for stellar nucleosynthesis sites. In particular, for ONe novae at a typical temperature of 0.4 GK the Gamow window $E_0 \pm \frac{\Delta}{2}$ is centered at $E_0 \simeq 303$ keV, with an effective width of $\Delta \simeq 236$ keV. Since the effective energies associated to our preliminary S-factor measurements are between ≈ 239 and 380 keV, we are able to provide new precise direct data in the Gamow window of such objects.

Thanks to the achieved low uncertainty on low energy data, S-factor extrapolation down to the Gamow peak can be improved by LUNA S-factor measurements. This thesis provide a preliminary extrapolation including LUNA data. The extrapolation has then been adopted to evaluate $^{20}\text{Ne}(p, \gamma)^{21}\text{Na}$ reaction rate at relevant stellar temperatures. The rate is preliminary and does not include yet the uncertainties, but it shows a higher value than literature's one in the temperature region corresponding to classical ONe novae (below 0.4 GK).

During the campaign presented in my thesis, only two of the possible transitions were seen in the reaction spectra with sufficient resolution. The S-factor here provided is therefore only a partial one, even if its contribution to the total one is the highest, because of the high branching ratio of the $DC \rightarrow 2425$ keV transition. During Summer 2022 further data taking has been performed in order to increase the statistics at certain beam energies. These energies were selected among the ones which showed a lower experimental background and therefore seemed promising for the purpose of observing with enough significance peaks from other direct capture transitions. Data analysis similar to the one presented here will be performed, so as to derive the total S-factor. If all the transitions are observed, also LUNA branching ratios for direct capture could be derived.

From the combination of the total direct capture S-factor with the resonance strength of the important 366 keV resonance, recently improved by LUNA, updated thermonuclear reaction rate for $^{20}\text{Ne}(p, \gamma)^{21}\text{Na}$ will be presented by LUNA collaboration in the near future. Thanks to improved nuclear inputs, stellar evolution and chemical enrichment models applied to Ne-Na burning cycle environments will be able to predict produced abundance patterns and ejecta composition with a high degree of reliability.

12 Acknowledgments

I would like to thank all the people who have contributed to this thesis work.

First of all, I am truly grateful to my supervisor Prof. Antonio Cacioli, who has given me the opportunity to meet and work with LUNA collaboration. Thanks for encouraging me throughout these months, for your kind support and your priceless advice.

Thanks to my co-supervisor Prof. Sandra Zavatarelli, always willing to help and advice me with enthusiasm and competence.

A special thanks to Dr. Eliana Masha and Prof. Pietro Corvisiero, who have been huge supporters from the beginning. Thanks for finding time to answer my many questions and for cheering me up when I needed it.

Thanks to all the LUNA people who have shared their shift with me at Gran Sasso National Laboratories. You have taught me so much and you have contributed to making my experience in the laboratories unforgettable.

Many thanks also to the technicians from Gran Sasso National Laboratories, in particular Donatello Ciccotti, for the helpfulness and the assistance in dealing with the troubles that a shift can reserve. Finally, I am thankful to all the members of LUNA collaboration for your precious contribution to this work. Working for the LUNA experiment has been a wonderful experience. I have met incredible people and I was delighted to learn something from each of you.



References

- [1] Christian Iliadis. *Nuclear physics of stars*. John Wiley & Sons, 2015.
- [2] Claus E. Rolfs and William S. Rodney. *Cauldrons in the cosmos : nuclear astrophysics*. 1988.
- [3] S. Lyons et al. “Determination of $^{20}\text{Ne}(p, \gamma)^{21}\text{Na}$ cross sections from $E_p = 500 - 2000$ keV”. In: *Phys. Rev. C* 97 (6 June 2018), p. 065802. DOI: [10.1103/PhysRevC.97.065802](https://doi.org/10.1103/PhysRevC.97.065802). URL: <https://link.aps.org/doi/10.1103/PhysRevC.97.065802>.
- [4] M. Wiescher et al. “The Cold and Hot CNO Cycles”. In: *Annual Review of Nuclear and Particle Science* 60.1 (2010), pp. 381–404. DOI: [10.1146/annurev.nucl.012809.104505](https://doi.org/10.1146/annurev.nucl.012809.104505). eprint: <https://doi.org/10.1146/annurev.nucl.012809.104505>. URL: <https://doi.org/10.1146/annurev.nucl.012809.104505>.
- [5] Jerry B. Marion and William A. Fowler. “Nuclear Reactions with the Neon Isotopes in Stars.” In: *Astrophys. J.* 125 (Jan. 1957), p. 221. DOI: [10.1086/146296](https://doi.org/10.1086/146296).
- [6] Robert M. Cavallo, Allen V. Sweigart, and Roger A. Bell. “The Production of Sodium and Aluminum in Globular Cluster Red Giant Stars”. In: *The Astrophysical Journal* 464.1 (June 1996), pp. L79–L82. DOI: [10.1086/310089](https://doi.org/10.1086/310089).
- [7] Robert M. Cavallo, Allen V. Sweigart, and Roger A. Bell. “Proton-Capture Nucleosynthesis in Globular Cluster Red Giant Stars”. In: *The Astrophysical Journal* 492.2 (Jan. 1998), pp. 575–595. DOI: [10.1086/305053](https://doi.org/10.1086/305053). URL: [American%20Astronomical%20Society](https://doi.org/10.1086/305053).
- [8] Lih-Sin The, Mounib F. El Eid, and Bradley S. Meyer. “s-Process Nucleosynthesis in Advanced Burning Phases of Massive Stars”. In: *The Astrophysical Journal* 655.2 (Feb. 2007), pp. 1058–1078. DOI: [10.1086/509753](https://doi.org/10.1086/509753). URL: <https://doi.org/10.1086/509753>.
- [9] M. Williams et al. “First inverse kinematics study of the $^{22}\text{Ne}(p, \gamma)^{23}\text{Na}$ reaction and its role in AGB star and classical nova nucleosynthesis”. In: *Phys. Rev. C* 102 (3 Sept. 2020), p. 035801. DOI: [10.1103/PhysRevC.102.035801](https://doi.org/10.1103/PhysRevC.102.035801). URL: <https://link.aps.org/doi/10.1103/PhysRevC.102.035801>.
- [10] C. Iliadis et al. “Charged-particle thermonuclear reaction rates: II. Tables and graphs of reaction rates and probability density functions”. In: *Nuclear Physics A* 841.1-4 (Oct. 2010), pp. 31–250. DOI: [10.1016/j.nuclphysa.2010.04.009](https://doi.org/10.1016/j.nuclphysa.2010.04.009). arXiv: [1004.4517 \[astro-ph.SR\]](https://arxiv.org/abs/1004.4517).
- [11] C. Iliadis et al. “Proton-induced Thermonuclear Reaction Rates for A=20-40 Nuclei”. In: *Astro-phys. J. Suppl. Ser.* 134 (2001), pp. 151–171.
- [12] R. Depalo. “The neon-sodium cycle: Study of the $^{22}\text{Ne}(p, \gamma)^{23}\text{Na}$ reaction at astrophysical energies”. PhD thesis. Università degli Studi di Padova, 2015.
- [13] F. Cavanna et al. “Three New Low-Energy Resonances in the $^{22}\text{Ne}(p, \gamma)^{23}\text{Na}$ reaction”. In: *Physical Review Letters* 115.25 (Dec. 2015). DOI: [10.1103/physrevlett.115.252501](https://doi.org/10.1103/physrevlett.115.252501).
- [14] F. Cavanna. “A direct measurement of the $^{22}\text{Ne}(p, \gamma)^{23}\text{Na}$ reaction down to the energies of astrophysical interest”. PhD thesis. Università degli Studi di Genova, 2015.
- [15] F. Ferraro et al. “Direct capture cross section and the $E_p = 71$ and 105 keV resonances in the $^{22}\text{Ne}(p, \gamma)^{23}\text{Na}$ reaction”. In: *Phys. Rev. Lett.* 121.17 (2018), p. 172701. DOI: [10.1103/PhysRevLett.121.172701](https://doi.org/10.1103/PhysRevLett.121.172701). arXiv: [1810.01628 \[nucl-ex\]](https://arxiv.org/abs/1810.01628).
- [16] K. J. Kelly et al. “New measurements of low-energy resonances in the $^{22}\text{Ne}(p, \gamma)^{23}\text{Na}$ reaction”. In: *Phys. Rev. C* 95 (1 Jan. 2017), p. 015806. DOI: [10.1103/PhysRevC.95.015806](https://doi.org/10.1103/PhysRevC.95.015806). URL: <https://link.aps.org/doi/10.1103/PhysRevC.95.015806>.

- [17] Carretta, E. et al. “Properties of stellar generations in globular clusters and relations with global parameters”. In: *A&A* 516 (2010), A55. DOI: [10.1051/0004-6361/200913451](https://doi.org/10.1051/0004-6361/200913451). URL: <https://doi.org/10.1051/0004-6361/200913451>.
- [18] Carretta, E. et al. “Multiple stellar populations in the globular cluster NGC1851”. In: *A&A* 533 (2011), A69. DOI: [10.1051/0004-6361/201117269](https://doi.org/10.1051/0004-6361/201117269). URL: <https://doi.org/10.1051/0004-6361/201117269>.
- [19] Alessandra Slemer et al. “ ^{22}Ne and ^{23}Na ejecta from intermediate-mass stars: The impact of the new LUNA rate for $^{22}\text{Ne}(p,\gamma)^{23}\text{Na}$ ”. In: (Nov. 2016).
- [20] Inese I. Ivans et al. “New Analyses of Star-to-Star Abundance Variations among Bright Giants in the Mildly Metal-poor Globular Cluster M5”. In: *The Astronomical Journal* 122.3 (Sept. 2001), pp. 1438–1463. DOI: [10.1086/322108](https://doi.org/10.1086/322108). URL: <https://doi.org/10.1086/322108>.
- [21] Raffaele Gratton, Christopher Sneden, and Eugenio Carretta. “Abundance Variations within Globular Clusters”. In: *Annual Review of Astronomy and Astrophysics* 42.1 (2004), pp. 385–440. DOI: [10.1146/annurev.astro.42.053102.133945](https://doi.org/10.1146/annurev.astro.42.053102.133945). eprint: <https://doi.org/10.1146/annurev.astro.42.053102.133945>. URL: <https://doi.org/10.1146/annurev.astro.42.053102.133945>.
- [22] P. Ventura and F. D’Antona. “Does the oxygen-sodium anticorrelation in globular clusters require a lowering of the $^{23}\text{Na}(p,\alpha)^{20}\text{Ne}$ reaction rate?” In: *Astronomy & Astrophysics* 457.3 (Oct. 2006), pp. 995–1001. DOI: [10.1051/0004-6361:20065481](https://doi.org/10.1051/0004-6361:20065481).
- [23] Thibaut Decressin et al. “Fast rotating massive stars and the origin of the abundance patterns in galactic globular clusters”. In: *Astronomy and Astrophysics* 464 (Nov. 2006). DOI: [10.1051/0004-6361:20066013](https://doi.org/10.1051/0004-6361:20066013).
- [24] Amanda I. Karakas and John C. Lattanzio. “The Dawes Review 2: Nucleosynthesis and Stellar Yields of Low- and Intermediate-Mass Single Stars”. In: *Publications of the Astronomical Society of Australia* 31 (2014), e030. DOI: [10.1017/pasa.2014.21](https://doi.org/10.1017/pasa.2014.21).
- [25] Izzard, R. G. et al. “Reaction rate uncertainties and the operation of the NeNa and MgAl chains during HBB in intermediate-mass AGB stars”. In: *A&A* 466.2 (2007), pp. 641–648. DOI: [10.1051/0004-6361:20066903](https://doi.org/10.1051/0004-6361:20066903). URL: <https://doi.org/10.1051/0004-6361:20066903>.
- [26] John Cesaratto† et al. “Measurement of the $E_{cm} = 138$ keV resonance in the $^{23}\text{Na}(p,\gamma)^{24}\text{Mg}$ reaction and the abundance of sodium in AGB stars”. In: *Physical Review C* 88 (Dec. 2013), p. 065806. DOI: [10.1103/PhysRevC.88.065806](https://doi.org/10.1103/PhysRevC.88.065806).
- [27] Jordi Josè and Margarita Hernanz. “Nucleosynthesis in classical nova explosions”. In: *Journal of Physics G: Nuclear and Particle Physics* 34.12 (Oct. 2007), R431–R458. DOI: [10.1088/0954-3899/34/12/r01](https://doi.org/10.1088/0954-3899/34/12/r01). URL: <https://doi.org/10.1088/0954-3899/34/12/r01>.
- [28] Michael M. Shara et al. “The Masses and Accretion Rates of White Dwarfs in Classical and Recurrent Novae”. In: *The Astrophysical Journal* 860.2 (June 2018), p. 110. DOI: [10.3847/1538-4357/aabfbd](https://doi.org/10.3847/1538-4357/aabfbd). URL: <https://doi.org/10.3847/1538-4357/aabfbd>.
- [29] Pavel Denissenkov and Falk Herwig. “The Abundance Evolution of Oxygen, Sodium and Magnesium in Extremely Metal-Poor Intermediate Mass Stars: Implications for the Self-Pollution Scenario in Globular Clusters”. In: *The Astrophysical Journal* 590 (May 2003). DOI: [10.1086/376748](https://doi.org/10.1086/376748).
- [30] Christian Iliadis et al. “The Effects of Thermonuclear Reaction-Rate Variations on Nova Nucleosynthesis: A Sensitivity Study”. In: *The Astrophysical Journal Supplement Series* 142.1 (Sept. 2002), pp. 105–137. DOI: [10.1086/341400](https://doi.org/10.1086/341400). URL: <https://doi.org/10.1086/341400>.

- [31] David Branch. “Supernovae”. In: *Encyclopedia of Physical Science and Technology (Third Edition)*. Ed. by Robert A. Meyers. Third Edition. New York: Academic Press, 2003, pp. 335–350. ISBN: 978-0-12-227410-7. DOI: <https://doi.org/10.1016/B0-12-227410-5/00754-7>. URL: <https://www.sciencedirect.com/science/article/pii/B0122274105007547>.
- [32] Parikh A., José J., and Seitzzahl I.R. “The effects of variations in nuclear interactions on nucleosynthesis in thermonuclear supernovae”. In: *Astronomy & Astrophysics* 557, A3 (Sept. 2013), A3. DOI: [10.1051/0004-6361/201321518](https://doi.org/10.1051/0004-6361/201321518). arXiv: [1306.6007](https://arxiv.org/abs/1306.6007) [astro-ph.SR].
- [33] Neil Tanner. “Direct Radiative Capture of Protons by O^{16} and Ne^{20} ”. In: *Phys. Rev.* 114 (4 May 1959), pp. 1060–1064. DOI: [10.1103/PhysRev.114.1060](https://doi.org/10.1103/PhysRev.114.1060). URL: <https://link.aps.org/doi/10.1103/PhysRev.114.1060>.
- [34] C. Van der Leun and W.L. Mouton. “The reaction $^{20}Ne(p, \gamma)^{21}Na$ ”. In: *Physica* 30.2 (1964), pp. 333–340. ISSN: 0031-8914. DOI: [https://doi.org/10.1016/0031-8914\(64\)90006-0](https://doi.org/10.1016/0031-8914(64)90006-0). URL: <https://www.sciencedirect.com/science/article/pii/0031891464900060>.
- [35] G C Thomas and N W Tanner. “The Cross Section of $^{20}Ne(p, \gamma)^{21}Na$ ”. In: *Proceedings of the Physical Society* 75.4 (Apr. 1960), pp. 498–501. DOI: [10.1088/0370-1328/75/4/303](https://doi.org/10.1088/0370-1328/75/4/303). URL: <https://doi.org/10.1088/0370-1328/75/4/303>.
- [36] C. Rolfs et al. “Hydrogen burning of ^{20}Ne and ^{22}Ne in stars”. In: *Nucl. Phys. A* 241 (1975), pp. 460–486. DOI: [10.1016/0375-9474\(75\)90398-X](https://doi.org/10.1016/0375-9474(75)90398-X).
- [37] J. Keinonen, M. Riihonen, and A. Anttila. “Absolute resonance strengths in the $^{20,21,22}Ne(p, \gamma)^{21,22,23}Na$ and $^{21}Ne(p, p_1\gamma)^{21}Ne$ reactions”. In: *Phys. Rev. C* 15 (2 Feb. 1977), pp. 579–586. DOI: [10.1103/PhysRevC.15.579](https://doi.org/10.1103/PhysRevC.15.579). URL: <https://link.aps.org/doi/10.1103/PhysRevC.15.579>.
- [38] A. M. Mukhamedzhanov et al. “Asymptotic normalization coefficients from the $^{20}Ne(^3He, d)^{21}Na$ reaction and astrophysical factor for $^{20}Ne(p, \gamma)^{21}Na$ ”. In: *Phys. Rev. C* 73 (3 Mar. 2006), p. 035806. DOI: [10.1103/PhysRevC.73.035806](https://doi.org/10.1103/PhysRevC.73.035806). URL: <https://link.aps.org/doi/10.1103/PhysRevC.73.035806>.
- [39] C.A. Bertulani et al. “Indirect methods in nuclear astrophysics”. In: *Journal of Physics: Conference Series* 703 (Apr. 2016), p. 012007. DOI: [10.1088/1742-6596/703/1/012007](https://doi.org/10.1088/1742-6596/703/1/012007). URL: <https://doi.org/10.1088/1742-6596/703/1/012007>.
- [40] Andrew Leland Cooper. “A Low-Energy Study of the $^{20}Ne(p, \gamma)^{21}Na$ Reaction with High-Current Proton Beams at LENA”. PhD thesis. University of North Carolina, Chapel Hill, Jan. 2019.
- [41] Ulrike Hager. “Measuring radiative capture rates at DRAGON”. In: Apr. 2013, p. 015. DOI: [10.22323/1.146.0015](https://doi.org/10.22323/1.146.0015).
- [42] E. Masha. “Astrophysical nuclear reactions on Neon isotopes at LUNA”. PhD thesis. Università degli Studi di Milano, 2022.
- [43] C. Iliadis et al. “Charged-particle thermonuclear reaction rates: III. Nuclear physics input”. In: *Nuclear Physics A* 841.1 (2010). The 2010 Evaluation of Monte Carlo based Thermonuclear Reaction Rates, pp. 251–322. ISSN: 0375-9474. DOI: <https://doi.org/10.1016/j.nuclphysa.2010.04.010>. URL: <https://www.sciencedirect.com/science/article/pii/S0375947410004203>.
- [44] C. Angulo et al. “A compilation of charged-particle induced thermonuclear reaction rates”. In: *Nuclear Physics A* 656.1 (Aug. 1999), pp. 3–183. DOI: [10.1016/S0375-9474\(99\)00030-5](https://doi.org/10.1016/S0375-9474(99)00030-5).
- [45] C. Broggini et al. “LUNA: Status and Prospects”. In: (July 2017). DOI: [10.1016/j.ppnp.2017.09.002](https://doi.org/10.1016/j.ppnp.2017.09.002). eprint: [1707.07952](https://arxiv.org/abs/1707.07952). URL: <https://arxiv.org/pdf/1707.07952.pdf>.

- [46] Carlo Brogini et al. “LUNA: Nuclear Astrophysics Deep Underground”. In: *Annual Review of Nuclear and Particle Science - ANNU REV NUCL PAR SCI* 60 (Oct. 2010). DOI: [10.1146/annurev.nucl.012809.104526](https://doi.org/10.1146/annurev.nucl.012809.104526).
- [47] A. Formicola et al. “The LUNA II 400kV accelerator”. In: *Nuclear Instruments and Methods in Physics Research Section A: Accelerators, Spectrometers, Detectors and Associated Equipment* 507.3 (2003), pp. 609–616. ISSN: 0168-9002. DOI: [https://doi.org/10.1016/S0168-9002\(03\)01435-9](https://doi.org/10.1016/S0168-9002(03)01435-9). URL: <https://www.sciencedirect.com/science/article/pii/S0168900203014359>.
- [48] Chiara Casella et al. “A new setup for the underground study of capture reactions”. In: *Nuclear Instruments and Methods in Physics Research Section A: Accelerators, Spectrometers, Detectors and Associated Equipment* 489 (Aug. 2002), pp. 160–169. DOI: [10.1016/S0168-9002\(02\)00577-6](https://doi.org/10.1016/S0168-9002(02)00577-6).
- [49] F. Ferraro et al. “A high-efficiency gas target setup for underground experiments, and re-determination of the branching ratio of the 189.5 keV $^{22}\text{Ne}(p,\gamma)^{23}\text{Na}$ resonance”. In: *European Physical Journal A* 54.3, 44 (Mar. 2018), p. 44. DOI: [10.1140/epja/i2018-12476-7](https://doi.org/10.1140/epja/i2018-12476-7). arXiv: [1802.04164](https://arxiv.org/abs/1802.04164) [nucl-ex].
- [50] D. Bemmerer et al. “Feasibility of low-energy radiative-capture experiments at the LUNA underground accelerator facility”. In: *The European Physical Journal A - Hadrons and Nuclei* 24.2 (2005), pp. 313–319. DOI: [10.1140/epja/i2004-10135-4](https://doi.org/10.1140/epja/i2004-10135-4). URL: <https://doi.org/10.1140/epja/i2004-10135-4>.
- [51] A. Cacioli et al. “Ultra-sensitive in-beam γ -ray spectroscopy for nuclear astrophysics at LUNA”. In: *European Physical Journal A* 39.2 (Feb. 2009), pp. 179–186. DOI: [10.1140/epja/i2008-10706-3](https://doi.org/10.1140/epja/i2008-10706-3). arXiv: [0812.3223](https://arxiv.org/abs/0812.3223) [nucl-ex].
- [52] Kai Vetter. “Recent Developments in the Fabrication and Operation of Germanium Detectors”. In: *Annual Review of Nuclear and Particle Science* 57.1 (2007), pp. 363–404. DOI: [10.1146/annurev.nucl.56.080805.140525](https://doi.org/10.1146/annurev.nucl.56.080805.140525). eprint: <https://doi.org/10.1146/annurev.nucl.56.080805.140525>. URL: <https://doi.org/10.1146/annurev.nucl.56.080805.140525>.
- [53] James F. Ziegler, M.D. Ziegler, and J.P. Biersack. “SRIM – The stopping and range of ions in matter (2010)”. In: *Nuclear Instruments and Methods in Physics Research Section B: Beam Interactions with Materials and Atoms* 268.11 (2010). 19th International Conference on Ion Beam Analysis, pp. 1818–1823. ISSN: 0168-583X. DOI: <https://doi.org/10.1016/j.nimb.2010.02.091>. URL: <https://www.sciencedirect.com/science/article/pii/S0168583X10001862>.
- [54] *SRIM- The Stopping and Range of Ions in Matter*. URL: <http://www.srim.org/PlotCit.htm>.
- [55] F. Ferraro. “Direct measurement of the $^{22}\text{Ne}(p,\gamma)^{23}\text{Na}$ reaction cross section at astrophysical energies”. PhD thesis. Università degli Studi di Genova, 2017.
- [56] J. Görres et al. “The influence of intense ion beams on gas target densities”. In: *Nuclear Instruments and Methods* 177.2 (1980), pp. 295–303. ISSN: 0029-554X. DOI: [https://doi.org/10.1016/0029-554X\(80\)90036-1](https://doi.org/10.1016/0029-554X(80)90036-1). URL: <https://www.sciencedirect.com/science/article/pii/0029554X80900361>.
- [57] D. Bemmerer et al. “Low energy measurement of the $^{14}\text{N}(p,\gamma)^{15}\text{O}$ total cross section at the LUNA underground facility”. In: *Nuclear Physics A* 779 (2006), pp. 297–317. ISSN: 0375-9474. DOI: <https://doi.org/10.1016/j.nuclphysa.2006.09.001>. URL: <https://www.sciencedirect.com/science/article/pii/S0375947406005902>.

-
- [58] H. W. Becker et al. “Low energy resonances in $^{21}\text{Ne}(p,\gamma)^{22}\text{Na}$ examined with a high energy resolution ion beam”. In: *Zeitschrift für Physik A Hadrons and Nuclei* 343.3 (1992), pp. 361–366. DOI: [10.1007/BF01291537](https://doi.org/10.1007/BF01291537). URL: <https://doi.org/10.1007/BF01291537>.
- [59] M. Marta et al. “Study of beam heating effect in a gas target through Rutherford scattering”. In: *Nuclear Instruments and Methods in Physics Research Section A: Accelerators, Spectrometers, Detectors and Associated Equipment* 569.3 (2006), pp. 727–731. ISSN: 0168-9002. DOI: <https://doi.org/10.1016/j.nima.2006.09.093>. URL: <https://www.sciencedirect.com/science/article/pii/S0168900206017505>.
- [60] F. Cavanna et al. “A new study of the $^{22}\text{Ne}(p,\gamma)^{23}\text{Na}$ reaction deep underground: Feasibility, setup and first observation of the 186 keV resonance”. In: *The European Physical Journal A* 50.11 (2014), p. 179. DOI: [10.1140/epja/i2014-14179-5](https://doi.org/10.1140/epja/i2014-14179-5). URL: <https://doi.org/10.1140/epja/i2014-14179-5>.
- [61] V. Mossa et al. “The baryon density of the Universe from an improved rate of deuterium burning”. In: *Nature* 587.7833 (2020), pp. 210–213. DOI: [10.1038/s41586-020-2878-4](https://doi.org/10.1038/s41586-020-2878-4).
- [62] C. Casella et al. “First measurement of the $d(p,\gamma)^3\text{He}$ cross section down to the solar Gamow peak”. In: *Nuclear Physics A* 706.1 (2002), pp. 203–216. ISSN: 0375-9474. DOI: [https://doi.org/10.1016/S0375-9474\(02\)00749-2](https://doi.org/10.1016/S0375-9474(02)00749-2). URL: <https://www.sciencedirect.com/science/article/pii/S0375947402007492>.
- [63] R. Azuma et al. “AZURE: An R-matrix code for nuclear astrophysics”. In: *Physical Review C - PHYS REV C* 81 (Apr. 2010). DOI: [10.1103/PhysRevC.81.045805](https://doi.org/10.1103/PhysRevC.81.045805).
- [64] R. Longland et al. “Charged-particle thermonuclear reaction rates: I. Monte Carlo method and statistical distributions”. In: *Nuclear Physics A* 841.1 (2010). The 2010 Evaluation of Monte Carlo based Thermonuclear Reaction Rates, pp. 1–30. ISSN: 0375-9474. DOI: <https://doi.org/10.1016/j.nuclphysa.2010.04.008>. URL: <https://www.sciencedirect.com/science/article/pii/S0375947410004185>.